TU WIEN

TECHNISCHE
UNIVERSITÄT
WIEN

Diplomarbeit

Studies of Few-Monolayer Zirconia Films and Metal Nucleation on Zirconia Surfaces

Ausgeführt am

Institut für Angewandte Physik

der Technischen Universität Wien

Unter Anleitung von

Ao.Univ.Prof. Dipl.-Ing. Dr.techn. Michael Schmid

Dipl.-Ing. Peter Lackner

Durch

Sabrina Mayr, BSc

Wien, Oktober 2017

Abstract

Due to the importance of zirconia (ZrO_2) for many applications, such as solid oxide fuel cells or oxygen sensors, it is of big interest to study the material and its metal interfaces at atomic scale. This is only possible by preparing thin oxide films on a conductive substrate, since ZrO_2 is an electronic insulator. Therefore, 5–6 ML thick ZrO_2 films were prepared on a Rh(111) single crystal by sputter deposition in ultra-high vacuum (UHV). The growth and phase transformation of the films are studied in the first part of this work. Investigations by scanning tunneling microscopy (STM), low-energy electron diffraction (LEED) and X-ray photoelectron spectroscopy (XPS) reveal the formation of a (2×1) row structure (w.r.t. cubic ZrO_2) and that the Zr $3d_{5/2}$ is located at a binding energy of 183.2 eV (after post-annealing in O_2 atmosphere at 650 °C), which is both confirming ZrO_2 in tetragonal phase. ZrO_2 is stable in the tetragonal phase up to a temperature of 700 °C. Above this temperature it transforms into monoclinic ZrO_2, which can be seen in STM and LEED due to the formation of a (2×2) structure (w.r.t. cubic ZrO_2) whose domains are rotated with respect to each other. Moreover, XPS reveals peak shifts of Zr 3d and O 1s to lower binding energies, with respect to the peaks in tetragonal phase. The Zr $3d_{5/2}$ peak is then positioned at 181.5 eV.

The second part of this work deals with the investigation of metal nucleation on both ZrO_2 phases. Fe, Ag, Au, and Rh were deposited on the 5–6 ML thick ZrO_2 films by evaporation. The growth mode, the cluster density, and the cluster sizes were examined by STM and the following trend could be determined: The metals showed different strengths of metal-oxide bonding: Ag≈Au<Fe≈Rh. Additional XPS measurements revealed surprising results. On monoclinic ZrO_2, the oxide peaks shift to higher binding energies according to the strength of metal-oxide bonding. The results do not match for tetragonal ZrO_2, however. The oxide peaks are either not shifting at all or slightly shifting to lower binding energies. As a general trend, it was found, that the XPS peaks of tetragonal and monoclinic ZrO_2 are closer after depositing metals on the oxid. This is probably induced by band bending of the oxide due to metal clusters.

Zusammenfassung

Zirkoniumdioxid (ZrO_2) ist ein wichtiges Material für viele Anwendungen, wie z.B. Festoxidbrennstoffzellen oder Sauerstoffsensoren. Es ist daher von großem Interesse, die atomare Struktur der Oxidoberfläche sowie seiner Grenzfläche zu Metallen zu untersuchen. Da ZrO_2 ein isolierendes Material ist, kann das Oxid nur als dünner Film auf einem leitenden Substrat untersucht werden. Deshalb wurden 5–6 ML dicke ZrO_2 Filme auf einem Rh(111)-Einkristall präpariert und durch Rastertunnelmikroskopie (STM), Röntgenphotoelektronenspektroskopie (XPS) und Beugung niederenergetischer Elektronen (LEED) untersucht. Zr $3d_{5/2}$ wurde bei einer Bindungsenergie von 183.2 eV gemessen, nachdem die Probe in Sauerstoff auf 650 °C geheizt wurde. Somit konnte die Bildung von ZrO_2 in tetragonaler Phase festgestellt werden, welche bis zu einer Temperatur von bis zu 700 °C stabil ist. Für diese Phase wurde eine (2×1) Struktur (bezogen auf kubisches ZrO_2) beobachtet. Bei höherer Temperatur transformiert ZrO_2 zur monoklinen Phase, welche eine (2×2) Struktur im STM und LEED aufweist und dessen Zr 3d Linien bei einer Bindungsenergie von 181.5 eV liegen.

Der zweite Teil der Arbeit beschäftigt sich mit Nukleation von Metallen auf 5–6 ML dicken ZrO_2 Filmen in beiden Phasen. Dabei wurde das Wachstum, die Flächendichte und Größe von Fe, Ag, Au und Rh-Clustern mit STM untersucht, welche folgenden Trend zu höheren Metall-Oxid-Bindungen zeigen: Ag≈Au<Fe≈Rh. Zusätzliche XPS-Messungen ergaben überraschende Ergebnisse: Die Bindungsenergien der Zr 3d Linien von monoklinem ZrO_2 verschieben sich bei stärker gebundenen Metallclustern zu höheren Bindungsenergien. Bei tetragonalem ZrO_2 verschiebt sich Zr 3d entweder leicht zu niedrigeren bzw. höheren Bindungsenergien oder verändert sich überhaupt nicht. Generell konnte beobachtet werden, dass sich die Zr 3d Linien beider Phasen aufeinander zu bewegen, nachdem Metalle auf die Oxidoberfläche gedampft wurden.

Acknowledgment

I would like to express my sincere gratitude to my supervisors Michael Schmid and Peter Lackner for giving me the chance to write this thesis and for the great support and many advices during the process of my diploma thesis. I would like to thank Peter for his endless patience at teaching me how to operate in the lab.

Furthermore, I would like to express my thanks to the whole group for the nice hours in between and the support while measuring. Special thanks to Ulrike Diebold who introduced me to the group.

Many thanks to my parents, who gave me the opportunity to study physics and for their continuous encouragement during all this years.

Finally, I would like to thank Laurin Holzner for keeping me happy and alive, especially during the last few weeks of writing this thesis.

Contents

1 Introduction

Zirconia (ZrO_2) is an important material for many applications, such as a solid electrolyte in solid oxide fuel cells (SOFC) [1] or for oxygen sensors [2]. Typically, it is used in a cubic form stabilized by dopants, for example yttria-stabilized zirconia (YSZ), and offers many favorable properties, such as electronic insulation with a wide band gap ($\geq 5\,\mathrm{eV}$) [3], thermal stability (melting point at $2983\,\mathrm{K}$), mechanical strength and oxygen ion conductivity. In SOFCs, YSZ is sandwiched between two electric conductors which work as anode and cathode materials. It is therefore of big interest to study ZrO_2 surfaces and especially the metal-ZrO_2 interfaces at the atomic scale. Due to its insulating properties, however, surface studies of ZrO_2 or metal-ZrO_2 studies are rare, because most surface-probing techniques require electronic conductivity. This can be circumvented by analyzing thin ZrO_2 films. Ultra-thin ZrO_2 films ($1\,\mathrm{ML}$ thick) were already prepared by oxidizing alloys like Pt_3Zr or Pd_3Zr and studied by scanning tunneling microscopy (STM) and X-ray photoelectron spectroscopy (XPS) [4, 5]. Moreover, the metal nucleation on ultra-thin ZrO_2 films was investigated and the growth mechanism, cluster densities and structures of Ag, Au, Pd, Ni, and Fe were studied by STM [6].

This work deals with the growth of few layer thick ZrO_2 films ($\approx$5–6 ML) on Rh(111), prepared using a home-built Zr sputter source [7]. The ZrO_2 film and its phase transition from tetragonal to monoclinic phase was investigated by STM, XPS, and low-energy electron diffraction (LEED) in the first part of this work. The second part of this work studies the growth of metals on tetragonal and monoclinic ZrO_2. Fe, Ag, Au, and Rh were deposited at room temperature by evaporation. The growth mechanism, the cluster densities, and the structures were investigated by STM. Furthermore, XPS measurements were performed to examine the electronic structure of the zirconia films and their changes after depositing metals on the surface.

2 Experimental Methods and Setup

All measurements of this work were performed in the room temperature STM lab. The following chapter gives a survey of the experimental methods used and the instrumental setup of the vacuum chamber.

2.1 Experimental Methods

2.1.1 Scanning Tunneling Microscopy (STM)

Scanning tunneling microscopy is a method to measure the topography and electronic structure of solid surfaces at atomic scale with the help of the tunneling effect [8, 9, 10]. With the help of piezo elements a sharp tungsten tip is moved close to the sample ($\approx$0.5–1.5 nm), at which a voltage is applied (typically in the range of $\pm$0.002–$\pm$6 V). This enables electrons to tunnel either from tip to sample (=anode) or vice versa (sample = cathode) and a current can be measured. The approach is performed in single movements forward (z-direction), after which the z-piezo is extending until a tunneling current I_{tunnel} is measured. If no current could be measured, the z-piezo gets retracted and the tip moves further towards the sample. This procedure is repeated until a current can be measured. During operation the distance between tip and sample, typically, lies in the range of 0.5–1.5 nm. To image a sample surface, the tip scans over the surface (x-y plane), usually using the constant current mode. A feedback loop controls the current by varying the tip-sample distance depending on the measured current, trying to keep it constant. The combination of sample topography and electronic structure can then be imaged by plotting the measured piezo voltage which controls the tip movement in z-direction (Fig. 2.1). The tunneling current typically lies in the range of 0.05–10 nA and can be derived from the Schrödinger equation 2.1, in which the potential barrier between sample and tip is estimated to have the same height as the work function Φ [10]:

$$(-\frac{h^2}{2m}\Delta^2 + V)\Psi = E\Psi \tag{2.1}$$

$$\Psi(z) \propto e^{-\kappa z} \quad \text{with} \quad \kappa = \sqrt{\frac{2m\Phi}{\hbar^2}}$$

The transmission T of the tunneling junction is proportional to the wave function squared $|\Psi|^2$. The tunneling current I_{tunnel} is proportional to T. If d is the width of Φ, the tunneling current decreases exponentially with d (2.2) [10]:

$$I_{tunnel} \propto T \propto |\Psi(d)|^2 \propto e^{-2\kappa d} \tag{2.2}$$

Thus the tunneling current changes depending on the work functions of tip and sample by a factor of 5 to 10 after a distance change of the tip of $\approx 1\,\text{Å}$. Therefore, a resolution in z-direction of about $1\,\text{pm}$ is possible if the current is held constant within 1–$2\,\%$. However, external interferences such as vibrations or electrical noise have to be avoided.
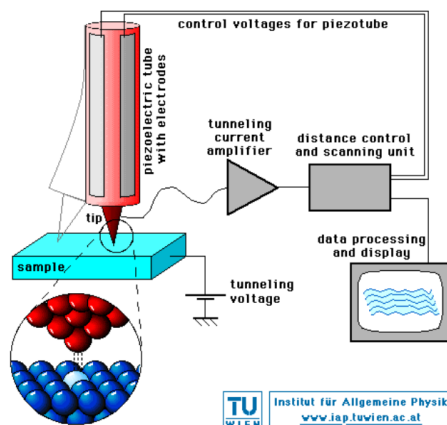
Figure 2.1: Schematical structure of a Scanning Tunneling Microscope (Figure: Michael Schmid, TU Wien)

2.1.2 X-Ray Photoelectron Spectroscopy (XPS)

X-ray photoelectron spectroscopy is a technique to quantitatively determine the elemental composition of a sample and also gives information about the chemical state of the elements [8, 10, 11]. Moreover, compared to STM, it is possible to also investigate samples with low electrical conductivity and survey a larger sample area at the same time.

An X-ray beam is pointed on the sample, which emits photoelectrons. The emitted electrons have a characteristic kinetic energy E_{kin} dependent of the element. E_{kin} of the emitted photoelectrons is measured by an hemispherical energy analyzer and their binding energy E_B can be derived from the work function Φ_{sample} and the energy of the photons $h\nu$ (2.3 and Fig. 2.2) [10]:

$$h\nu = E_B + \Phi_{sample} + E_{kin} \tag{2.3}$$

For the determination of E_B it is not necessary to know Φ_{sample}, since the work function $\Phi_{analyzer}$ of the analyzer is known which is linear dependent to Φ_{sample} and E_{kin}.

XPS is a surface-sensitive method, since only the electrons emitted from the very top atomic layers contribute to the sharp signals of the characteristic spectral lines. The electrons emitted from atoms deeper in the bulk get inelastically scattered by the other atoms on their way out of the sample and do not reach the surface or loose energy. This electrons are responsible for the background signal. The intensity I of the spectral lines therefore depends on the depth z where the photoelectrons are emitted in the solid, the mean free path length λ and the exit angle θ [10].

$$I \propto e^{-z/\lambda \cos\theta} \tag{2.4}$$

It is even possible to differ between the signal of the surface layer and the bulk, which form two separate spectral lines and which can be distinguished, if the energy resolution is high enough (surface core level shift). Moreover, different chemical states of an element can be distinguished by XPS, since the binding energy is dependent on its bonding properties. If the element is bound, its electron density is changing. For Zr in ZrO_2 for example the electron density decreases, which causes a increasing binding energy for the remaining electrons. Thus the Zr peaks shift to higher binding energies with respect to the signal of the pure element (chemical shift).
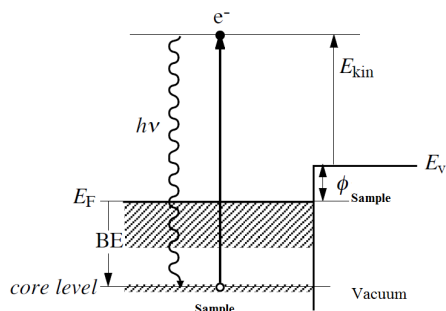
Figure 2.2: Scheme for the determination of the binding energy of a sample (taken from: [10])

2.1.3 Low Energy Electron Diffraction (LEED)

LEED is a method to investigate the symmetry of a sample surface by imaging the diffraction of an electron beam caused by the periodic arrangement of a lattice [8, 10]. The electron beam with energies between 20–500 eV is directed perpendicular to the sample and the electron wavelength (1.7–0.5 Å) is shorter than the lattice constants of a solid. The diffracted electrons are then detected at a spherical screen and the reciprocal space of the sample surface can be imaged as a diffraction pattern. Due to the short mean free path for low energy electrons in a solid, only the topmost atomic layers contribute to the diffraction signal, which makes this technique surface sensitive.

2.2 Chamber and Instrumentation

2.2.1 UHV Chamber in the Room Temperature STM Lab

The ultra-high vacuum chamber features two stainless steel vessels and is divided into two systems: a preparation chamber and a measurement chamber, called main chamber.

The preparation chamber is mainly used to clean samples by sputtering and annealing with an Ar^+ sputter source and an electron-beam heater. Moreover, it features evaporators for vapor deposition of metals and leak valves to dose gases, e.g. oxygen. Note that the indicated annealing temperatures in this work are not precise, since the thermocouple is mounted on the sample holder on the manipulator and not directly on the sample, a deviation of plus 50–100 °C is estimated. The preparation chamber is equipped with following instruments, which were used to clean the sample and prepare the oxide films:

- home-build Zr sputter source [7]

- Triple evaporator Focus EFM 3T [1]

- water cooled quartz crystal micro balance, XTC/2[2]

- HAL Quadrupole mass spectrometer[3]

- sputter gun VG EX05

The main chamber is used as an analysis chamber in which it is possible to perform STM, XPS, LEED, AES (Auger Electron Spectroscopy) and ISS (Ion Scattering Spectroscopy) measurements and it features the following instruments which were used in this work:

- STM: Omicron μSTM

- Non-monochromatized X-ray gun: "XR3E2"[4], features both a MgK_α and AlK_α anode

- PHOIBOS 100 hemispherical energy analyzer with a HSA 3500plus power supply and a MCD-5 detector[5]

- Er-LEED optics[6]

2.2.2 Ultra High Vacuum (UHV)

The experiments were performed in ultra-high vacuum (UHV) to ensure as little contamination of the sample surface as possible. At pressures between 10^{-10}–10^{-11} mbar the sample surface can be held clean for up to 10^4 s in UHV, whereas the sample would be contaminated immediately in air [8].

A rotary vane pump of the type "Duo 10 M"[7] is used as a forepump and a turbo-molecular pump of the type "HiPace 700"[7] to reach pressures in the UHV regime in the UHV chamber in the room temperature STM lab. Ion getter pumps (the main chamber features a "Varian Picotorr 350"[8]) are mounted additionally to support the other pumps and to maintain the UHV.

The pressure in the preparation chamber is measured by a Penning gauge of the type Balzers IKR020 with TPG300 controller, whereas the main chamber features a Bayard-Alpert gauge of the type Varian UHV-24 with Balzers IMG070 controller.

The base pressures during the experiments where in the range of $0.6 \cdot 10^{-10}$ mbar in the main chamber and below $1 \cdot 10^{-10}$ mbar in the preparation chamber.

---

[1]Focus, Hünstetten, Germany
[2]INFINICON Inc., NY, USA
[3]HIDEN ANALYTICAL, Warrington, United Kingdom
[4]VG Microtech, Sussex, United Kingdom
[5]SPECS GmbH, Berlin, Germany, http://www.specs.de
[6]Vacuum Science Instruments GmbH, Bad Schwalbach, Germany
[7]Pfeiffer Vacuum GmbH, Asslar, Germany, https://group.pfeiffer-vacuum.com
[8]Agilent Technologies, Santa Clara, CA, United States, http://www.agilent.com

2.2.3 Zr Sputter-Source

For the preparation of the ZrO_2 films, a home-built Zr sputter-source is used (Fig. 2.3) [7], since evaporation of Zr is difficult due to its high melting temperature and low vapor pressure. In principle, a resistively heated W filament emits electrons which are accelerated towards two positively biased grids (U_{front} and U_{rear} for front grid and rear grid, respectively). The electron cloud, which is trapped between the two grids, ionizes Ar which is leaked directly into the sputter source (p_{Ar} is measured with the quadrupole mass spectrometer (QMS) and penning gauge in the preparation chamber and it is estimated that the pressure inside the source is higher by a factor of 27 [7]). The Ar^+ ions are accelerated toward a negatively biased Zr plate ($U_{\text{Zr}-\text{plate}}$), which gets sputtered and emits Zr atoms. Due to the potentials of Zr plate and grids, only neutral Zr atoms can pass and reach the sample. The amount of sputtered Zr is proportional to the current of the Ar^+ ions hitting the Zr plate. Therefore, the measured current $I_{\text{Zr}-\text{plate}}$ at the Zr plate can be used as a measure for the Ar^+ flux. To get a constant Zr flux it is necessary to keep a constant $I_{\text{Zr}-\text{plate}}$ by varying p_{Ar}. The electron emission is controlled by measuring the current $I_{\text{em,front}}$ at the front grid. The whole sputter source is covered by a copper cylinder which is LN_2 cooled.

The preparation of ZrO_2 films is performed by sputtering Zr in oxygen atmosphere (p_{O_2}), which is leaked directly into the vacuum chamber. The settings used for preparing the ZrO_2 films in this work are listed in table 2.1. Note that all oxygen pressures mentioned in this work are measured with the QMS.
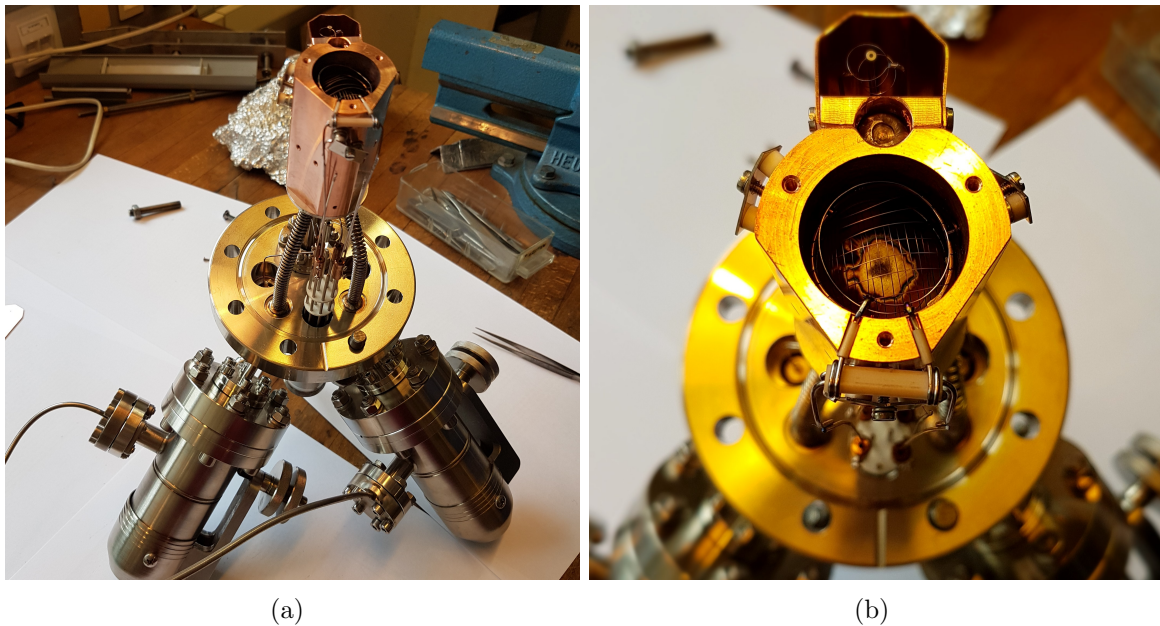

(a)   (b)

Figure 2.3: Zr sputter source without front plate

Table 2.1: Settings for the Zr-sputter source a) before and b) after exchanging the Zr-sputter source electronics and calibrating the QMS

	a)	b)
I_{fil}:	2.43 A	≈ 2.51 A
$I_{\text{em,front}}$:	10–17 mA	17.7 mA
$I_{\text{Zr−plate}}$:	66 μA	71.7 μA (incl. 5.7 μA leaking current)
U_{front}:	150 V	150 V
U_{rear}:	100 V	100 V
$U_{\text{Zr−plate}}$:	−2 kV	−2 kV
p_{O_2}:	$5 \cdot 10^{-8}$ torr	$4.7 \cdot 10^{-8}$ torr (QMS) $\hat{=} 1.2 \cdot 10^{-6}$ mbar
p_{Ar}:	$8 \cdot 10^{-6}$–$2 \cdot 10^{-5}$ mbar	$8 \cdot 10^{-6}$–$9 \cdot 10^{-6}$ mbar

2.2.4 Triple Evaporator

The deposition of metals on the sample surface was performed by a triple evaporator of the type Focus EFM 3T. The evaporator consists of three cells in which Fe and Rh were mounted as rods, whereas Ag and Au were held in crucibles. To evaporate a metal, specific filament currents I_{fil} and voltages U have to be applied on the W filament and the crucible/rod, respectively. The filament is thereby positioned in front of the metals. It emits electrons, which are accelerated towards the crucible/rod. Moreover, a repelling voltage of $+1.2$ kV could be applied at a tube electrode, which is mounted between filament and cell exit, to prevent fast ions from hitting the sample and sputtering the surface or causing defects. For the evaporation of Fe and Ag no repelling voltage was turned on, whereas for Au and Rh (except one preparation) the repelling voltage was applied. The amount of evaporated metal is controlled by measuring the current on the tube electrode I_{flux} and emission current on the crucible/rod I_{em}. The settings for each metal can be found in table 2.2.

Table 2.2: Parameters for the triple evaporator for each metal

Metal	I_{fil}	I_{em}	I_{flux}	U
Fe	2.12 A	7.1 mA	6.5 nA	1000 V
Ag	2.05 A	7.4 mA	≈ 160 nA	901 V
Au	2.05 A	≈ 16.4 mA	≈ 3.5 μA	1000 V
Rh	2.05 A	8–8.3 mA	≈ 5 nA	1000 V

2.2.5 X-Ray Source and Hemispherical Energy Analyzer

The settings for the X-ray source and the hemispherical energy analyzer used for the XPS measurements are listed in the following table:

Table 2.3: Parameters for the XPS measurements

Scan mode:	Fixed analyzer transmission
Scan range:	1.5 kV
Entrance slit:	4: 7×20 mm
Exit slit:	B: open
Iris diameter:	15 mm
Lens mode:	Medium Magnification
E_{pass}:	Overview: 30 eV
	detail spectra: 16 eV
	metal clusters: 50 eV
Excitation source:	XPS: Mg K_{α}, 222 W
Energy range (B.E.):	1000...-5 eV (overview spectra)
Dwell time:	0.1 s
Step:	Overview: 0.5 eV
	all detail spectra: 0.1 eV
	except Au 4f: 1 eV

3 Few-layer ZrO₂ Films on Rh(111)

3.1 ZrO₂ bulk phases

Pure ZrO_2 undergoes two phase transformations before melting [12]:

Liquid (2710 °C) $\leftrightarrow$ Cubic (2377 °C) $\leftrightarrow$ Tetragonal (1205 °C) $\leftrightarrow$ Monoclinic (stable at RT)
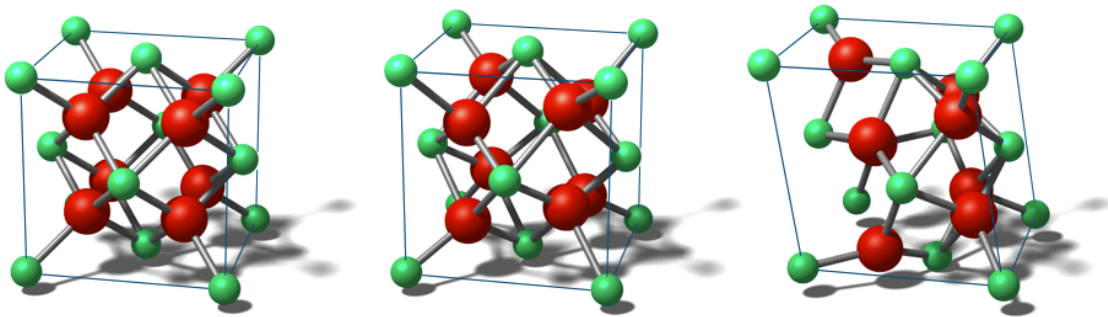

Figure 3.1: 3D Models of the three different solid phases: Cubic - tetragonal - monoclinic ZrO₂. Oxygen in red, Zirconium in green (Figure: Michael Schmid, TU Wien)

The different ZrO_2 phases differ in volume and crystal structure. Monoclinic zirconia has a $\approx 3\%$ larger molar volume than tetragonal zirconia, whereas the molar volumes of tetragonal and cubic zirconia are equal [12]. Moreover, in the monoclinic form, the Zr ions have a seven-fold coordination with oxygen ions and an eight-fold coordination in the tetragonal and cubic phase. Oxygen is coordinated tetrahedral by Zr in the cubic and tetragonal phase, whereas it has a three- or four-fold coordination in monoclinic phase. Also the average Zr-O bond length differs depending to the phases.

Although non-stoichiometry (ZrO_{2-x}) can stabilize the cubic phase at lower temperatures (≈ 1525 °C) it is still very difficult to prepare and study [12]. Therefore, only monoclinic and tetragonal ZrO_2 will be investigated in this work.

Considering the zirconia structures of the two investigated phases it can be determined that the oxygen columns in the tetragonal structure are shifted up and down in z direction compared to the cubic structure (Fig. 3.1) [12]. This leads to a smaller Zr-O distance

of four oxygen atoms and a larger distance of the other four oxygen atoms, which leads to a formation of two interpenetrating tetrahedra and an increasing O-O distance [12]. It is believed that the tetragonal phase is only stable in a non-stochiometric form [12]. However, it was claimed that the tetragonal form is favored also for stoichiometric ZrO_2 at RT if the particle size is small enough (below $300\,\text{Å}$) [13]. On the other hand, it was suggested that this is only possible if the oxide is reduced, which leads to a stabilization caused by oxygen vacancies or trapped OH ions [14]. Nevertheless, it was shown that this size-stabilized tetragonal ZrO_2 is similar to the structure of pure tetragonal ZrO_2 [15]. Moreover, tetragonal ZrO_2 can be stabilized below $1205\,^\circ\text{C}$ by alloying with other oxides (e.g. MgO, Y_2O_3, CaO and Sc_2O_3) [16].

For pure ZrO_2, below $1200\,^\circ\text{C}$ the tetragonal phase becomes unstable and transforms to the monoclinic phase, which causes shear and dilation (Fig. 3.1) [12]. The so increased volume causes micro-cracks in the structure [17, 18].

3.2 Previous Studies

Due to the insulating properties of ZrO_2, to study the oxide with STM it is necessary to prepare thin films on a conducting substrate, which is an established method to study insulators with STM. Meinel *et al.* prepared thin ZrO_2 films on Pt(111) to examine the grown structure by STM, LEED and DFT calculations [19, 20, 21]. The films were prepared by Zr vapor deposition in O_2 atmosphere at $470\,\text{K}$. Although it was not possible to get atomically resolved STM images on most surfaces, it was possible to observe various structures using LEED. Post-annealing at 500–$950\,\text{K}$ led to a p(1×1) ZrO_2(111) LEED pattern, which was ±6° rotated with respect to Pt(111). At an annealing temperature around $950\,\text{K}$ in addition to the (1×1) structure a (2×2) structure (w.r.t. ZrO_2) was found, which fits to a $(\sqrt{7} \times \sqrt{7})$-Pt(111) interface structure. Further annealing up to $1300\,^\circ\text{C}$ led to the rotation of the (1×1) structure rotated by ±6.6° with respect to the substrate, which caused the formation of a $(2\sqrt{3} \times 2\sqrt{3})$ structure, corresponding to a $(\sqrt{19} \times \sqrt{19})$R± 36.6° superstructure with respect to Pt(111) lattice). However, because of the high melting temperature of Zr and the low vapor pressure at the melting point, the preparation of ZrO_2 films was difficult and the long duration of evaporation possibly exposed the sample to contaminations.

A preparation of ultra-thin ZrO_2 films by oxidation of Zr-based alloys made a faster growth of the films possible. Antlanger *et al.* grew ultra-thin ZrO_2 films by oxidation and post-annealing of Pt_3Zr(0001) at $400\,^\circ\text{C}$ and $\approx\!800\,^\circ\text{C}$, respectively [4]. The oxide film, whose oxidation is self-limited, forms a O-Zr-O trilayer, which is laterally contracted compared to a (111) trilayer of the fluorite structure of cubic ZrO_2. The authors of

[4] were successful in atomically resolving the oxide film by STM and determined a $(\sqrt{19} \times \sqrt{19})$R23.4° superstructure (w.r.t. the substrate) and a lattice constant of the oxide film of 0.35 nm. DFT calculations revealed that the oxide trilayer binds weakly to the substrate.

Li *et al.* examined an ultra-thin ZrO_2 film grown under the same preparation conditions on a $Pt_3Zr(0001)$ substrate by oxidation and post-annealing with high-resolution XPS, LEED, DFT and STM [22]. They revealed that the oxidation leads not only to the growth of an ultra-thin trilayer film but also to the formation of three dimensional (3D) ZrO_2 clusters. Moreover, they were successful in determining the correspondence of the Zr 3d XPS peaks to the different Zr species by combining STM, DFT and XPS measurements: the ultrathin oxide film and the 3D clusters have the Zr $3d_{5/2}$ peak at binding energies of 180.7 eV and 182.8 eV, respectively.

Since ultra-thin ZrO_2 films are not necessarily representing the properties of bulk ZrO_2, Choi examined thicker ZrO_2 films on Pt(111) and Rh(111) by STM, LEED and XPS measurements in his PhD thesis [23]. He found a (2×1) superstructure (w.r.t. ZrO_2) after growing several layers of ZrO_2 on Pt(111) and post-annealing of the sample. Atomically resolved STM images show a (2×1) row structure with a 2×0.35 nm periodicity. XPS studies revealed that the Zr $3d_{5/2}$ peak of the oxide is positioned at a binding energy of 182.8 eV, which was determined in [22] as multilayer ZrO_2 peak. While this was the same for ZrO_2 on Pt and Rh, the oxide growth on Pt(111) and Rh(111) reveals also differences. Whereas the (2×1) superstructure is rotated with respect to Pt(111), no rotation could be observed with respect to Rh(111). Moreover, the oxide starts to dewet the Pt(111) substrate at lower annealing temperatures (below 600 °C than Rh(111) (above 700 °C).

The investigations in the following sections build on the results of [23] of growing thicker ZrO_2 films on Rh(111), since the growing properties seem to be best on this substrate. The properties of 5–6 monolayer (ML) thick ZrO_2 films are examined using STM, XPS and LEED.

3.3 Sample Preparation

A Rh(111) single crystal (from MaTecK[1], purity: 99.99 %) is used as a substrate, which is 2 mm thick and has a diameter of 9 mm. The crystal is mounted with Ta clips on a Mo sample plate. To ensure a good heat radiation a hole was drilled into the sample plate.

---

[1]MaTeck GmbH, Juelich, Germany

The sample was cleaned by several sputter-and-annealing cycles in an Ar atmosphere of $p_{Ar} = 8 \cdot 10^{-6}$ mbar. Sputtering was performed at room temperature (RT) and annealing at a temperature of 800 °C for 10 min, respectively. In the end the sample was usually annealed in UHV. The cleanliness of the sample was checked by XPS and STM measurements. XPS surveys confirmed the absence of oxygen and other contaminations from the residual gas on the surface. However, sometimes small Zr 3d signals were measured, which arises from previous Zr depositions. The Zr 3d$_{5/2}$ peak is located at 178.9 eV and fits metallic Zr [24]. Since the goal was to prepare ZrO$_2$ films of 5–6 ML, the remaining small amount of Zr on the surface was not disruptive and the XPS signal of metallic Zr vanished after preparing ordered ZrO$_2$ films. STM measurements on the cleaned surface, which revealed Zr signals in XPS measurements, show the formation of a (2×2) superstructure of metallic Zr on Rh(111) (see section 3.4).

The thick ZrO$_2$ films were prepared using a home-built UHV-compatible Zr-sputter source [7]. The settings of the source during deposition are listed in table 2.1. Note that the settings changed after exchanging the electronics of the Zr-sputter source and a recalibration of the quadrupole mass spectrometer (QMS), which leads to higher signal of mass 32 at lower pressures. Therefore the Zr-sputter source was operated at an actually lower oxygen pressure. Zr was deposited and post-annealed in O$_2$ atmosphere (p_{O_2} see Table 2.1). The preparation of a tetragonal ZrO$_2$ surface requires an annealing temperature of 650 °C for 10 min. To prepare a homogeneous and smooth monoclinic ZrO$_2$ film with few holes, it is necessary to first anneal the sample at lower temperatures (e.g 500 °C for 10 min) to get a surface in tetragonal phase. After the sample cooled down to less than 300 °C it was annealed to 750 °C to transform the oxide into monoclinic phase. Annealing the oxide directly at 750 °C leads to many holes and an inhomogeneous surface. The sample cooled down in O$_2$ atmosphere until a temperature of approximately 300 °C for both phases after annealing.

The XPS measurements were performed with settings listed in Table 2.3. To determine the lattice parameters of the oxides, the STM images had to be undistorted. A detailed description about the distortion method used in this work can be found elsewhere [5].

3.4 (2×2) Zr superstructure on Rh(111)

The Rh(111) single crystal sample was frequently cleaned by sputter-and-annealing cycles and the cleanliness was checked by XPS and STM (see section 3.3). During these measurements, the formation of a (2×2) superstructure caused by Zr could be observed. Fig. 3.2 shows the Rh(111) surface after three sputter ($p_{Ar} = 8 \cdot 10^{-6}$ mbar, $T = $ RT, $t = 10$ min) and annealing ($T_{TC} = 800$ °C, $t = 10$ min) cycles. Two different species can

be determined. The bright species in Fig. 3.2(a), which appear dark in Fig. 3.2(c), have a triangular shape (blue circle and insets). The dark features in Fig. 3.2 (a), appear bright in Fig. 3.2(c) (red circles and insets). Considering the fast Fourier transform (FFT) of Fig. 3.2(c) (Fig. 3.2(b)), the bright species order in a (2×2) superstructure (blurred spots marked with red circles), whereas the sharp spots stem from Rh(111) (yellow circles).
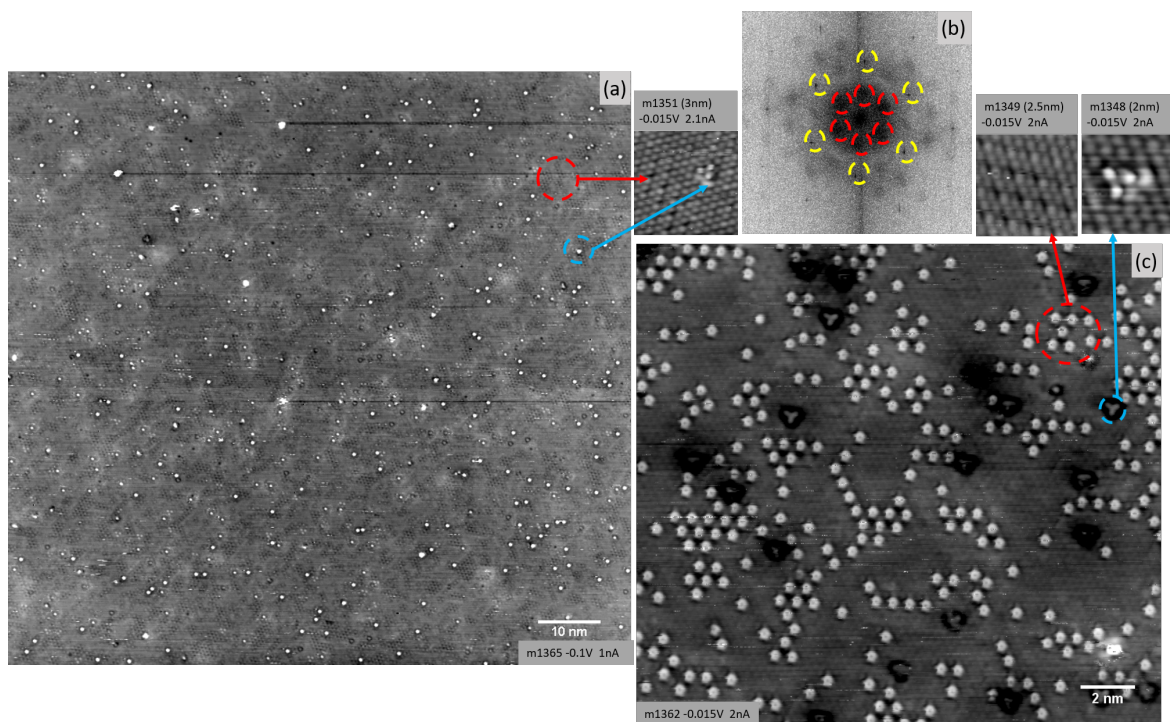

Figure 3.2: STM images of Rh(111) with remaining Zr after several sputter-and-annealing cycles: (a) bright features (blue circles), which appear dark in (c) form triangular shaped features (insets of blue circles). The dark features in (a), bright in (c), arise from a (2×2) superstructure, which can be determined in (b): blurred spots (red circles). The sharp spots (yellow circles) stem from Rh(111)

XPS measurements of the Rh(111) surface, performed with the same preparation as for the STM measurements presented in Fig. 3.2, confirm the presence of Zr (Fig. 3.3(c)). The Zr $3d_{5/2}$ peak is located at $178.9\,\mathrm{eV}$, which confirms metallic Zr [24]. The Zr 3d peak of the cleaned Rh(111) is compared to $2\,\mathrm{ML}$ Zr on Rh(111) and to a $5\,\mathrm{ML}$ thick tetragonal ZrO_2 film. It can be observed that the Zr 3d peak of $2\,\mathrm{ML}$ Zr is slightly shifted to higher binding energies and Zr $3d_{5/2}$ is then located at $179.4\,\mathrm{eV}$. The tetragonal ZrO_2, however, is shifted to a binding energy of $183.2\,\mathrm{eV}$ (see section 3.8). The XPS and STM measurements, which were performed after every cleaning procedure of Rh(111), reveal that the triangular species are always present on the Rh(111) surface (Fig. 3.2

insets of red circles). However, their coverage is too low to be detected by XPS. An XPS signal of metallic Zr is only detected if the (2×2) superstructure forms on the surface. By assuming that each bright dot in the (2×2) superstructure in Fig. 3.2 (c) is caused by one Zr atom, an analysis of Fig. 3.2 (c) reveals a 5 % Zr coverage. Moreover, the XPS measurements show a 0.5 % ratio between the areas of Rh $3d_{5/2}$ and Zr $3d_{5/2}$. According to a SESSA simulation [25], the peak ratio should be 0.3 % for a 5 % Zr coverage, which confirms the assumed result whithin the accuracy of the simulation.
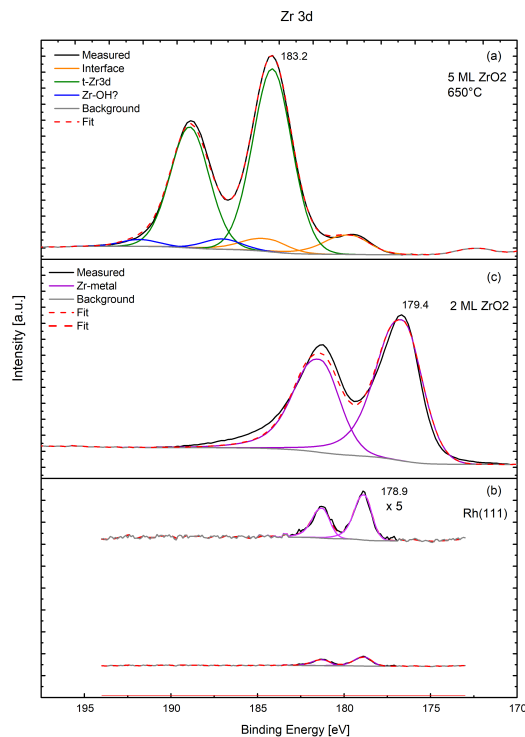

Figure 3.3: XPS comparison of the Zr 3d peak area on cleaned Rh(111) with remaining Zr (c), 2 ML Zr on Rh(111) (b) and 5 ML tetragonal ZrO₂ (a)

3.5 STM of the Tetragonal ZrO₂ Phase

As mentioned above, to create an ordered tetragonal ZrO₂ film with large domains, the 5 ML thick ZrO₂ film was post-annealed in O₂ atmosphere ($p_{O_2} = 5 \cdot 10^{-8}$ torr (QMS)) at 650 °C for 10 min by slowly increasing temperatures. The STM measurements were performed at positive sample bias voltages of 2.5–5 V and currents of 0.1–0.2 nA.

Fig. 3.4 shows a flat smooth area with few islands, which appear 280 nm high and indicate the growth of the next ZrO₂ layer. Measurements at different sample positions confirm a fully covered substrate surface without holes. A row structure can be distinguished, which propagates in three directions (red lines) and is indicative of a

tetragonal surface. Investigations reveal that the domain sizes strongly depend on the annealing temperature and become larger with increasing temperature. Moreover, a moirè structure can be observed, with at least minimum six different orientations (blue lines) and an estimated periodicity of ≈1.7 nm. The moirè structure most probably arises from the interaction of the Rh substrate with the oxide.

Fig. 3.5 shows two different domains of the row structure, which can be determined as a (2×1) structure. Analyzing the FFT of the domains separately reveals that the domains are not exactly rotated by 120° with respect to each other, but slightly differently (Fig. 3.5 (b) and (c)). The green circles represent the domain which runs horizontally and the pink dots mark the second domain (top left in Fig. 3.5 (a)). Moreover, a lattice constant of 0.36 nm is determined, which matches to the lattice constant of bulk ZrO$_2$ [3].

Additionally to the row structure dark features (red circles) can be identified, which could be defects or unknown adsorbates (Fig. 3.6). A comparison between the two images measured immediately after each other reveals that the features are moving or vanish. Moreover, the features are only located at the bright rows, which is also seen in Fig. 3.5 (a) (red circle).
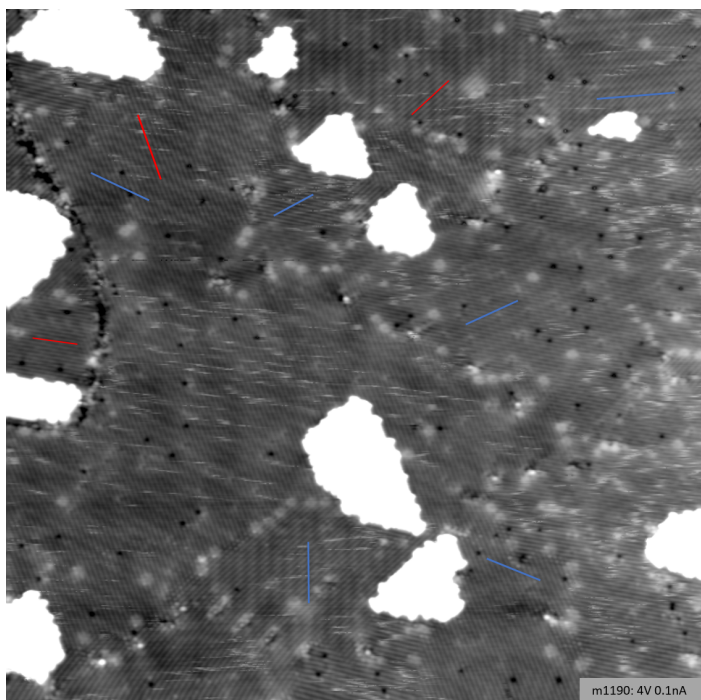
Figure 3.4: STM image of a 5 ML ZrO$_2$/Rh(111) film post-annealed in O$_2$ at 650 °C: a row structure propagating in three directions can be determined (red lines) and a Moirè structure is visible (blue lines)
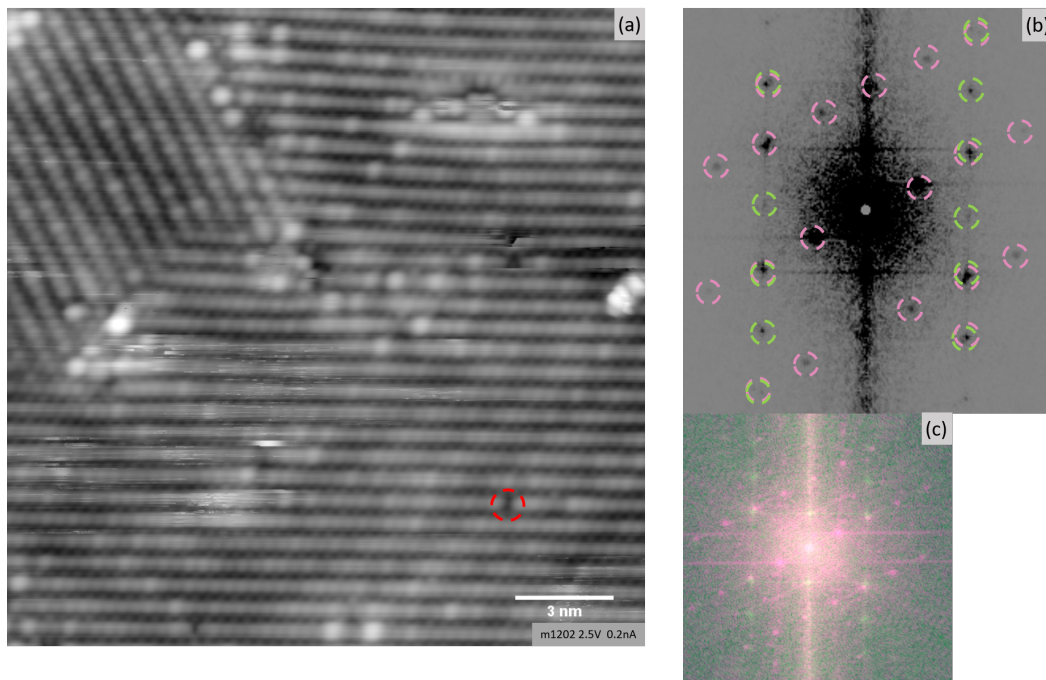
Figure 3.5: STM image of a 5 ML ZrO₂/Rh(111) film post-annealed in O₂ at 650 °C: (a) two different domains are visible, which reveal a (2×1) row structure; the red circle shows a defect in the row structure. (b) FFT of (a): green circles mark the the horizontal row structure of (a), whereas the purple circles show the domain on the top left side of (a). (c) merged FFT of the domains visible in (a): green: horizontal domain, purple: domain top left in (a)
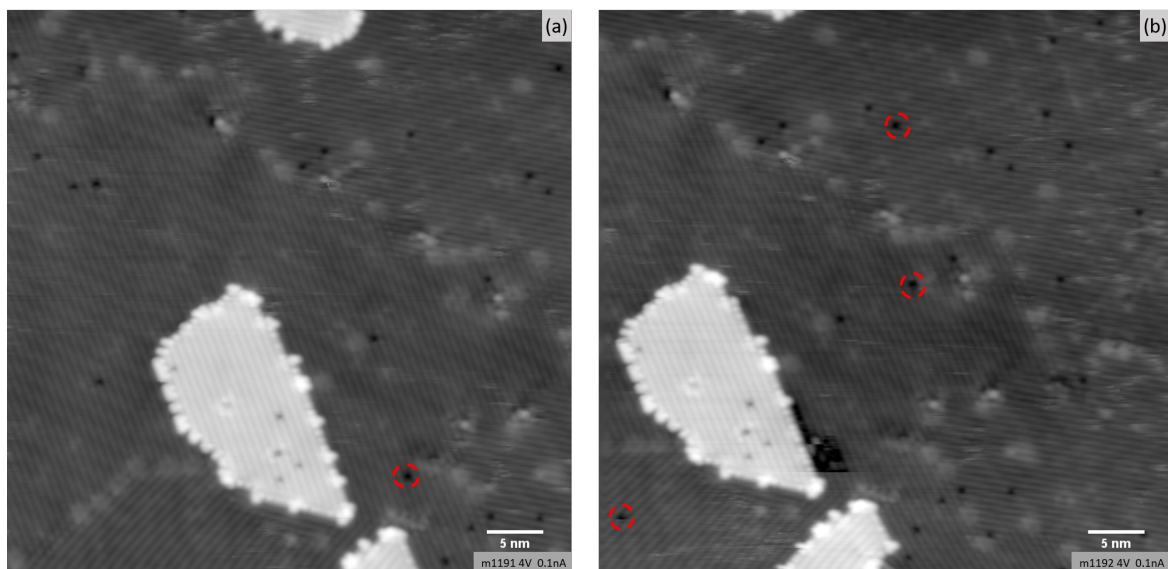
Figure 3.6: STM image of a 5 ML ZrO₂/Rh(111) film post-annealed in O₂ at 650 °C: (a) and (b) show two successive scanned images: A comparison of (a) and (b) reveals vanishing or moving defects/adatoms (red circles)

3.6 STM of Monoclinic ZrO$_2$ Phase

The monoclinic ZrO$_2$ film was prepared by post-annealing in O$_2$ atmosphere (p_{O_2} = $5 \cdot 10^{-8}$ torr (QMS)) at various temperatures up to $750\,°C$ for $10\,min$. The STM measurements were performed with voltages of 3.5–$5\,V$ and a tunneling current of $0.1\,nA$.

The STM measurements show a clear change of the oxide structure in comparison to the tetragonal ZrO$_2$ surface and hence a phase transition (Fig. 3.7). The surface appears smoother with fewer islands compared to the oxide surface in tetragonal phase. However, also holes down to the Rh(111) substrate could be detected, hence the oxide film breaks up. The reduction of the number of islands and the holes infer that the film thickness is increased to $6\,ML$. An FFT of Fig. 3.7 (a) reveals a (2×2) structure with respect to the cubic ZrO$_2$(111) structure (Fig. 3.7 (b)). Some spots appear distorted, which arises from rotated domains whose structure does not have the same lattice constant in the same direction (red circles). The horizontally blurred dots arise from the domain visible at the bottom left in Fig. 3.7 (a). The other domain has sharper dots in the FFT, which appear blurred in vertical direction. This characteristic fits to a monoclinic structure and the measured lattice constant lies in the range of bulk ZrO$_2$. Moreover, bright spots can be observed on the surface which could not be assigned to a known species.

It could be observed that the monoclinic surface is covered with features that appear fuzzy in the STM images and seem to strongly interact with the tip. Scanning the sample at higher voltages in the range of $6\,V$ removes the fuzzy features and provides a better resolution of the monoclinic oxide surface beneath. Fig. 3.8 (b) shows a 100×100 nm^2 area of the oxide which was scanned with $6\,V$. The surface is nicely resolved and a monoclinic structure is visible. Zooming out to a 200×200 nm^2 area and measuring with a bias voltage of $5\,V$ reveals that the fuzzy features had been removed on the area scanned at $6\,V$ (red box), but can not be removed while scanning at $5\,V$ (Fig. 3.8 (a)).

Looking at Fig. 3.8 (b) shows that the monoclinic oxide surface also contains many dark features, which arise from an unknown species or are defects.
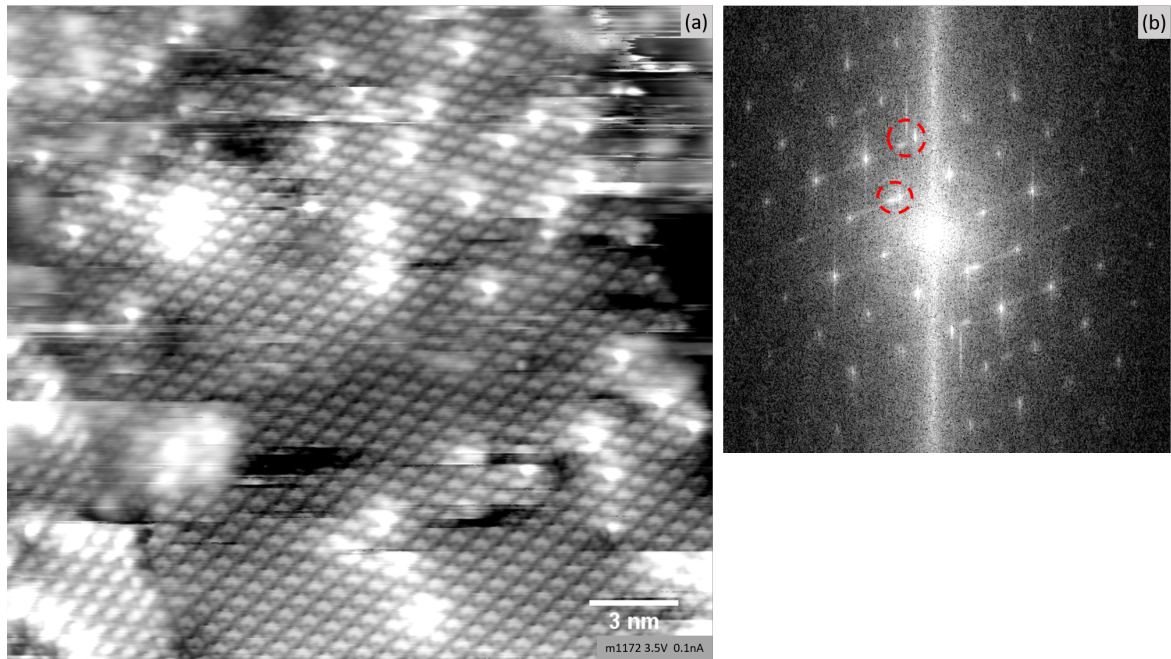
Figure 3.7: STM image of a 6 ML ZrO$_2$/Rh(111) film post-annealed in O$_2$ at 750 °C: (a) two different domains of the monoclinic ZrO$_2$ structure are visible. (b) FFT of (a) which reveals a (2×2) structure. The two domains are rotated with respect to each other (red circles). The sharp spots represents the main domain, wheras the blurred spots mark the small domain on the bottom left in (a)
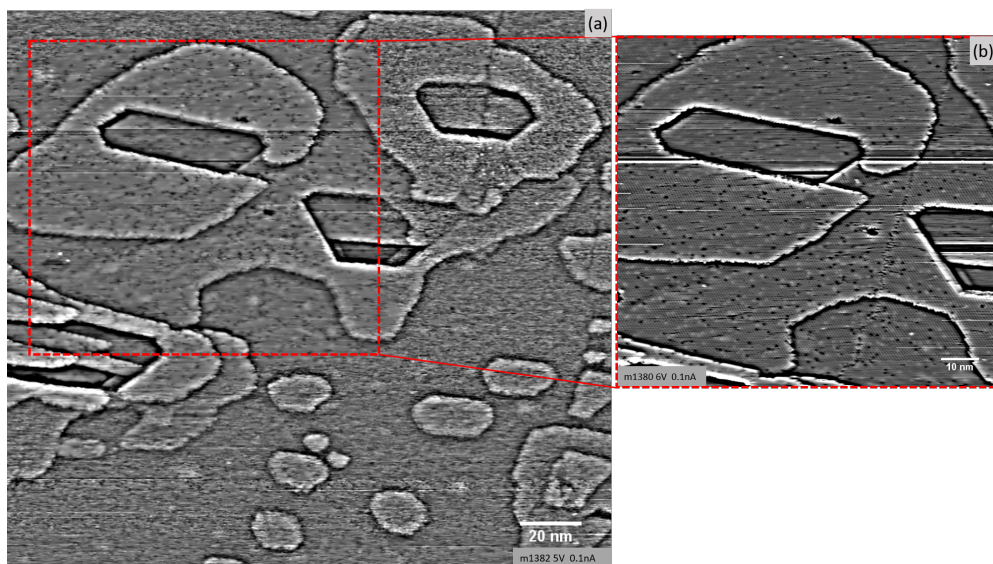
Figure 3.8: High pass filtered STM images of a 6 ML ZrO$_2$/Rh(111) film post-annealed in O$_2$ at 750 °C: a 100×100nm^2 area was scanned with 6 V, removing the fuzzy species (b). A successive scan with 5 V of a larger area, visible in (a) shows, that only the scanned area from before (b) is free of fuzzy features.

3.7 LEED of Tetragonal and Monoclinic ZrO$_2$

Additionally to STM measurements, LEED measurements were perfomed. With this technique the differences between tetragonal and monoclinic ZrO$_2$ are nicely visible. Fig. 3.9 (a) images the reciprocal space of a 5 ML thick tetragonal ZrO$_2$ film (post-annealed at 650 °C in oxygen atmosphere). The differently rotated domains cause an apparent (2×2) LEED pattern (blue rhomb marks the (1×1) cell). However, the domains are not exactly rotated by 120° with respect to each other, which results in blurred spots (edge of blue rhomb). The 6 ML thick monoclinic ZrO$_2$ film breaks, hence a Rh(111) signal is visible (red circle) in Fig. 3.9 (b). The spots of the different domains are slightly rotated to each other in contrast to the spots of the tetragonal domains, which arises from the different lattice constants of a monoclinic ZrO$_2$ structure.
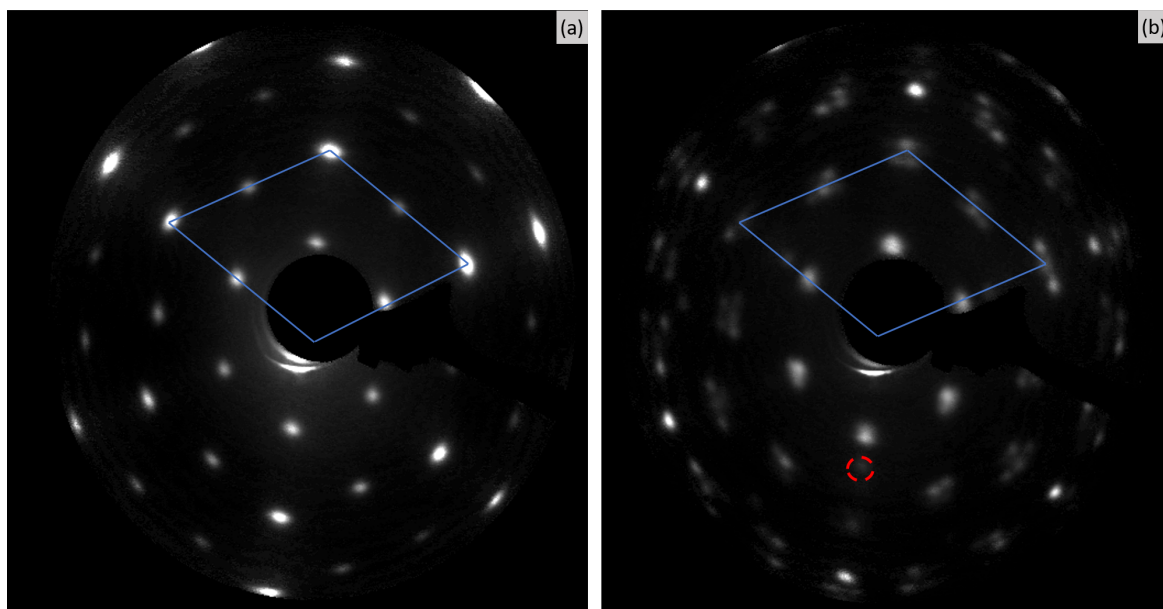
Figure 3.9: LEED of tetragonal (a) and monoclinic ZrO$_2$ (b) (Both images were measured with an electron beam energy of 70 eV): (a) A (2×2) structure is visible, which arises from the three overlapping domains (b) the different domain rotations are visible and since the lattice constant of monoclinic ZrO$_2$ varies, the domains do not overlap fully. The monoclinic ZrO$_2$ film breaks, which causes holes to the Rh(111) and therefore, spots arising from Rh(111) are visible (marked by a red circle).

3.8 XPS Studies of 5 ML Thick ZrO$_2$ Films and the Phase Transition

A 5 ML thick ZrO$_2$ film was deposited on Rh(111) using the Zr sputter source and was post-annealed in O$_2$ atmosphere ($p_{O_2} = 5 \cdot 10^{-8}$ torr (QMS)) for 4–20 min at increasing temperatures in the range of 500–750 °C to determine the temperature at which the film transforms from the tetragonal to the monoclinic structure. Investigations with XPS of the Zr 3d area reveal the formation of four different Zr species, which could be determined as metal Zr peak, interface peak, ZrO$_2$ peak (tetragonal ZrO$_2$ or monoclinic ZrO$_2$) and Zr-OH peak (Fig. 3.10 and Table 3.1).

Directly after deposition of the ZrO$_2$ film at room temperature, shown in Fig. 3.10 (a), the Zr 3d peak consists of five different peak doublets. The Zr 3d$_{5/2}$ interface peak (orange) is located at 180.5 eV, shifted by + 1.9 eV with respect to pure Zr, which correlates well with the trilayer peak presented in [22]. Moreover, the authors in [22] claim that the interface of thicker ZrO$_2$ films shows the same core level shift in XPS as a trilayer of ultra-thin ZrO$_2$. The main peak (green) is positioned at a binding energy of 183.4 eV, shifted by +4.8 eV with respect to pure Zr. Combined with the results of XPS, STM and LEED on post-annealed ZrO$_2$ surfaces, it could be determined as tetragonal ZrO$_2$. A smaller peak, located at 181.9 eV (shifted by + 2.3 eV w.r.t. pure Zr), almost exactly coincides with that of monoclinic ZrO$_2$ (see below). The peak, located at the highest binding energies, (blue) is positioned at 185.2 eV, shifted by + 6.6 eV with respect to pure Zr. Since the difference of the binding energies of the tetragonal ZrO$_2$ peak and this peak correlate with the results of [26], it seems likely that the peak (blue) arises from OH binding to Zr (N.B. as it is shown later, the Zr-OH peak will not arise from OH, but its name will not be changed). The smallest peak (purple) is located at 179.4 eV, shifted by +0.8 eV with respect to clean Zr. Since depositing metallic Zr on the clean Rh(111) at RT revealed the same peak shift of Zr 3d$_{5/2}$, the peak could be determined as metallic Zr on Rh(111). The metallic Zr is only present directly after deposition of ZrO$_2$. The Zr 3d peak locations change after annealing in O$_2$ atmosphere at 500 °C for 10 min. The metallic Zr and monoclinic-like ZrO$_2$ signal vanishes whereas the tetragonal ZrO$_2$ peak area increases, which means that the oxide consists of only one phase (Fig. 3.10 (c)). Moreover, the tetragonal zro peak and Zr-OH peak positions shift by 0.6 eV to lower binding energies. Annealing at 650 °C causes again changes of the peak positions (Fig. 3.10 (e)). The tetragonal ZrO$_2$ peak and the Zr-OH peak shift back to higher binding energies and are located at 183.2 eV and 184.8 eV, respectively, while the interface peak shifts slightly to lower binding energies. At this stage the STM measurements reveal that the domains of the tetragonal phase

become larger. Further annealing (750 °C for 10 min) leads to a clear peak shift of the main peak and the Zr-OH peak to lower binding energies, which are then located at 181.5 eV shifted by + 2.9 eV with respect to pure Zr and 183.1 eV shifted by + 4.5 eV, respectively (Fig. 3.10 (g)). The interface peak is placed at 180.2 eV. The STM measurements (see sections 3.5 and 3.6) confirm a phase transition of ZrO$_2$, thus the main peak could be determined as monoclinic ZrO$_2$. The area of the Zr-OH peak does not change, while the interface peak area decreases appreciably. However, it has to be noted, that the monoclinic ZrO$_2$ peak overlaps with the interface peak and a exact determination of the interface peak is therefore not possible.

Examining the O1 s peak area reveals two species of oxygen: the O 1s main peak and a smaller peak attributed to OH. It could be observed that the O 1s peak shifts similarly to the Zr 3d peak (Fig. 3.10 and Table 3.1).

Table 3.1: XPS peak properties of the four species of Zr 3d and the two species of O 1s after deposition at RT and annealing at different temperatures in $5 \cdot 10^{-8}$ torr O_2 (measured by QMS)

Peak Zr $3d_{5/2}$ (5 ML) BE	RT [eV]	500 °C [eV]	550 °C [eV]	650 °C [eV]	750 °C [eV]
Tetragonal ZrO_2	183.4	182.8	182.8	183.2	-
Monclinic ZrO_2	181.9	-	-	-	181.5
Interface	180.5	181.3	181.2	180.9	180.2
Zr-OH	185.2	184.5	184.4	184.8	183.1
Metal Zr	179.4				

Peak Zr $3d_{5/2}$ (5 ML) Area	RT [%]	500 °C [%]	550 °C [%]	650 °C [%]	750 °C [%]
Tetragonal ZrO_2	79	84	85	84	-
Monoclinic ZrO_2	4	-	-	-	88
Interface	10	11	10	10	6
Zr-OH	5	5	5	6	5
Metal-Zr	3				

Peak O 1s (5 ML) BE	RT [eV]	500 °C [eV]	550 °C [eV]	650 °C [eV]	750 °C [eV]
O1 s	531.2	530.5	530.6	530.9	529.5
O1 s - OH	533.1	532.4	532.1	532.9	531.6

Peak O1 s (5 ML) Area	RT [%]	500 °C [%]	550 °C [%]	650 °C [%]	750 °C [%]
O1 s	95	97	95	97	97
O1 s - OH	5	3	5	3	3

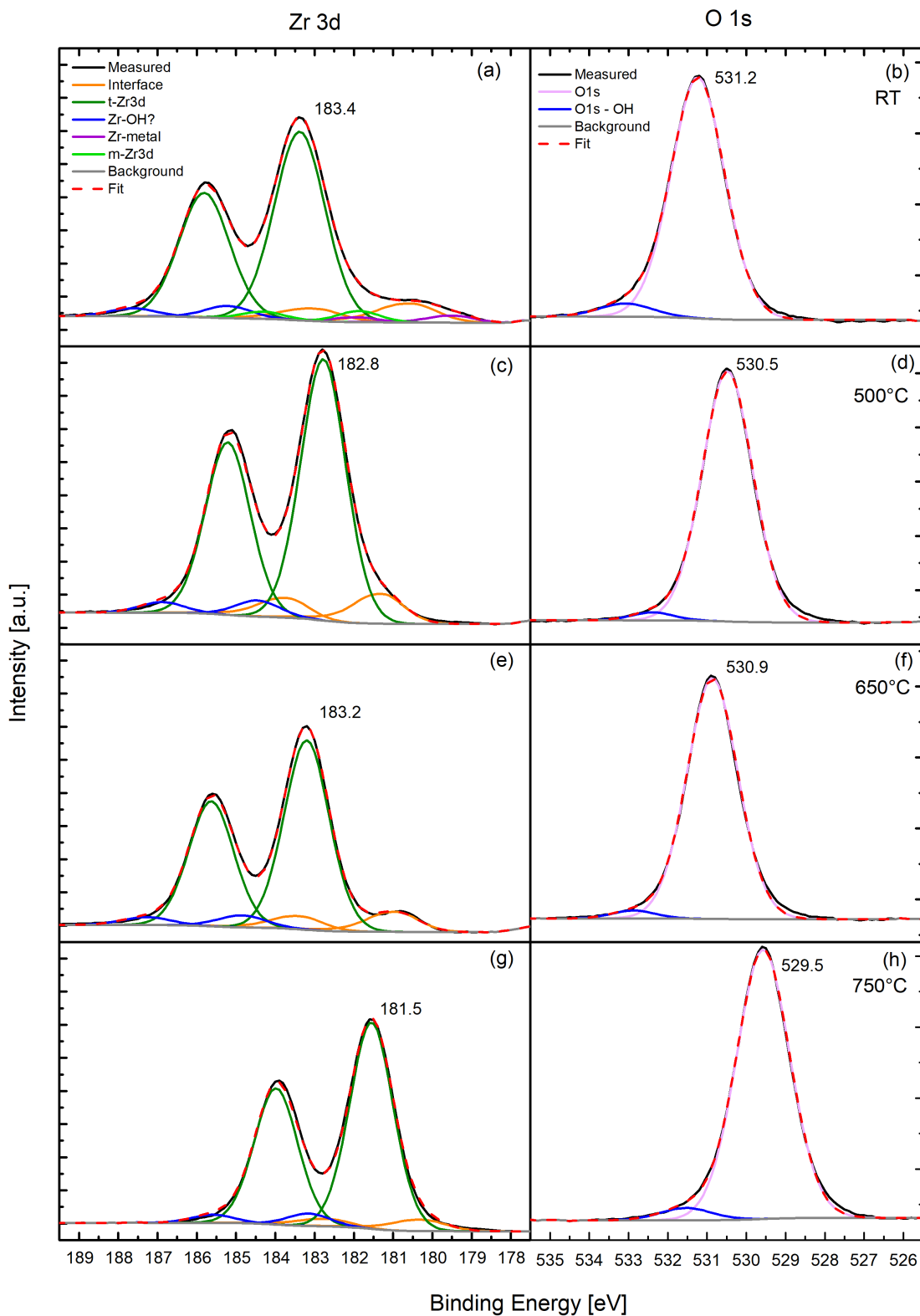| Ratio O/Zr	RT	500 °C	550 °C	650 °C	750 °C
	1.31	1.42	1.48	1.45	1.42

Figure 3.10: XPS fits of Zr 3d peaks (left column) and O 1s peaks (right column) after deposition of 5 ML ZrO₂ and different annealing temperatures. With: tetragonal ZrO₂ peak (t-Zr3d), monoclinic ZrO₂ peak (m-Zr3d), Zr-OH peak, metallic Zr peak (Zr-metal) and the interface peak (Interace)

3.9 Discussion

The STM measurements revealed that 5 ML thick ZrO$_2$ films, grown at RT and post-annealed in O$_2$ atmosphere, form a (2×1) structure with respect to cubic ZrO$_2$(111), with a lattice constant of 0.36 nm. It could be identified as tetragonal phase. Post-annealing in O$_2$ atmosphere influences the domain area size, which is increasing with higher temperatures up to an annealing temperature of 650 °C. Above an annealing temperature of 700 °C the phase starts to transform to the monoclinic phase. By means of STM measurements, a (2×2) structure could be distinguished. At first glance, the formation order of the ZrO$_2$ phases appears surprising, since bulk ZrO$_2$ is known to be stable in monoclinic phase at RT and transforms to the tetragonal phase only when annealed at much higher temperatures [12]. However, as mentioned in section 3.1, tetragonal ZrO$_2$ can be stabilized by alloying to other oxides [16] and it was claimed that the tetragonal phase can be favored at RT if the particle size is small enough [13]. Stable tetragonal nanoparticles at RT where found in [27]. These transform to the monoclinic phase above a particle size of 18 nm. Hence follows the assumption that the Rh(111) substrate stabilizes the thin tetragonal ZrO$_2$ films and a certain temperature is needed to overcome this stabilization and let the oxide transform into monoclinic ZrO$_2$.

Investigating ZrO$_2$ with XPS disclosed the phase transition in terms of the changing electronic structure, since the Zr 3d and O 1s peaks show clear peak shifts upon phase transition. Already Debasis and Dilip presented different spectra of Zr 3d and O 1s arising from changes in atomic coordination [28]. However, to compare tetragonal ZrO$_2$ with monoclinic ZrO$_2$, different materials were used in this study. For monoclinic ZrO$_2$ they used powder samples and for tetragonal powder, the study resorted to YSZ. The location of the Zr 3d$_{5/2}$ peak of tetragonal ZrO$_2$ (post-annealed at 650 °C) could be determined as 183.2 eV (B.E.), whereas monoclinic ZrO$_2$ showed a peak at 181.5 eV (-1.7 eV w.r.t. tetragonal ZrO$_2$). The Zr-OH peak shifts together with the tetragonal/monoclinic Zr 3d peak, whereas the interface peak experiences a shift of only 0.7 eV to lower binding energies by the transformation from tetragonal to monoclinic phase. However, as mentioned above, the interface peak position could only be estimated, since the monoclinic ZrO$_2$ peak is located to close to it. The Zr 3d$_{5/2}$ peak positions of the interface and tetragonal ZrO$_2$ distinguished on tetragonal ZrO$_2$ films are similar to the trilayer peaks and 3D cluster peaks on Pt$_3$Zr(0001), respectively, presented in [22] and moreover, the tetragonal ZrO$_2$ peak is similar to the multilayer ZrO$_2$ peak on Pt(111) [23]. A comparison of the peak areas shows that the interface peak ratio decreases after transforming the oxide to the monoclinic phase (Table 3.1). STM measurements show that the monoclinic ZrO$_2$ film breaks up and the oxide dewets the

substrate surface, which reduces the oxide area but the film thickness increases to 6 ML. According to this assumption and by a SESSA simulation [25] the signal decrease could roughly be estimated from $\approx 10\,\%$ (for tetragonal ZrO_2) to $\approx 6\,\%$ (for monoclinic ZrO_2), which correlates well with the results.

The Zr 3d peak shifts observed upon annealing the tetragonal ZrO_2 at lower temperatures (RT, 500 °C, 650 °C) do not offer such a clear explanation. XPS measurements directly after depositing ZrO_2 at RT reveal the formation of tetragonal ZrO_2. Moreover, metallic Zr could be found, which shows that the ZrO_2 is still not fully oxidized, which is also visible by studying the ratio between O 1s and Zr 3d (see Table 3.1). After annealing the oxide to 500 °C in O_2 atmosphere ($p_{O_2} = 5 \cdot 10^{-8}$ torr (QMS)) a peak shift of Zr 3d to lower binding energies can be observed. Furthermore, the metal Zr signals vanishes. The peak shift can be explained by a changing Fermi level, caused by not fully oxidized ZrO_2 at RT and a fully oxidized film after annealing in O_2 atmosphere. It is unlikely yet possible that the shift back to higher binding energies after annealing tetragonal ZrO_2 to 650 °C in O_2 atmosphere is caused by oxygen non-stoichiometry. However, no effect which causes the shift could be found yet.

4 Metal deposition on ZrO_2/Rh(111)

4.1 Previous studies

The deposition of metal clusters on ultrathin ZrO_2 films was already studied by STM and DFT calculations by Choi *et al.* [6]. They deposited Fe, Ni, Ag, Au and Pd on ultrathin ZrO_2 films grown by oxidation of $Pt_3Zr(0001)$ and $Pd_3Zr(0001)$. The STM studies reveal growth of different cluster sizes, depending on the metal-oxide interaction: The stronger the metal-oxide interaction (Fe≈Ni>Au≈Pd>Ag), the smaller the clusters. The cluster density increases with increasing reactivity of the metals towards oxygen, i.e. decreasing electronegativity of metals. Moreover, the wetting ability of metals increases with increasing reactivity. Au does not follow this trend, because it binds also to the Zr cations, where it becomes negative, in contrast to the other metals, which stay neutral or become positive. Moreover, it was observed that Ag and Pd grow as large 3D clusters and tend to nucleate on step edges and domain boundaries, whereas Fe and Ni form small clusters, consisting of few atoms, which prefer to grow on oxide terraces. The cluster density of Fe and Ni is high, which comes from strong interaction with the substrate.

DFT calculations for single adatoms on monoclinic ZrO_2 show that the metal-oxide interaction strength increases in the order of Ag<Au<Pd<Ni [6]. Choi *et al.* suggested that the cluster growth on nanoparticles and ZrO_2 bulk materials should show a similar behavior than the cluster growth on ultrathin ZrO_2 with some restrictions, though. A charge transfer between adatoms and the metal substrate is not possible on thicker ZrO_2 films.

The following sections should show wheater this assumption is justified and investigate the growth of Fe, Rh, Ag, and Au on 5–6 ML thick ZrO_2 films on a Rh(111) substrate. The cluster growth, density and height are studied on both tetragonal and monoclinic ZrO_2 by STM and XPS.

4.2 Sample Preparation and experimental methods

The oxide films were prepared with the Zr sputter source and post-annealed in O$_2$ atmosphere, as explained in section 3.3. It should be noted that the settings of the sputter-source and QMS were different for preparing the oxide films for depositing Fe than for the other metals (see Table 2.1: (a) settings for experiments with Fe; (b) settings for the experiments of the other metals). The metals were deposited using a triple evaporator from rods for Fe and Rh and from Mo crucibles for Ag and Au. During the evaporation of Au and Rh (except for one preparation of Rh), a repelling voltage of $+1.2\,\mathrm{kV}$ was applied at a tube electrode in front of rod or crucible to prevent fast ions from hitting the sample and sputtering the surface or causing defects. For the evaporation of Fe and Ag no repelling voltage was used. The sample was at RT during deposition of metals and the base pressure in the preparation chamber was below $2 \cdot 10^{-10}\,\mathrm{mbar}$. The other evaporation settings can be found in table 2.2.

The deposition rate was checked with a quartz crystal microbalance (QCM) before and after evaporating the metals to the sample. Note that the deposition rate of the metals is calculated in units of ML with respect to bulk ZrO$_2$. Thus 1 ML is defined as the number of atoms in a pseudomorphic monolayer with respect to bulk ZrO$_2$ (lattice constant of a $= 0.360\,\mathrm{nm}$), i.e. one atom per Zr atom in the ZrO$_2$ film ($1\,\mathrm{ML} = 8.91 \cdot 10^{18}\,\mathrm{m^{-2}}$). The metal cluster densities are given as clusters per m^2. To determine the real cluster density value, the distortion of the STM images must be considered, since the tip and the piezo electronics cause a thermal drift and a creep, respectively. A detailed description about the distortion method used in this work can be found elsewhere [5]. An undistortion of the images is only possible if the substrate lattice structure can be measured, which was not always possible. The average atoms per cluster are calculated from the amount of the deposited metal and the cluster density. Furthermore, all STM image sizes and cluster densities are given without correcting the inaccurate scanner calibration and therefore the values have to be divided by $\approx$ 1.1. Since the images are usually stretched in y-direction and compressed in x-direction, the error of the cluster densities is even less. The cluster heights on the 5 ML thick ZrO$_2$ films appear differently with different sample bias. Measuring with higher sample bias lets the oxide appear thicker, whereas the height difference between cluster and oxide decreases [29]. Since the apparent oxide thickness can not be calculated well, the cluster heights given in the following sections are apparent cluster heights.

The STM measurements were performed in constant current mode, with a tunneling current of 0.05–0.1 nA and positive sample bias voltages in the range of 1–6 V. The XPS measurements were performed with settings listed in Table 2.3.

4.3 Fe

Before presenting the results of Fe nucleation on tetragonal and monoclinic ZrO_2, it should be noted that the deposition of Fe was performed without applying a repelling voltage on the tube electrode in the evaporator, which should prevent that charged particles hit the sample. This may have influenced the preparation.

4.3.1 Fe on Tetragonal ZrO_2

To survey the growth of Fe on tetragonal ZrO_2, 0.05 ML and 1.25 ML Fe were deposited, which would correspond to 0.03 ML and 0.65 ML with respect to Fe(110) (N.B. deposition of 1.25 ML performed in several steps over two days).

Fig. 4.1 (a) and 4.2 (a) show STM images of tetragonal ZrO_2/Rh(111) after depositing 0.05 ML Fe. The cluster density is $6.4 \cdot 10^{16} \, \mathrm{m}^{-2}$. Fe forms small clusters which contain 7 atoms on average. The images were scanned with different voltages, 3.5 V and 3 V, respectively. The corresponding height distributions of the clusters (Fig. 4.1 (b) and 4.2 (b)) show a clear dependence on the tunneling voltage. The predominant height for Fig. 4.2 (a) is 150 pm, whereas the mean height determined in Fig. 4.2 (a) is 230 pm. The clusters appear higher while scanning with a lower voltage, which indicates that the Fe clusters are lying on top of the surface [23]. Clusters beneath the oxide surface do not change the apparent height with changing sample bias. The distribution of the clusters appears homogeneous and no tendency of growth on steps or at domain boundaries could be found. The clusters are reacting readily with the tip and interact more easily while scanning at lower sample bias, which can be seen in Fig. 4.2 (a), in which more cluster appear streaky. Moreover, a comparison between Fig. 4.1 (a) and 4.2 (a) shows that the clusters can be moved by the tip (red circles).

Fig. 4.2 (a) reveals a well resolved tetragonal surface (see inset). On a side note, in Fig. 4.1 (a) fuzzy features could be distinguished (on the left side, marked with a blue arrow), which were observed already on the clean monoclinic ZrO_2 surface (see section 3.6 and Fig. 3.8).

After depositing 1.25 ML Fe on ZrO_2/Rh(111), the surface appears fully covered by Fe clusters (Fig. 4.3 (a)). The height distribution in Fig. 4.3 (b) clearly indicates a 3D cluster growth.

XPS measurements show small shifts (+0.2 eV w.r.t. clean tetragonal ZrO_2) to higher binding energies of the tetragonal Zr 3d peak and O 1s after depositing 0.05 ML Fe, whereas no peak shifts could be distinguished after depositing 1.25 ML Fe (Fig. 4.5). However, the interface peak of Zr 3d shifts by only +0.1 eV after depositing 1.25 ML Fe, which lies within the error bars. The peak does not shift after depositing 0.05 ML Fe.

The Fe clusters do not strongly affect the electronic structure of the oxide, although the Fe 2p peak shifts by +3.5 eV and +0.6 eV (w.r.t. metallic Fe at 2p$_{3/2}$ 707 eV [24]) after depositing 0.25 ML and 1.25 ML Fe, respectively (Fig. 4.4). Moreover, it can be determined that the OH shoulder of the O 1s area is increasing after depositing 1.25 ML Fe.
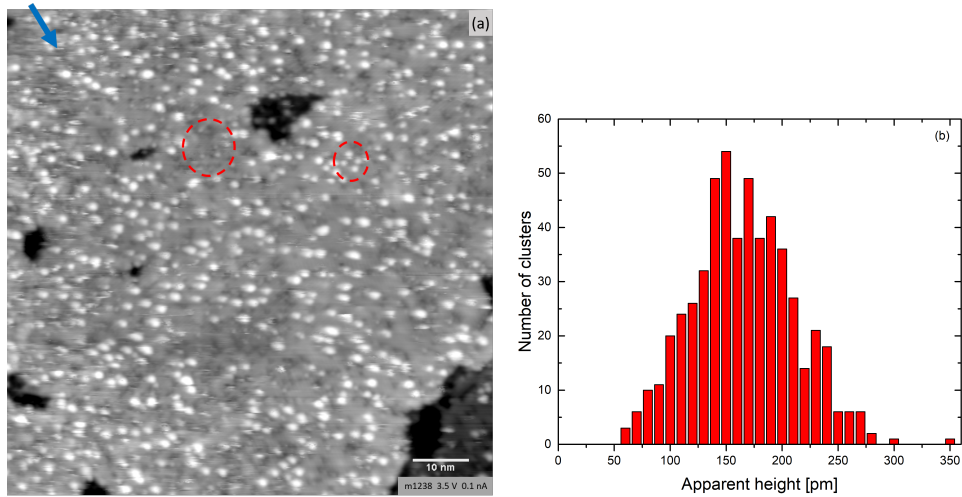
Figure 4.1: STM image of 0.05 ML Fe on tetragonal ZrO$_2$/Rh(111): (a) The Fe clusters are moving (red circles) and fuzzy features are found (blue arrow) (b) Cluster height distribution
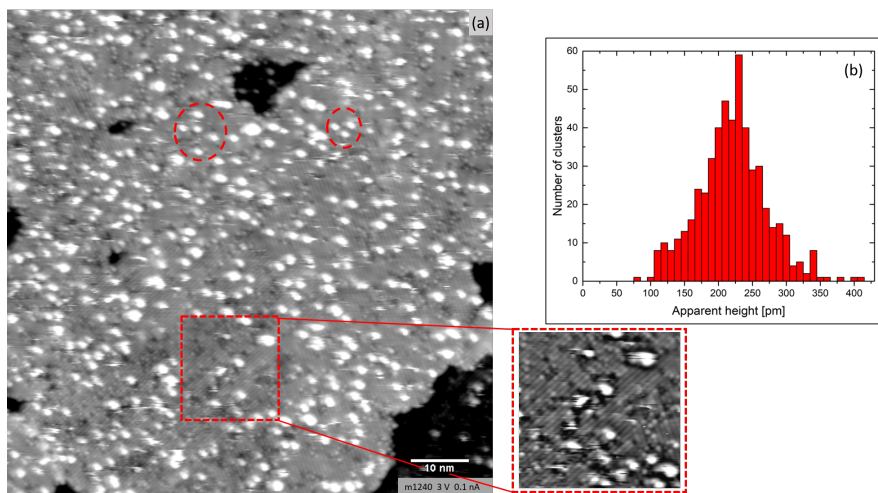
Figure 4.2: STM image of 0.05 ML Fe on tetragonal ZrO$_2$/Rh(111): (a) moving clusters can be distinguished by comparing with 4.1 (a) (red circles). The tetragonal structure is resolved. The inset shows a high pass filtered area for better visibility of the tetragonal structure. (b) cluster height distribution
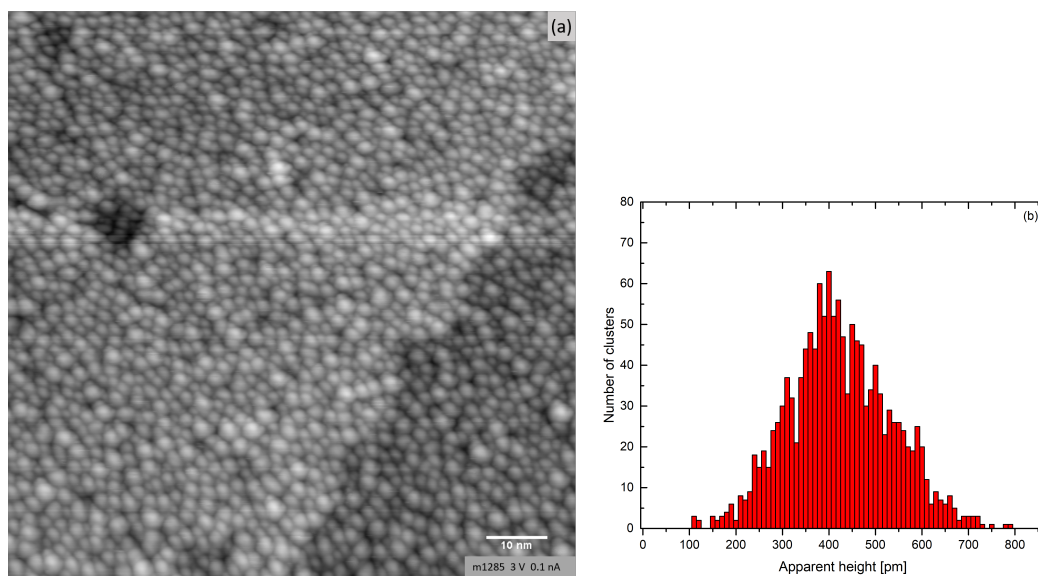
Figure 4.3: STM image of 1.25 ML Fe on tetragonal ZrO_2/Rh(111): (a) the oxide surface is fully covered by Fe clusters (b) cluster height distribution
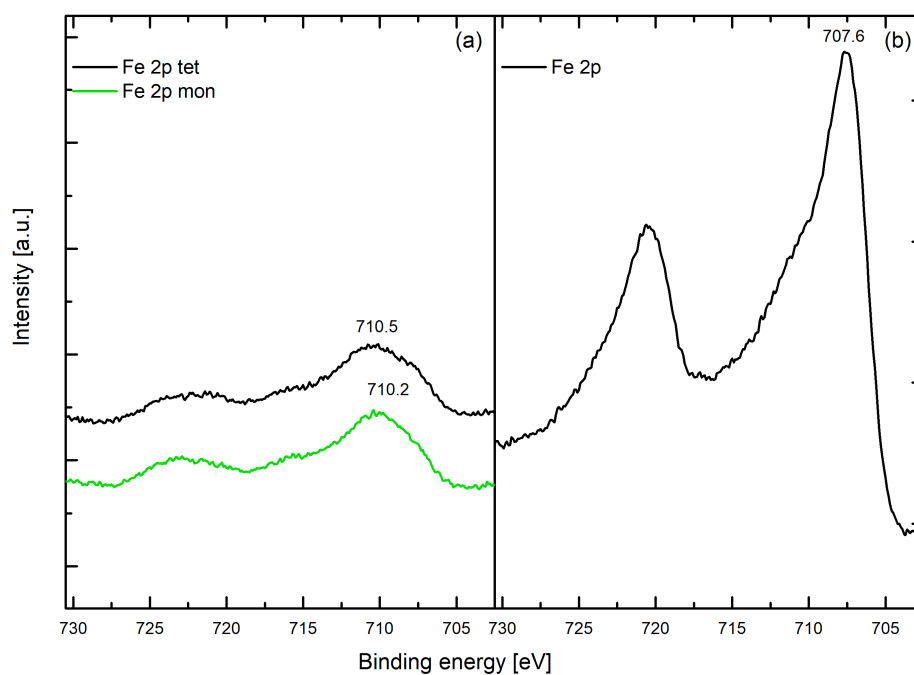
Figure 4.4: XPS spectra of Fe 2p after deposition of 0.25 ML Fe (a) and 1.25 ML Fe (b) on tetragonal ZrO_2/Rh(111) and 0.25 ML Fe on monoclinic ZrO_2/Rh(111) (a) in green ($E_{pass} = 50\,eV$)
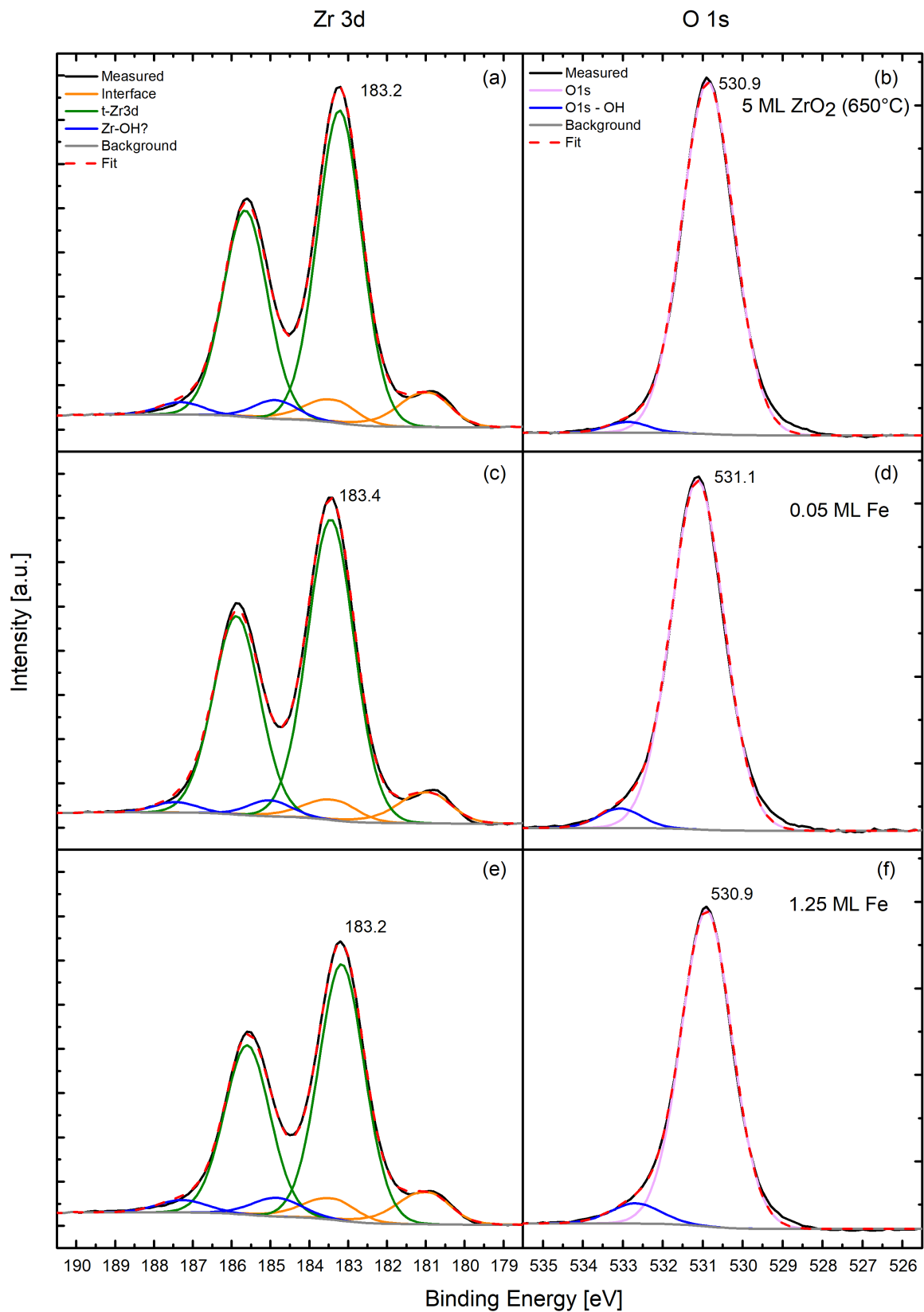
Figure 4.5: XPS fits of Zr 3d peaks (left column) and O 1s peaks (right column) after deposition of 5 ML ZrO₂ (post-annealed at 650 °C) (a),(b), 0.05 ML Fe (c),(d) and 1.25 ML Fe (e),(f). The peak positions of tetragonal ZrO₂ Zr 3d$_{5/2}$ and O 1s are shown next to the peaks

4.3.2 Fe on Monoclinic ZrO$_2$

To study the growth of Fe on monoclinic ZrO$_2$, 0.05 ML and 0.25 ML Fe was deposited, which corresponds to a coverage of 0.03 ML and 0.13 ML with respect to Fe(110), respectively.

Fig. 4.6 shows a nicely visible monoclinic ZrO$_2$ surface with Fe clusters on top. The clusters do not appear to grow preferentially at domain boundaries and a cluster density of $5.3 \cdot 10^{16} \, \text{m}^{-2}$ is determined, which leads to an average number of 8 atoms per cluster. The height distribution reveals a predominant height of 170 pm.

Fig. 4.8 (a) and 4.9 (a) show the oxide surface after depositing 0.25 ML Fe. A cluster density of $6.4 \cdot 10^{16} \, \text{m}^{-2}$ is determined and it can be estimated that the average cluster contains 35 atoms. The height distribution of Fig. 4.8(b) reveals 3D growth of the clusters and mean cluster height of 440 pm (Fig. 4.9(b)). Regarding the oxide structure Fig. 4.8(a) shows a smooth monoclinic surface. Furthermore, no holes and defects can be distinguished, also the bright features observed on the clean monoclinic ZrO$_2$ surface (see Fig. 3.7) vanished. The clusters show no tendency of growing at step edges or domain boundaries (Fig. 4.9(a)). Moreover, the clusters seem to appear different, depending on the terrace on which they are growing. The clusters in Fig. 4.9(a) interact with the tip more easily on the lower terrace and seem to be moved strongly from the tip, whereas the clusters on the topmost terrace do not move or strongly interact with the tip. This effect is most likely caused by a double tip or an artefact of the tip. The height distribution of Fig. 4.9(a) considers only the clusters on the topmost terrace and shows a 3D growth (Fig. 4.9(b)).

Fig. 4.7 shows the monoclinic ZrO$_2$ with a large hole to the Rh substrate. The different growth mode on the oxide and on the Rh(111) substrate is nicely visible. Fe forms small round-shaped clusters on the oxide and the height distribution shows 3D cluster growth (Fig. 4.9(b)). On Rh(111) however, Fe tends to wet the surface and forms 2D-islands, with an apparent height of 150 pm.

XPS measurements show a clear peak shift of Zr 3d after deposition of Fe. The monoclinic Zr 3d peak is located at 182.6 eV binding energy, which is a shift of +1.1 eV to higher binding energies with respect to clean monoclinic ZrO$_2$ (Fig. 4.10). Moreover, the peak shift caused by the phase transition from tetragonal to monoclinic ZrO$_2$ is shown. The O 1s area reveals a similar shift than Zr 3d (+0.9 eV). Both peaks (Zr 3d and O 1s) change their peak shape after deposition of Fe and become broader, which indicates a change in the electronic structure. The full width at half maximum (FWHM) of the monoclinic Zr 3d peak changes from 1.3 eV to 1.7 eV. An analysis of the Fe 2p peak area after depositing 0.25 ML Fe shows that the peak shifts by +3.2 eV with

respect to pure Fe (peak position of pure Fe $2p_{3/2}$ = 707 eV [24]) and has the same peak shape as Fe on tetragonal ZrO_2 (Fig. 4.4).

Note: The preparation of 0.05 ML Fe on ZrO_2/Rh(111) was different to the other preparations in this chapter. The oxygen pressures during annealing were between $4.3 \cdot 10^{-8}$–$4.7 \cdot 10^{-9}$ torr compared to $5 \cdot 10^{-8}$ torr in the other preparations. XPS confirmed that the oxide did not change compared to the other preparations.
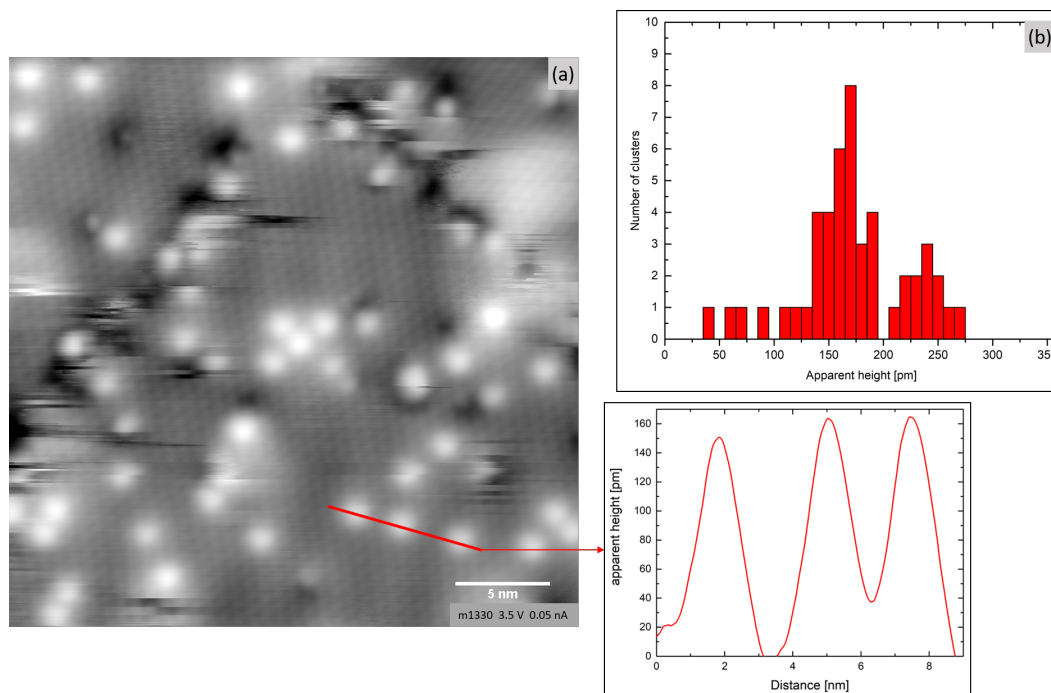
Figure 4.6: (a) STM image of 0.05 ML Fe on monoclinic ZrO_2/Rh(111) with a line profile over Fe clusters (inset below). (b) Cluster height distribution.
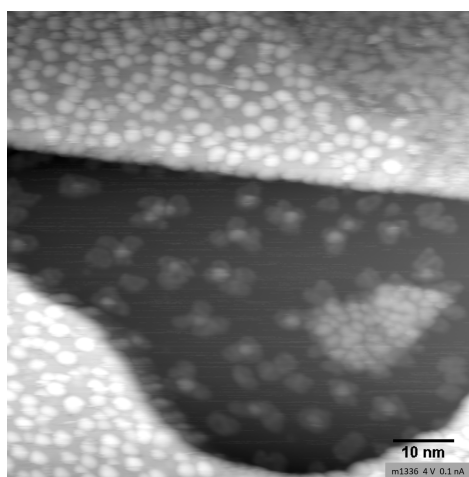
Figure 4.7: STM image of 0.25 ML Fe on monoclinic ZrO_2/Rh(111): Fe forms small rounded clusters on the oxide, whereas it wets the surface on Rh(111) and forms 2D islands
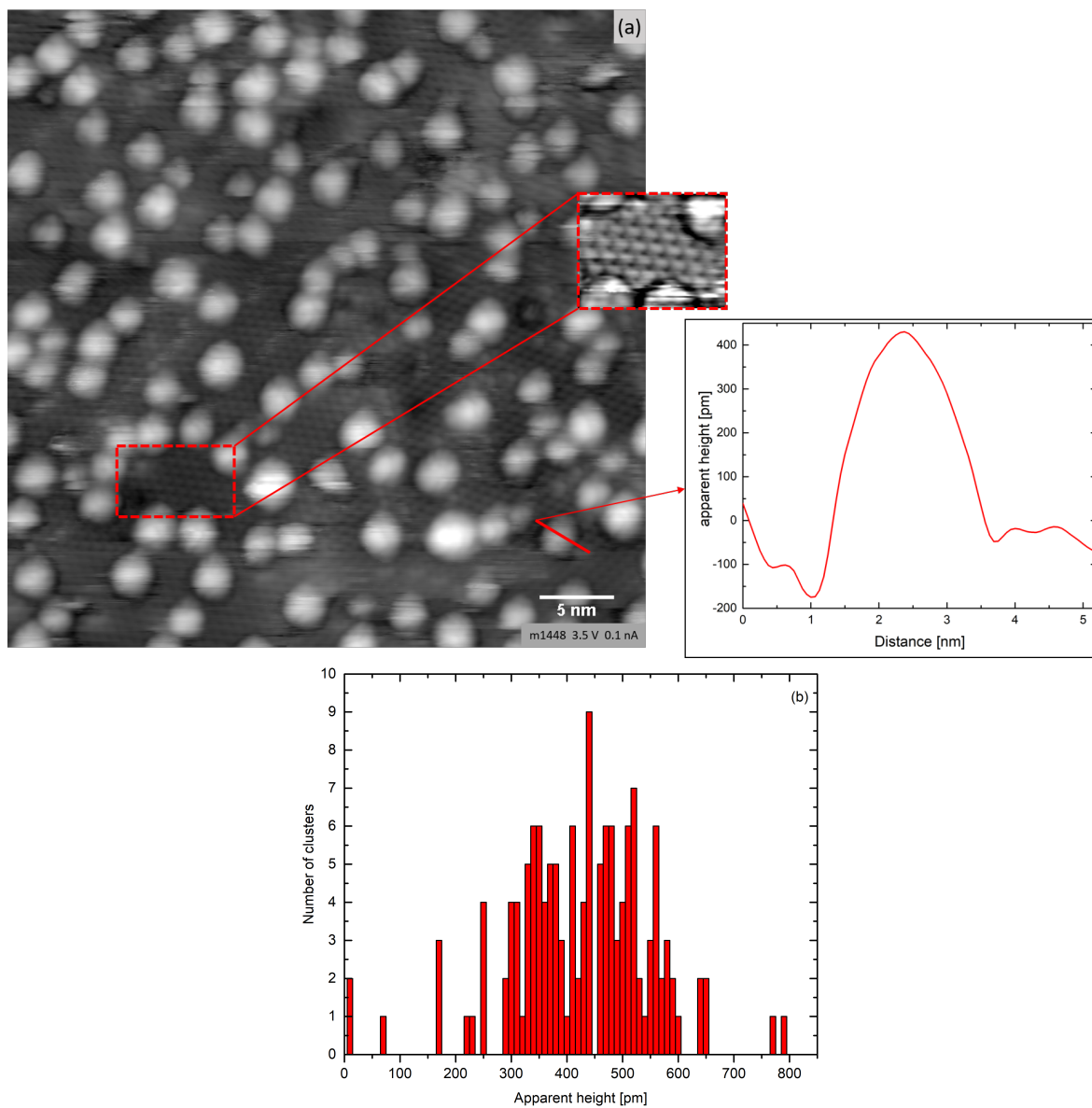
Figure 4.8: (a) STM image of $0.25\,\mathrm{ML}$ Fe on monoclinic $ZrO_2/Rh(111)$. The monoclinic structure is visible (inset). (b) Cluster height distribution.
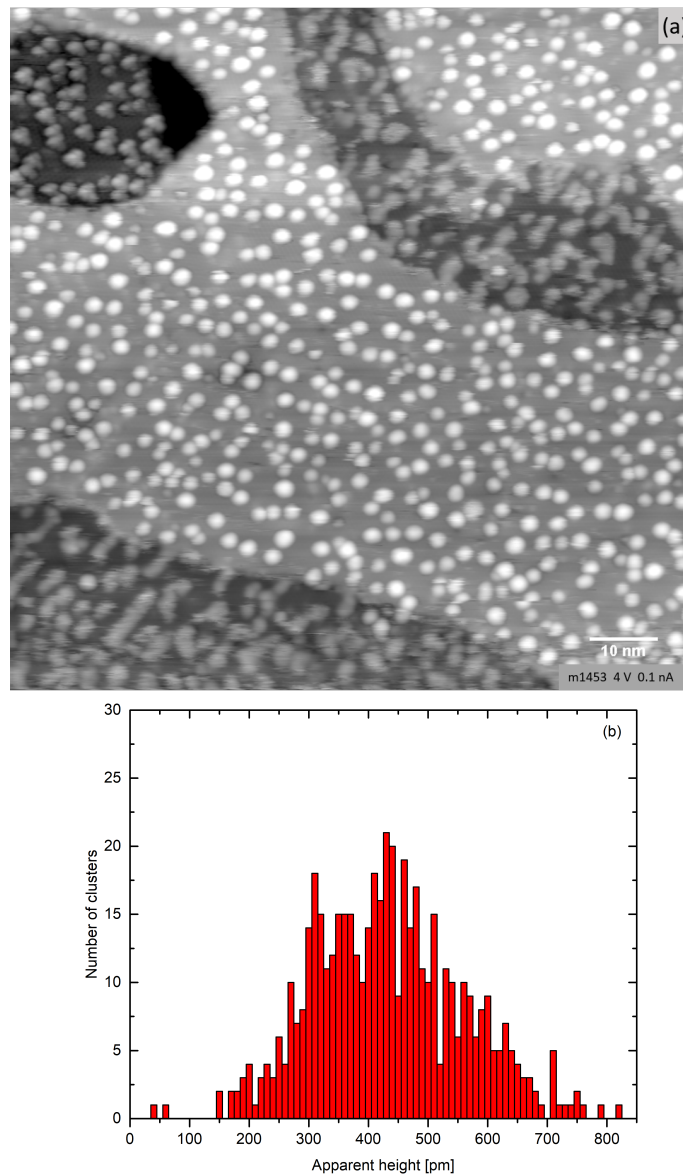
Figure 4.9: (a) STM image of $0.25\,\text{ML}$ Fe on monoclinic $ZrO_2/Rh(111)$: The clusters on the topmost terrace are nicely imaged, whereas the clusters on the other terraces appear streaky, which is most likely due to a tip artefact. (b) Cluster height distribution of the Fe clusters on the topmost terrace.
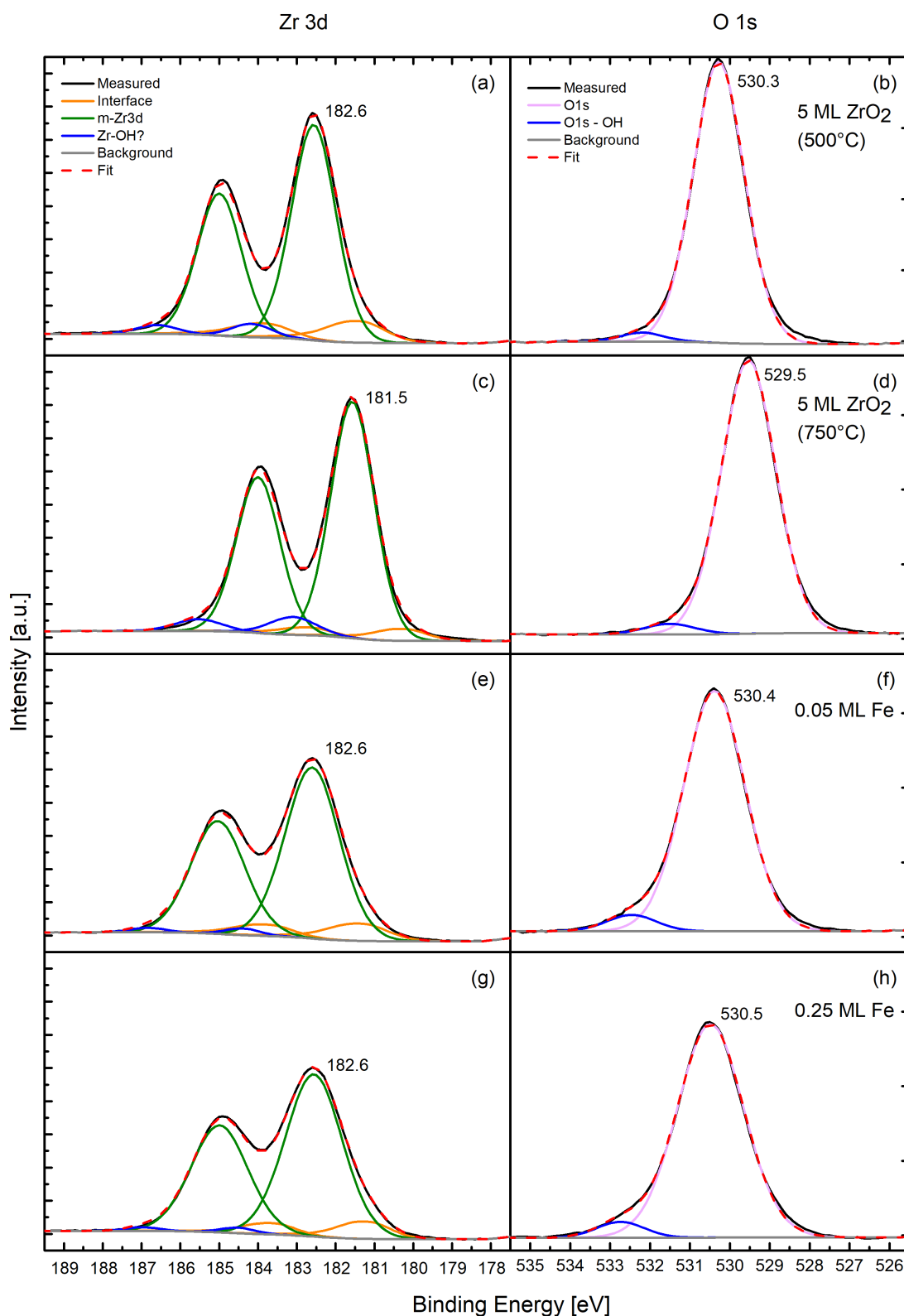
Figure 4.10: XPS fits of Zr 3d peaks (left column) and O 1s peaks (right column) after deposition of 5 ML ZrO$_2$ (post-annealed at 500 °C) to get tetragonal ZrO$_2$ (a),(b), 5 ML ZrO$_2$ (post-annealed at 750 °C) to prepare monoclinic ZrO$_2$ (c),(d), 0.05 ML Fe (e),(f) and 0.25 ML Fe (g),(h). The peak positions of monoclinic ZrO$_2$ Zr 3d$_{5/2}$ and O 1s are shown next to the peaks

4.3.3 Discussion: Fe growth on ZrO$_2$

The studies of Fe cluster growth on tetragonal and monoclinic ZrO$_2$ reveals surprising differences. At first glance the growth mode of Fe clusters appears similar, since the cluster density is in the same range for a coverage of 0.05 ML Fe and the cluster sizes differ only slightly ZrO$_2$ (Table 4.2). The clusters become larger with higher coverage. The differences in cluster heights can be explained by the different tunneling voltages (3 V and 3.5 V for Fe on tetragonal ZrO$_2$ and monoclinic ZrO$_2$, respectively). However, the clusters show different behaviors while performing STM measurements. Whereas the clusters are very mobile and get moved by the tip on tetragonal ZrO$_2$, the clusters do not show the same strong interaction on the monoclinic ZrO$_2$ surface, which could be explained by a stronger bonding to the oxide on the monoclinic ZrO$_2$ surface.

The XPS results reveal a remarkable difference between the two preparations. Fe on tetragonal ZrO$_2$ influences the electronic structure of the oxide weakly. Fe on monoclinic ZrO$_2$, however, causes a strong peak shift of Zr 3d and O 1s to higher binding energies (+1.1 eV for Zr 3d). The fact that the peaks are broadening indicates also that the metal clusters are changing the electronic structure on this surface and support the results of STM, which indicate a strong bonding of Fe. The Fe 2p peak reveals a strong shift by $\approx$+3.3 eV to higher binding energies on both phases after depositing 0.25 ML Fe, which indicates that Fe is charging. By depositing more (1.25 ML) Fe, it appears to be more like metallic Fe, according to its peak position (shifted by +0.6 eV w.r.t. pure Fe).

A comparison with the growth of Fe clusters on ultrathin ZrO$_2$ films on ZrO$_2$/Pt$_3$Zr presented in [6] reveals a clear difference. The cluster density on the ultrathin ZrO$_2$ films is approximately four times higher ($24 \cdot 10^{16}$ m^{-2} [6] vs. $6.4 \cdot 10^{16}$ m^{-2} on monoclinic ZrO$_2$), which results in fewer estimated average atoms per cluster (7 on ultrathin ZrO$_2$). However, the predominant heights are in the same range for ultrathin, tetragonal and monoclinic ZrO$_2$.

4.4 Ag

Before presenting the results of Ag nucleation on tetragonal and monoclinic ZrO$_2$, it should be noted that the deposition of Ag was performed without applying a repelling voltage on the tube electrode in the evaporator, which should prevent that charged particles hit the sample. This may have influenced the preparation.

4.4.1 Ag on Tetragonal ZrO$_2$

The cluster growth of Ag on 5 ML thick tetragonal ZrO$_2$ films on Rh(111) was examined by depositing 0.05 ML, 0.1 ML and 0.23 ML Ag (w.r.t. ZrO$_2$). These coverages correspond to 0.02 ML, 0.05 ML and 0.1 ML, respectively, with respect to Ag(111).

Fig. 4.11(a) shows the tetragonal ZrO$_2$ surface after deposition of 0.05 ML Ag. It can be observed that the Ag clusters grow in two tifferent types. The bigger clusters reveal a predominant height of 640 pm, whereas the mean height of the smaller Ag clusters is determined as 380 pm (Fig. 4.11(b)). Scanning at a lower sample bias (below 3 V) causes a strong interaction between the Ag clusters and the tip, which can be identified by streaky clusters. It is even possible to pick up clusters with the tip if the sample bias is low enough (in the range of 1.5 V) or move them to the side of the scanned area. The Ag clusters reveal a tendency to grow on steps edges, which is also observed in Fig. 4.11(c), where 0.1 ML Ag was deposited. The cluster density of $2.7 \cdot 10^{16}$ m^{-2} leads to 34 atoms per cluster on average. The corresponding height distribution shows a predominant cluster height between 490–720 pm (Fig. 4.11(d)).

The cluster density is increasing with increasing Ag coverage of from $1.2 \cdot 10^{16}$ m^{-2} at 0.05 ML to $2.7 \cdot 10^{16}$ m^{-2} at 0.1 ML. However, after depositing 0.23 ML Ag (Fig. 4.11(e)) mainly the Ag cluster sizes are increasing, whereas the cluster density of $3.2 \cdot 10^{16}$ m^{-2} does not change remarkably compared to a coverage of 0.1 ML. The height distribution in Fig. 4.11(f) reveals Ag clusters which appear several layers thick and at least five different cluster heights, of which no height is predominant. The peaks are separated by 200–280 pm, which roughly matches the interlayer distance of Ag(111) (235.9 pm). Due to an artifact of the STM tip, the large Ag clusters are distorted in one direction.

The XPS measurements performed on each preparation show that the Zr 3d region does not change substantially after depositing Ag on the oxide (Fig. 4.12). The peak shifts of Zr 3d by -0.1 eV and O1 s by ± 0.1 eV after a deposition of 0.23 ML Ag may be caused by repeated post-annealing (at 500 °C) of the oxide before depositing Ag. Furthermore, it can be determined that the OH peak increases when depositing Ag. This increase is not due to time the prepared sample spent in UHV, where the contamination through the residual gas increases with time. XPS was performed before and after leaving the prepared sample in the UHV chamber, which revealed no increase of the OH signal. The Ag 3d peak is shifted by +0.5 eV and +0.3 eV (w.r.t. pure Ag 3d$_{5/2}$, which is located at 368.3 eV [24]) after deposition of 0.1 ML and 0.23 ML Ag (Fig. 4.13).
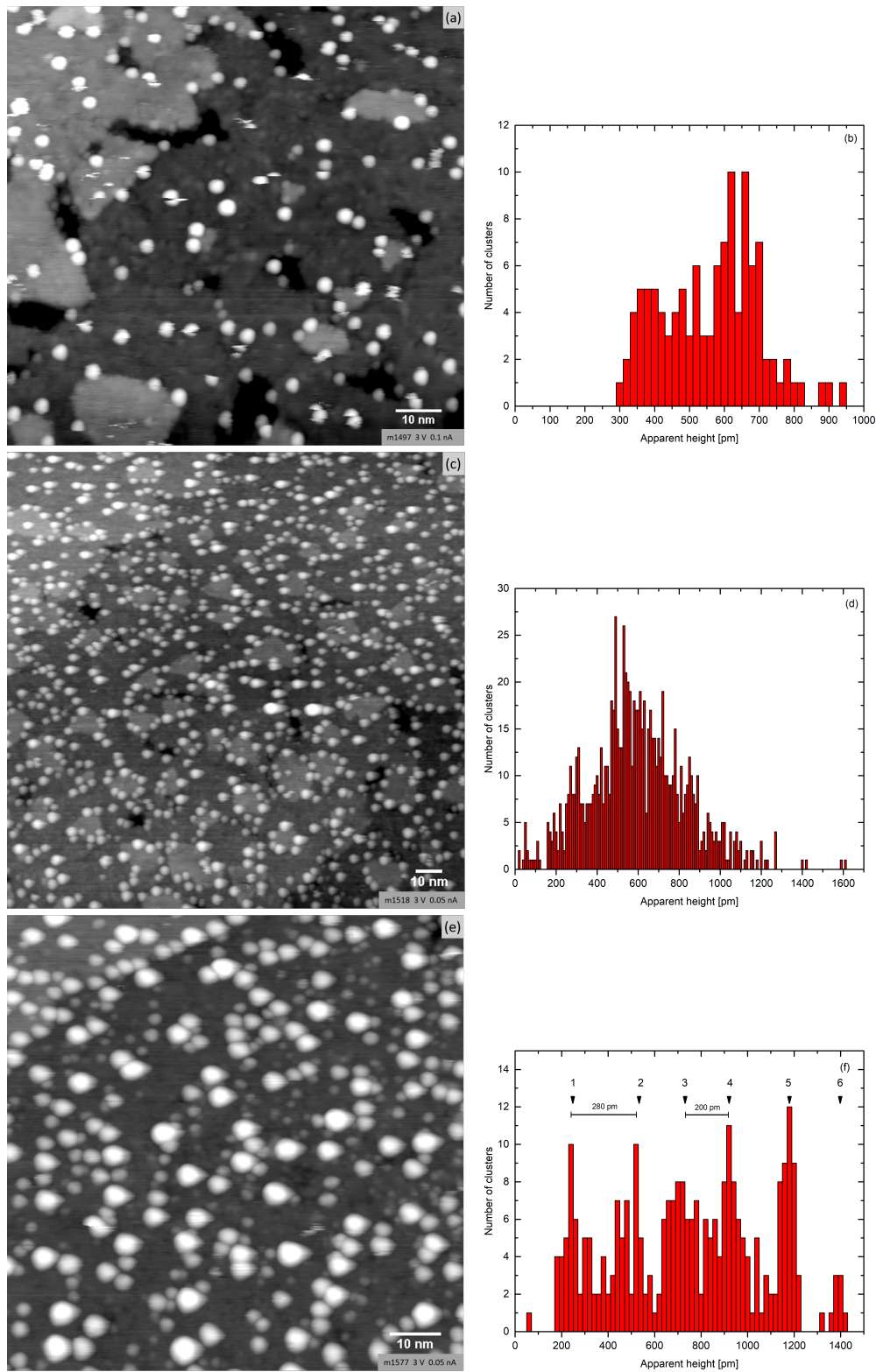
Figure 4.11: STM images of Ag deposited on tetragonal $ZrO_2/Rh(111)$: (a) 0.05 ML Ag. (b) cluster height distribution of (a). (c) 0.1 ML Ag: The clusters tend to grow at step edges. (d) cluster height distribution of (c). (e) 0.23 ML Ag: Cluster growth at step edges is visible (top left). (f) Cluster height distribution of (e): The peak spacing roughly fits the Ag interlayer distance
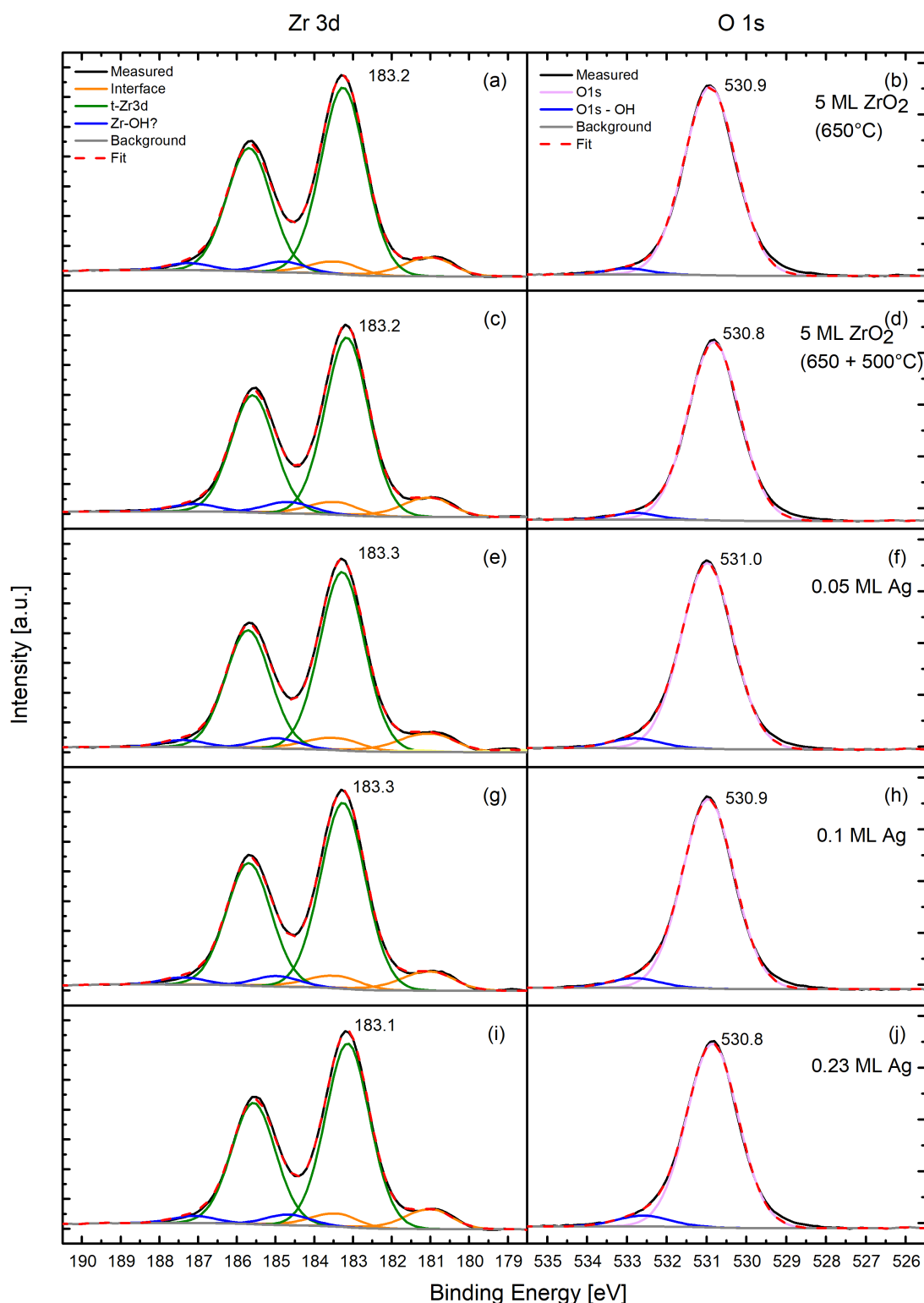
Figure 4.12: XPS fits of Zr 3d peaks (left column) and O 1s peaks (right column) after deposition of 5 ML ZrO$_2$ (annealed at 650 °C) to get tetragonal ZrO$_2$ (a),(b), 5 ML ZrO$_2$ (post-annealed at 500 °C the next day to clean the surface from contaminations of the residual gas after a night in UHV) (c),(d), 0.05 ML Ag (e),(f), 0.1 ML Ag (g),(h) and 0.23 ML Ag (i), (j). The peak positions of tetragonal ZrO$_2$ Zr 3d$_{5/2}$ and O 1s are shown next to the peaks.
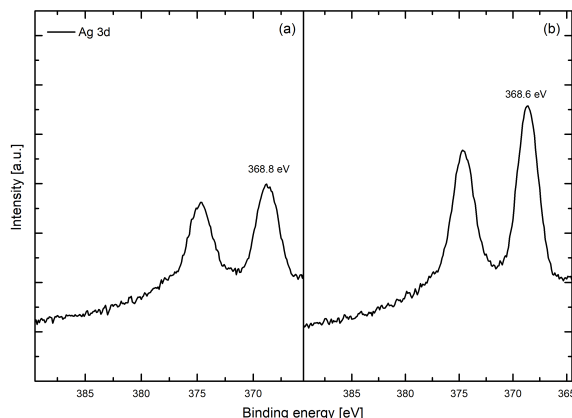
Figure 4.13: XPS spectra of Ag 3d after deposition of $0.1\,\mathrm{ML}$ Ag (a) and $0.23\,\mathrm{ML}$ Ag (b) on $\mathrm{ZrO_2}$/Rh(111) ($E_{pass} = 50\,\mathrm{eV}$)

4.4.2 Ag on Monoclinic ZrO₂

To study the growth of Ag on monoclinic $\mathrm{ZrO_2}$, $0.1\,\mathrm{ML}$ and $0.2\,\mathrm{ML}$ Ag were deposited, which correspond to $0.05\,\mathrm{ML}$ and $0.09\,\mathrm{ML}$ with respect to Ag(111). Fig. 4.14(a) - 4.14(c) show the same region of the oxide after deposition of $0.2\,\mathrm{ML}$ Ag, scanned with different sample bias. Ag clusters are found mainly on the topmost terraces; the clusters are very large. Therefore, the cluster density is relatively low ($0.49 \cdot 10^{16}\,\mathrm{m^{-2}}$) and leads to estimated 364 atoms per cluster. The height distribution in Fig. 4.14(d) shows that the cluster height is in the range of mainly 700–1700 pm, which indicates a 3D cluster growth. Because of the few clusters, a height distribution with reasonable statistics can not be presented. Moreover, the clusters and the tip are strongly interacting, which results in moving clusters and can be observed in Fig. 4.14(a) - Fig. 4.14(c). It shows a cluster on the right edge, marked by a red circle, which is moved by the tip to the step edge. Fig. 4.14(b) shows the cluster, which is moved while scanning and in Fig. 4.14(c) the cluster is stable at the step edge. The clusters do not grow on domain boundaries, which is visible in 4.14(b) (marked by green dotted box). Additional STM measurements of a different region reveal that the clusters show a tendency of growing at step edges (Fig. 4.15).

XPS reveals a peak shift of Zr 3d and O 1s to higher binding energies (Fig. 4.17). After deposition of $0.1\,\mathrm{ML}$ Ag the monoclinic Zr 3d and the Zr-OH peak shift by $+0.4\,\mathrm{eV}$ with respect to clean monoclinic $\mathrm{ZrO_2}$. The monoclinic Zr $3d_{5/2}$ peak is now located at $181.9\,\mathrm{eV}$ and Zr-OH Zr $3d_{5/2}$ at $183.5\,\mathrm{eV}$. Both peaks shift further by $+0.1\,\mathrm{eV}$ after deposition of $0.2\,\mathrm{ML}$ Ag. Also the interface peak shifts by $+0.2\,\mathrm{eV}$ to higher binding energies. The O 1s peak shows the same behavior and shifts by $+0.4\,\mathrm{eV}$ and $+0.5\,\mathrm{eV}$ after depositing $0.1\,\mathrm{ML}$ and $0.2\,\mathrm{ML}$ Ag, respectively. However, the O 1s-OH peak shifts

only by $+0.1\,\mathrm{eV}$ and $+0.2\,\mathrm{eV}$, respectively. Moreover, its peak area slightly increases when depositing Ag. The Ag 3d peak is not shifted with respect to bulk Ag(111), as shown in Fig. 4.16.
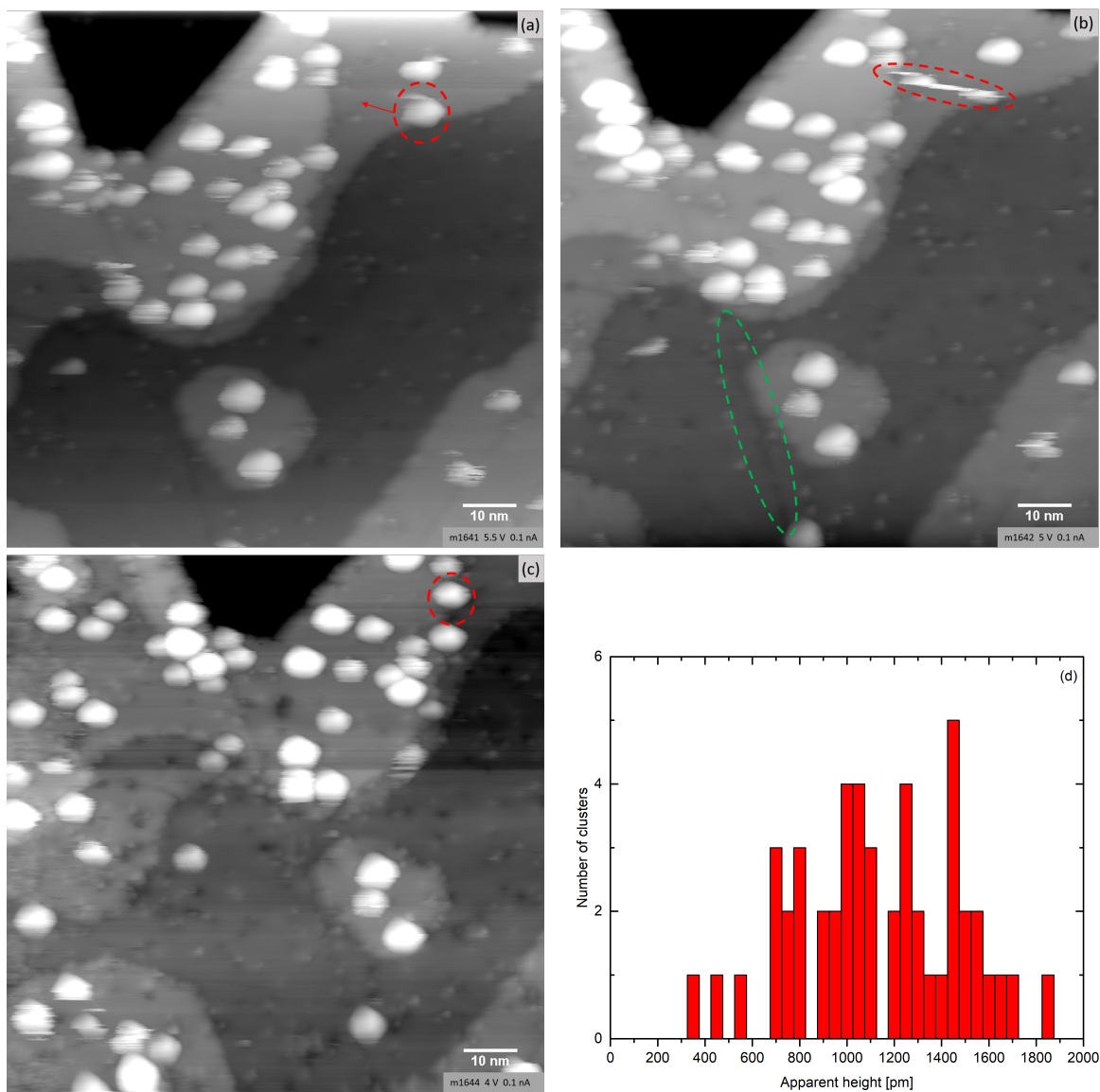
Figure 4.14: (a)-(c) STM images of $0.2\,\mathrm{ML}$ Ag on monoclinic $\mathrm{ZrO_2/Rh(111)}$, which show the movement of an Ag cluster: (a) A cluster is visible at a terrace (red circle), which is then moved by the tip (b) to the step edge (c). The cluster do not tend to grow on domain boundaries (green dotted line in (b)). (d) cluster height distribution of (c).
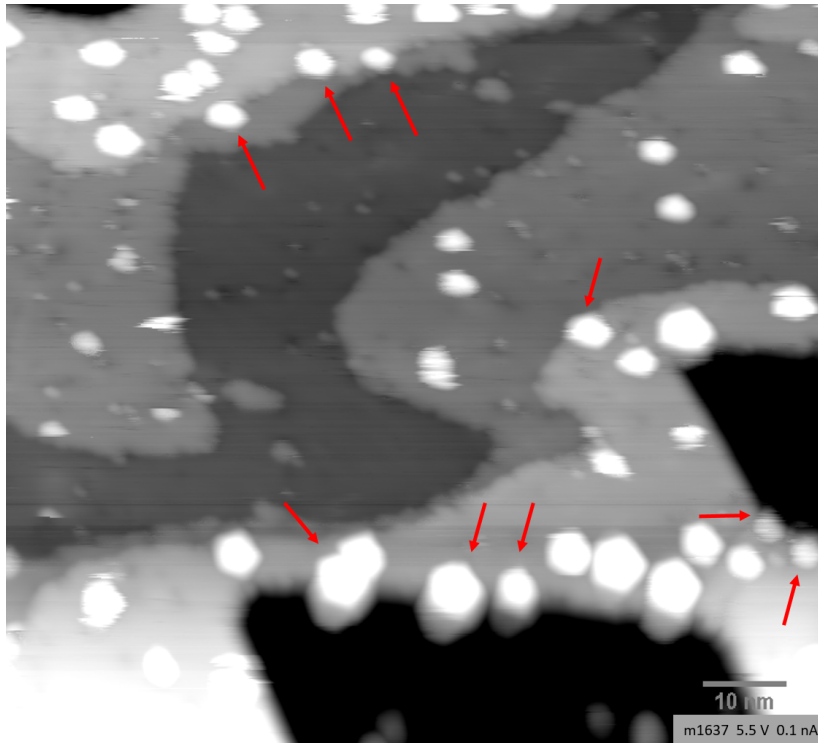
Figure 4.15: STM image of 0.2 ML Ag on monoclinic ZrO$_2$/Rh(111): The clusters tend to grow at step edges (red arrows)
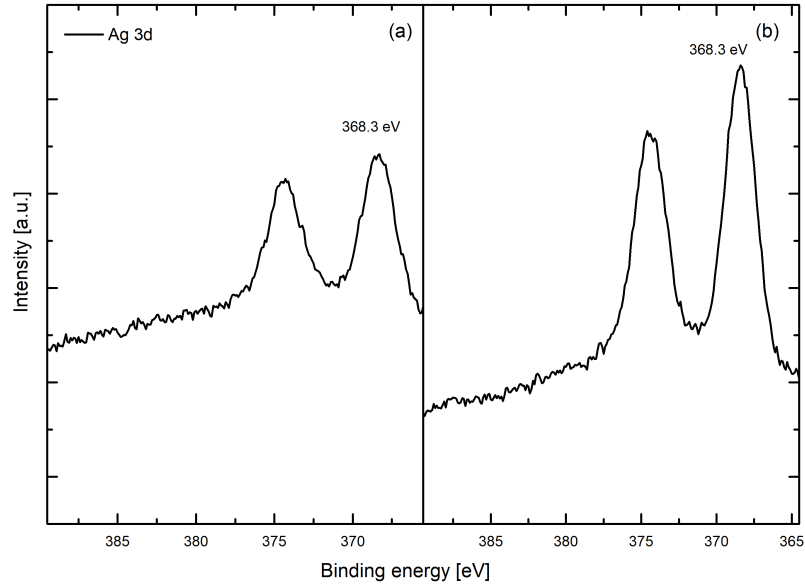
Figure 4.16: XPS spectra of Ag 3d after deposition of 0.1 ML Ag (a) and 0.2 ML Ag (b) on monoclinic ZrO$_2$/Rh(111) ($E_{pass} = 50$ eV)
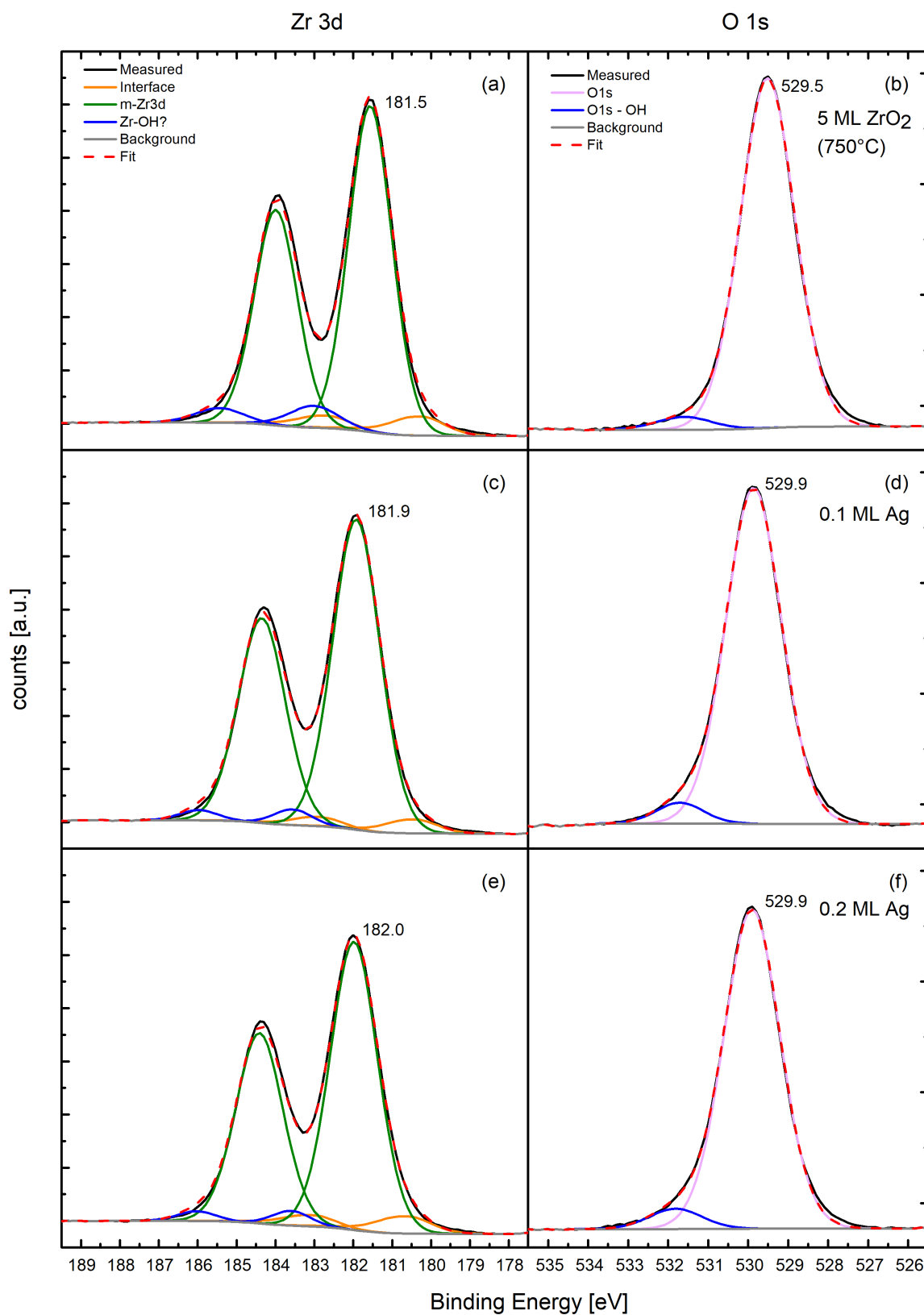
Figure 4.17: XPS fits of Zr 3d peaks (left column) and O 1s peaks (right column) after deposition of 5 ML ZrO_2 (post-annealed at 750 °C) (a),(b), 0.1 ML Ag (c),(d) and 0.2 ML Ag (e),(f). The peak positions of monoclinic ZrO_2 Zr $3d_{5/2}$ and O 1s are shown next to the peaks.

4.4.3 Discussion: Ag growth on ZrO₂

Examining the growth mode of Ag on tetragonal and monoclinic ZrO_2 reveals many differences. The cluster density of Ag on the monoclinic ZrO_2 surface is approximately six times smaller than on tetragonal ZrO_2 ($0.49 \cdot 10^{16} \, \mathrm{m}^{-2}$ vs. $3.19 \cdot 10^{16} \, \mathrm{m}^{-2}$ after deposition of $0.2 \, \mathrm{ML}$ and $0.23 \, \mathrm{ML}$ Ag, respectively), which results in fewer but bigger clusters on monoclinic ZrO_2. The clusters do not show a single predominant height in both phases. The cluster heights on monoclinic ZrO_2 are in the range of 700–1700 pm, whereas Ag the cluster heights on tetragonal ZrO_2 are typically below 1230 pm. The higher cluster density and smaller cluster height on tetragonal ZrO_2 lead to the assumption of a stronger interaction to the oxide than on monoclinic ZrO_2. However, the clusters show a similar behavior by interacting with the STM tip. It is possible to move a cluster under tip influence on both surfaces while scanning at a lower sample bias (in the range of 1 V). Furthermore, the clusters tend to grow at step edges on both ZrO_2 phases, which indicates a stronger metal-oxide interaction at the edges. Since the oxide atoms at step edges offer more broken bonds than atoms on terraces, Ag binds more likely on the lower terrace. The cluster movement in Fig. 4.14(a) - 4.14(c) confirms this assumption, since the cluster became immobile when finally bound at a step.

The XPS measurements reveal a stronger change of the electronic structure of ZrO_2 affected by Ag on monoclinic ZrO_2, where Zr 3d and O 1s shift about $+0.4$–$0.5 \, \mathrm{eV}$ (w.r.t. clean monoclinic ZrO_2) to higher binding energies. The oxide peaks do not shift significantly on tetragonal ZrO_2. However, both phases show an increase of the OH peak area of the O 1s region when depositing Ag. The Ag 3d peak, however, shows a shift by $+0.5 \, \mathrm{eV}$ on tetragonal ZrO_2, but no shift on monoclinic ZrO_2, which apparently correlates with the cluster sizes. The smaller Ag clusters and higher cluster density on tetragonal ZrO_2, lead to a larger interface between oxide and Ag clusters and hence, to a stronger peak shift in XPS.

The Ag growth mode on thicker ZrO_2 films shows similarities to the growth on ultra-thin films on ZrO_2/Pt_3Zr and ZrO_2/Pd_3Zr, which was investigated in [6]. Ag shows a preference of growing on step edges on all four oxide surfaces. However, on ZrO_2/Pt_3Zr clusters grow also on domain boundaries, which was not seen on the thicker oxide films. Similar to the growth of Ag on tetragonal ZrO_2, different cluster heights, which differ by the interlayer Ag distance could be distinguished on ZrO_2/Pt_3Zr. This was not observed on ZrO_2/Pd_3Zr. However, the cluster densities and therefore also the estimated atoms per cluster differ (Tab 4.1). In fact, similarities between tetragonal ZrO_2 and ZrO_2/Pd_3Zr and between monoclinic ZrO_2 and ZrO_2/Pt_3Zr can be determined.

Table 4.1: Comparison of deposition of Ag on tetragonal (tet) and monoclinic (mon) $ZrO_2/Rh(111)$ and ultra-thin ZrO_2/Pt_3Zr and ZrO_2/Pd_3Zr

Surface	tet	mon	ZrO_2/Pt_3Zr [6]	ZrO_2/Pd_3Zr [6]
Cluster coverage [ML]	0.23	0.2	0.26	0.15
Cluster density [$10^{16}\,m^{-2}$]	3.19	0.49	0.53	5.3
Average atoms/cluster	64	364	464	26
predominant apparent height [pm]	700	1100	1400	700

4.5 Au

4.5.1 Au on Tetragonal ZrO_2

The growth of Au clusters on tetragonal ZrO_2 was examined by depositing 0.1 ML and 0.2 ML Au w.r.t. ZrO_2 (0.064 ML and 0.13 ML, respectively, w.r.t. Au(111)). Analyzing the STM measurements of 0.2 ML Au on tetragonal $ZrO_2/Rh(111)$ shows an average cluster density of $4.6 \cdot 10^{16}\,m^{-2}$. This leads to 39 atoms per cluster on average.

Fig. 4.18 shows 0.1 ML Au on the tetragonal $ZrO_2/Rh(111)$ film (Insets of Fig. 4.18(d) and 4.19(a)) with a cluster density of $3.3 \cdot 10^{16}\,m^{-2}$, which leads to an average of 27 atoms per cluster. Two types of Au clusters can be identified (Line profiles of Fig. 4.18(a) and 4.19(a)), in which the smaller clusters represent the majority with a predominant cluster height of 340 pm at 3 V tunneling voltage (Fig. 4.18(c) and 4.18(d)). Comparing the height distributions of Fig. 4.18(b) and 4.18(c), a dependency of the cluster height on the applied sample bias can be determined. The clusters appear higher at lower sample bias, which confirms that Au is growing on top of the oxide surface and not beneath [23]. The cluster size increases after depositing 0.2 ML Au (Fig. 4.19) and the peaks in the cluster height distribution (Fig. 4.19(b)) change to 430 pm and 770 pm (scanned with 2.9 V). The clusters nucleate on terraces and at step edges. Moreover, they do not tend to grow at domain boundaries. The tetragonal structure, which can be seen in all images, reveals more holes and defects than the clean tetragonal ZrO_2 surface, although a repelling voltage was applied to the tube electrode of the evaporator while depositing Au to prevent sputtering of the oxide by charged particles. Fig. 4.18 and 4.19 show that the clusters interact with the tip and can be moved, which suggests a weak bonding of the clusters to the ZrO_2 film.

XPS reveals an interesting behavior of the Zr 3d area after deposition of Au (Fig. 4.20). After depositing 0.2 ML Au, the peaks shift to lower binding energies and the tetragonal Zr $3d_{5/2}$ peak is then positioned at 182.9 eV, -0.3 eV shifted with respect to clean

tetragonal ZrO$_2$ (Note: the oxide was post-annealed at 650 °C and 500 °C, which caused already a slight peak shift to lower binding energies of -0.1 eV). The Zr-OH peak shifts together with the tetragonal peak, whereas the interface peak does not shift. The O 1s peak area shows the same shift as Zr 3d of -0.3 eV and is then located at 530.6 eV. The ratio between O 1s main peak and OH-related peak changes by depositing Au on the oxide and the OH-peak increases. The Au 4f peak shifts by -0.2 eV with respect to pure Au (84 eV[24]) (Fig. 4.21(a)).
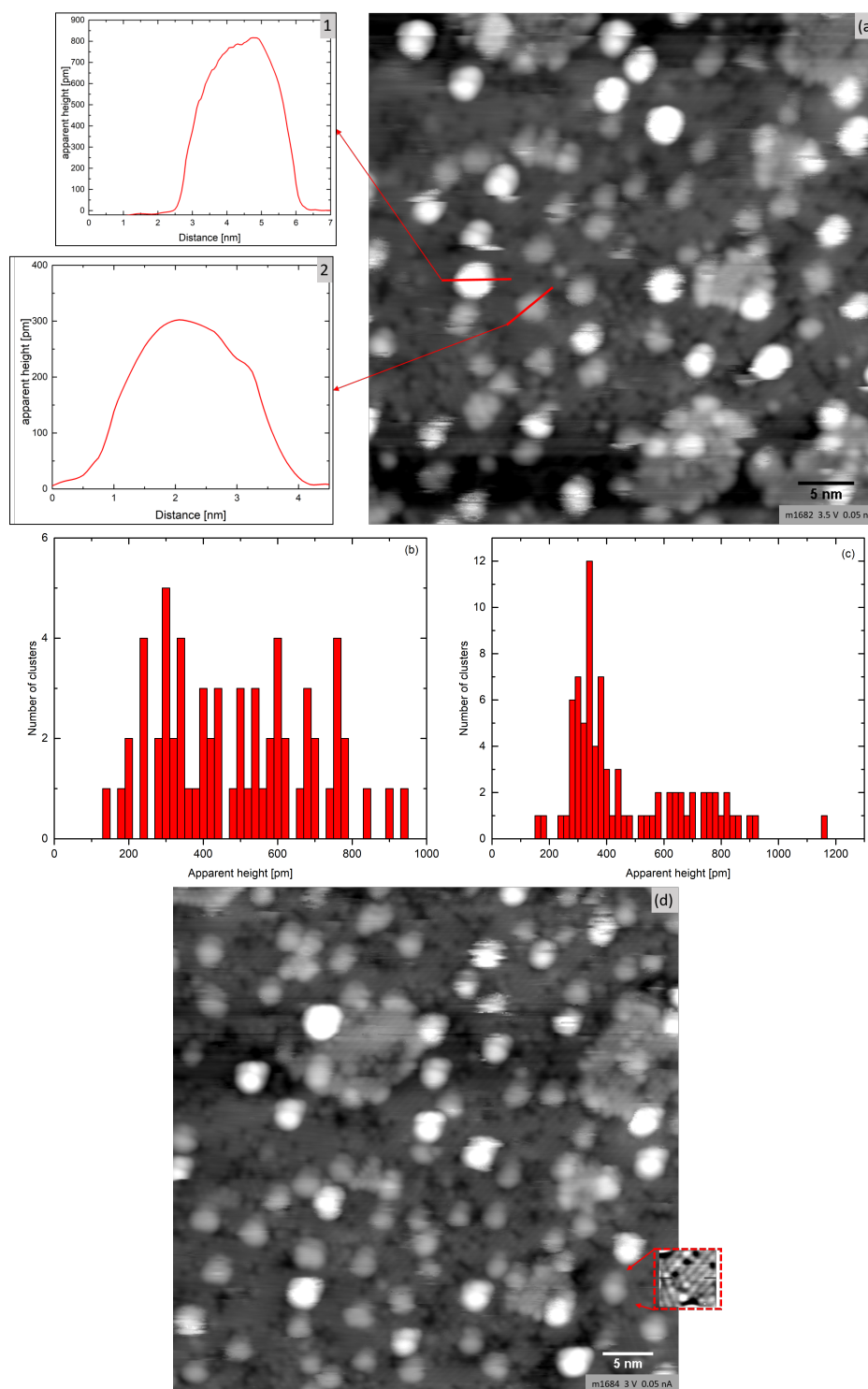
Figure 4.18: STM image of 0.1 ML Au on tetragonal ZrO_2/Rh(111): (a) The clusters grow as smaller clusters (line profile 2) and larger clusters (line profile 1). (b) Cluster height distributions of (a). (c) Cluster height distribution of (d) (d) The clusters grow at step edges and on terraces. The tetragonal structure is shown in the inset.
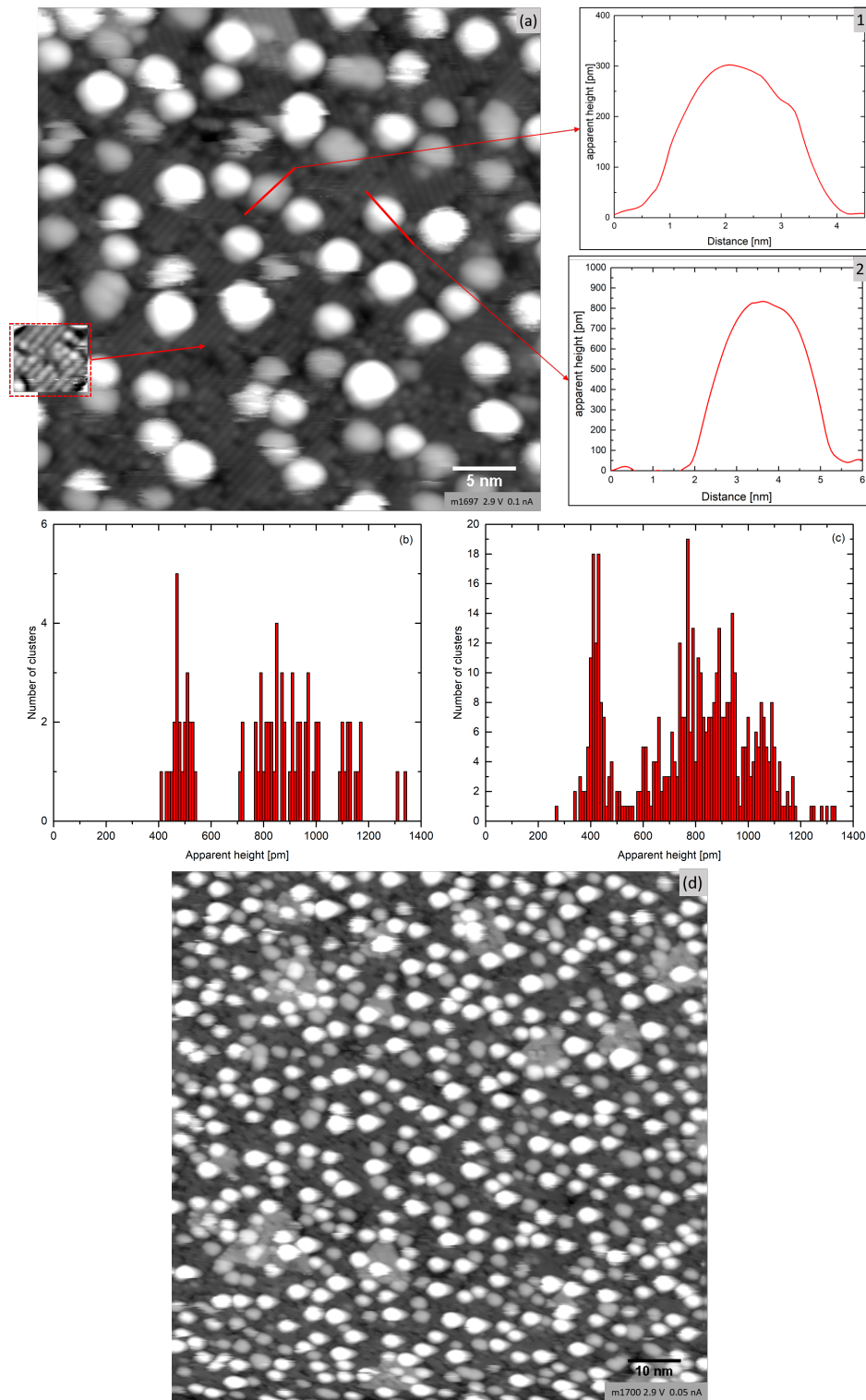
Figure 4.19: STM image of 0.2 ML Au on tetragonal ZrO_2/Rh(111): (a) More larger Au clusters are forming (line profile 2) than smaller Au clusters (line profile 1). The tetragonal structure is shown in the inset. (b) Cluster height distributions of (a). (c) Cluster height distribution of (d) (d) The clusters grow at step edges and on terraces.
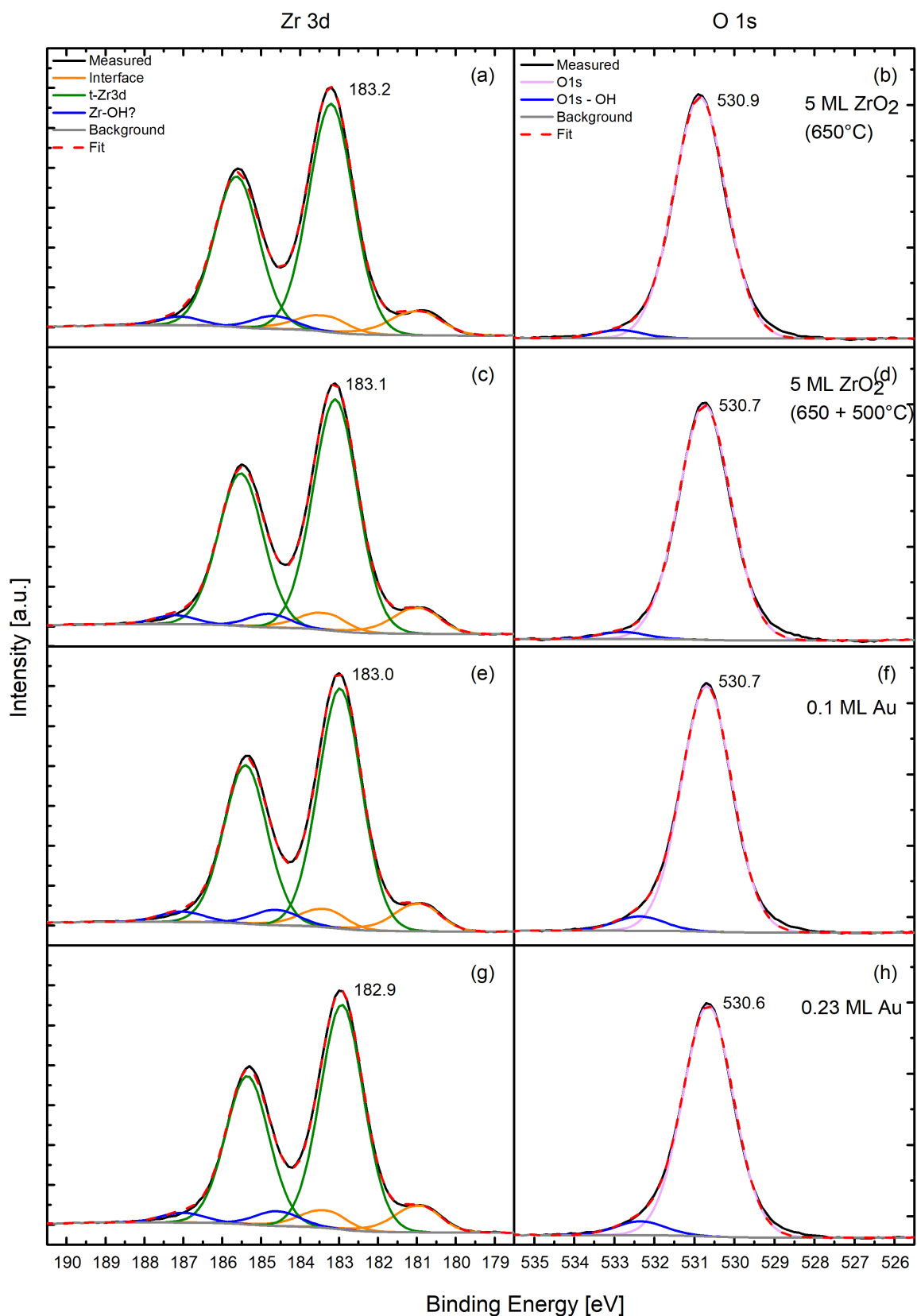
Figure 4.20: XPS fits of Zr 3d peaks (left column) and O 1s peaks (right column) after deposition of 5 ML ZrO_2 (annealed at 650 °C) (a),(b), additionally post-annealed the next day (500 °C) (c),(d), 0.1 ML Au (e),(f) and 0.2 ML Au (g),(h). The peak positions of tetragonal ZrO_2 Zr $3d_{5/2}$ and O 1s are shown next to the peaks.
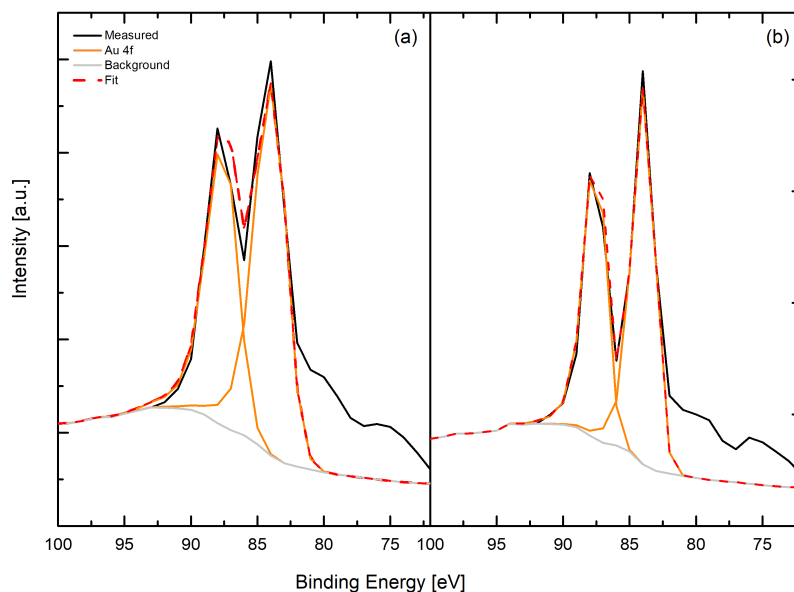
Figure 4.21: XPS spectra of 0.2 ML Au on tetragonal ZrO$_2$ (a) and on monoclinic ZrO$_2$ (b) ($E_{pass} = 50$ eV)

4.5.2 Au on Monoclinic ZrO$_2$

To study the growth of Au on monoclinic ZrO$_2$, 0.1 ML and 0.2 ML Au (at which 0.1 ML Au was added to the previous preparation) were deposited on the oxide, which correspond to 0.064 ML and 0.13 ML Au, respectively, with respect to Au(111).

After depositing 0.1 ML Au a cluster density of $1.28 \cdot 10^{16}$ m^{-2} is determined, which leads to 70 atoms per cluster on average. Two types of clusters can be observed (Fig. 4.22(a)). The cluster height of the smaller clusters is estimated to be below of 500 pm. The bigger clusters, however, are the predominant species and according to the height distribution, their cluster height lies in the range of 1000 pm, which indicates 3D growth (Fig. 4.22(c)). The clusters nucleate at step edges and terraces, but no preference can be determined. Moreover, the clusters interact easily with the tip and get strongly moved while scanning, which can be observed by comparing Fig. 4.22(a) with Fig. 4.22(b).

Scanning at very low sample bias (in the range of 1.5 V) enables the tip to move the clusters out of the scanning area. Fig. 4.23 shows a cluster-free area at the bottom, which was scanned at 1 V before, while the region above still shows Au clusters. Moreover, it can be observed that the cleaned area shows a monoclinic structure, which indicates that Au is not changing the surface structure permanently (Fig. 4.23 (inset)). Many bright features appear on the surface, however, which could not be assigned to a known species. Fig. 4.23 also shows fuzzy features, which were already observed on the clean

monoclinic ZrO_2 surface (see section 3.6 and Fig. 3.8).

Fig. 4.24 shows a hole in the oxide film down to the Rh(111) substrate and Au clusters growing on it. In contrast to the Au cluster growth on the oxide, Au is forming flat islands ($\approx 220\,\text{pm}$) and is wetting the metal surface. The islands have a triangular shape, which is indicative for Au(111) growth.

The XPS measurements after depositing Au show a peak shift of the monoclinic ZrO_2 Zr $3d_{5/2}$ peak by $+0.4\,\text{eV}$ to higher binding energies with respect to the clean monoclinic ZrO_2 peak. It is then positioned at $181.9\,\text{eV}$ (Fig. 4.25). The ratio between the three Zr 3d species stays constant. O 1s shifts in a similar way by $+0.4\,\text{eV}$ and the OH-O+O 1s peak is slightly increasing after depositing Au onto ZrO_2. The Au 4f peak, however, shifts by $-0.2\,\text{eV}$ with respect to pure Au (Fig. 4.21(b)).
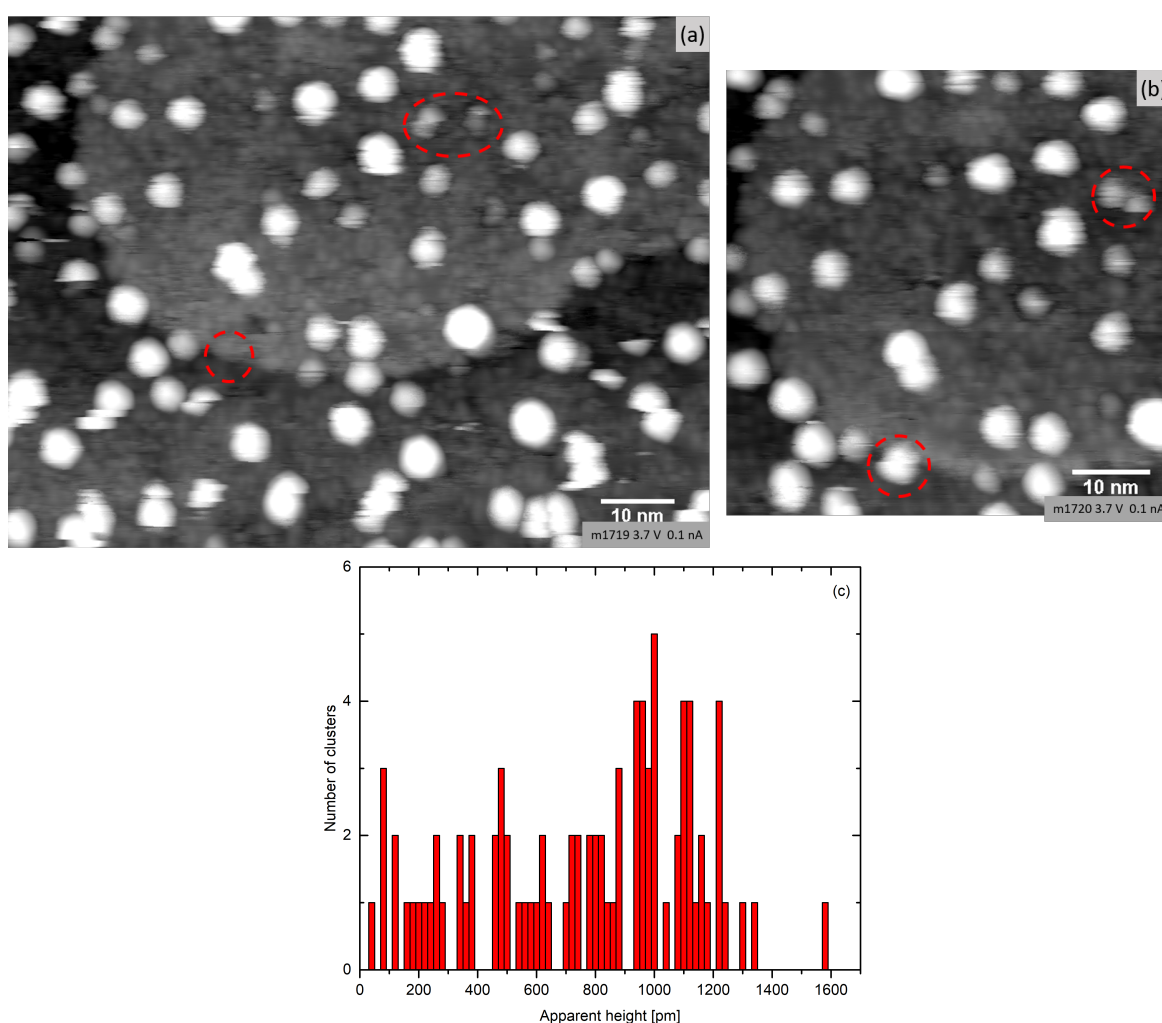
Figure 4.22: (a) STM image of 0.1 ML Au on monoclinic ZrO_2/Rh(111). The clusters are moving, which is visible by comparing (a) and (b) (red circles) (c) Cluster height distribution of (a).
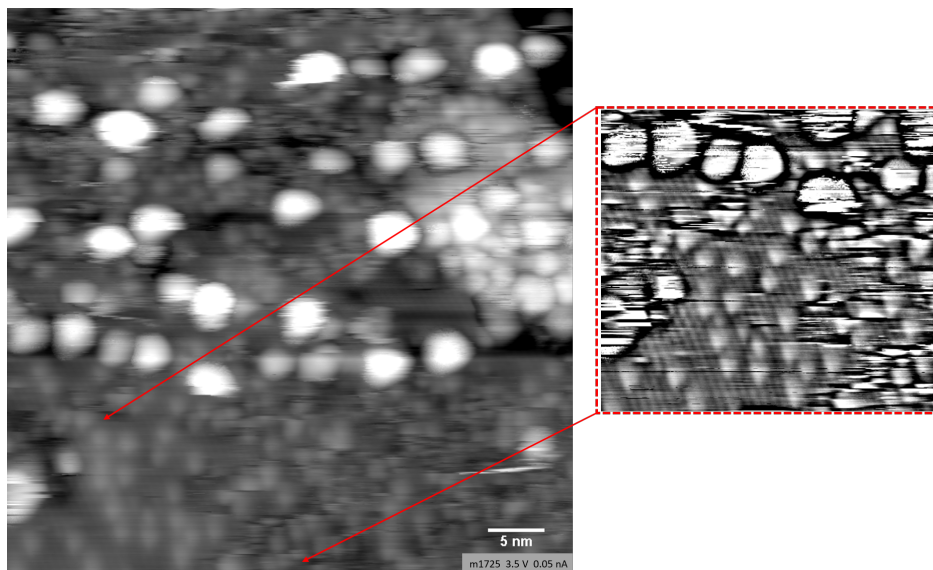
Figure 4.23: STM image of 0.1 ML Au on monoclinic ZrO$_2$/Rh(111): The bottom, which was scanned at 1 V before, is cluster-free. The inset shows a high-pass-filtered image of the cluster-free area and shows a monoclinic structure of the oxide.
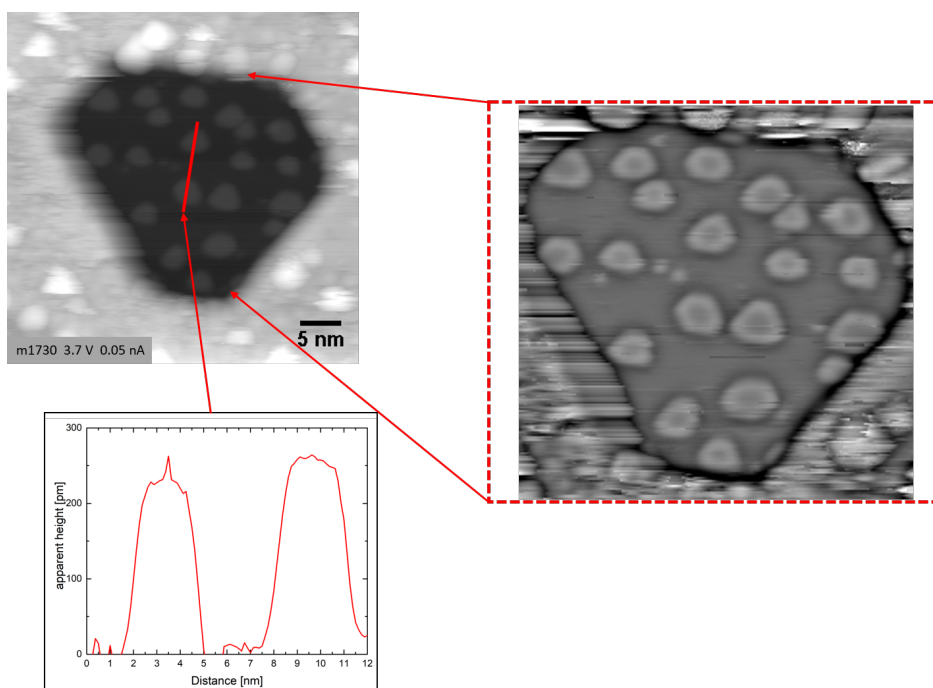
Figure 4.24: STM image of 0.1 ML Au on monoclinic ZrO$_2$/Rh(111) and a hole to the Rh(111) substrate. The image at the right is a high-pass-filtered image of the same region, which reveals the Au islands with a triangular shape. The line profile reveals a height of the Au islands of $\approx$220 pm.
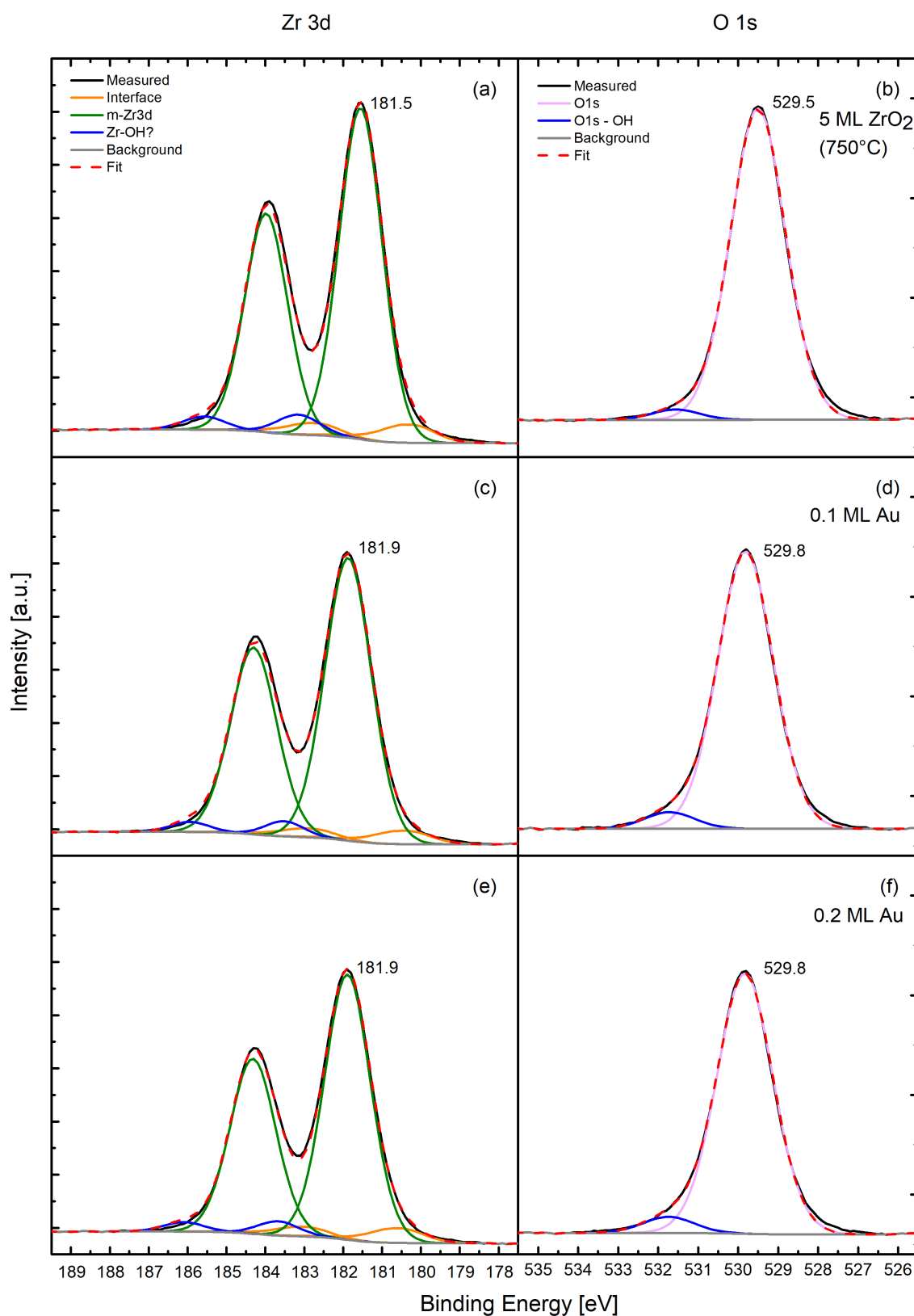
Figure 4.25: XPS fits of Zr 3d peaks (left column) and O 1s peaks (right column) after deposition of 5 ML ZrO_2 (post-annealed at 750 °C) (a),(b), 0.1 ML Au (c),(d) and 0.2 ML Au (e),(f). The peak positions of monoclinic ZrO_2 Zr $3d_{5/2}$ and O 1s are shown next to the peaks.

4.5.3 Discussion: Au growth on ZrO₂

The studies of Au nucleation on tetragonal and monoclinic ZrO_2 reveal a similar growth mode on both phases and the rounded clusters grow on terraces and at step edges, but no preference can be determined. Moreover, Au forms small and larger clusters, which reveals a 3D cluster growth on both phases. The smaller clusters reveal a predominant height of 340 pm on tetragonal ZrO_2, after deposition of 0.1 ML Au and the bigger clusters appear twice as high than the smaller clusters on both phases. The cluster density is higher on tetragonal ZrO_2 than on monoclinic ZrO_2 ($3.3 \cdot 10^{16}\,\mathrm{m}^{-2}$ vs. $1.3 \cdot 10^{16}\,\mathrm{m}^{-2}$ after deposition of 0.1 ML Au), which leads to different cluster sizes. The Au clusters interact with the tip on both phases and get moved, though the Au clusters on monoclinic ZrO_2 require a higher scanning voltage to not interact strongly with the tip. Scanning at low voltages (in the range of 1 V) enables the tip to move the clusters away on monoclinic ZrO_2. These observations indicate a weak bonding to the oxide on both phases but a weaker metal-oxide interaction on monoclinic ZrO_2 than on tetragonal ZrO_2.

XPS reveals a different behavior of tetragonal and monoclinic ZrO_2, after depositing Au. The Zr 3d and O 1s peaks shift by -0.3 eV to lower binding energies after depositing Au on tetragonal ZrO_2, whereas the peaks shift by +0.4 eV to higher binding energies on monoclinic ZrO_2. Au is hence influencing the electronic structure of ZrO_2 differently on both phases, which indicates that the bonding to the oxide varies. On the other hand the shifts could arise from a similar band alignment of the oxide in both phases induced by the metal clusters. Moreover, the OH peak in the O 1s region increases after deposition of Au, on both phases. The Au 4f peak shifts to lower binding energies by -0.2 ev, with respect to pure Au, on both phases (Fig. 4.21).

A comparison with Au cluster growth on ultra-thin ZrO_2 on Pt_3Zr, Pt_3Zr_{unrec} and Pd_3Zr presented in [6] shows many differences. Choi *et al.* showed that the growth mode strongly depends on the substrate and the cluster densities for the three substrates are $2.3 \cdot 10^{16}\,\mathrm{m}^{-2}$, $13 \cdot 10^{16}\,\mathrm{m}^{-2}$ and $21 \cdot 10^{16}\,\mathrm{m}^{-2}$, respectively. Therefore, according to the cluster densities, ZrO_2 on Pt_3Zr is most similar to the cluster growth on thicker ZrO_2 films. However, the Au clusters show preferential growth at domain boundaries and step edges on ZrO_2/Pt_3Zr, whereas Au shows no tendency towards growing at boundaries on thicker ZrO_2 films, neither on tetragonal nor on monoclinic ZrO_2. The clusters growing on terraces form flat, one monolayer thick, islands on ZrO_2/Pt_3Zr and the mean cluster height is smaller compared to the clusters at steps. The STM images of tetragonal and monoclinic ZrO_2 do not show such a different cluster growth at step edges.

4.6 Rh

Note: During deposition of 0.11 ML Rh on tetragonal ZrO_2 a repelling voltage of 1.2 kV was applied to prevent charged particles from hitting the sample, whereas no such voltage was applied when depositing 0.22 ML Rh. A repelling voltage was applied for all depositions of Rh on monoclinic ZrO_2.

Moreover, the position of the evaporator was not aligned well with the sample, which caused an inhomogenous Rh deposition of the sample.

4.6.1 Rh on Tetragonal ZrO_2

The tetragonal ZrO_2 surface used here showed few and small ZrO_2 islands. After depositing 0.11 ML and 0.22 ML Rh (0.08 ML and 0.16 ML, respectively, w.r.t. Rh(111)) it can be observed that the number of defects and holes increased (Fig. 4.26 and Fig. 4.27). Clusters do not grow preferentially at step edges or domain boundaries. The shape of the clusters appears round. Fig. 4.26 shows a cluster density of $3.1 \cdot 10^{16}\,m^{-2}$ after depositing 0.11 ML Rh which leads to an average number of atoms per clusters of 32. The cluster density increases after depositing 0.22 ML Rh (Fig. 4.27) to $4.3 \cdot 10^{16}\,m^{-2}$, whereas the cluster size does not change remarkably (average number of atoms: 45). It has to be noted that all the coverages and the resulting cluster densities are imprecise, due to inaccurate alignment of the evaporator. Considering the height distribution, it reveals that two types of clusters are growing: small clusters with the average height of 110 pm and bigger clusters with an average height of 320 pm (see line profiles in Fig. 4.26(a) and (b)). Moreover, the clusters do not move while scanning, but nevertheless interact with the tip, which can be identified by streaks.

Fig. 4.26(b) reveals the presence of fuzzy features (outside the red box), which were already observed on the clean monoclinic surface (see section 3.6 and Fig. 3.8). However, the fuzzy features are only observed at the edge of the image. The area containing no fuzzy features was already scanned at a sample bias of 5 V, which removed the fuzzy features (Fig. 4.26(a) and red box in Fig. 4.26(b)). Moreover, it can be observed that the Rh clusters in the fuzzy region appear smaller, whereas the Rh clusters in the middle appear higher and bigger, which is also exhibited by the height distributions on Fig. 4.26(c) and Fig. 4.26(d).

XPS reveals a peak shift of Zr 3d by -0.2 eV and the tetragonal Zr $3d_{5/2}$ peak is therefore located at 183.0 eV after a deposition of 0.11 ML Rh. The Zr-OH peak shifts accordingly, whereas the interface peak does not shift (Fig. 4.28). The ratio of the three peak doublets stays constant. Also the O 1s peak shifts to lower binding energies, to 530.7 eV (-0.2 eV w.r.t. clean tetragonal ZrO_2). The ratio between the O 1s and the

OH-peak is changing, with the OH signal increasing with increasing coverage of Rh.
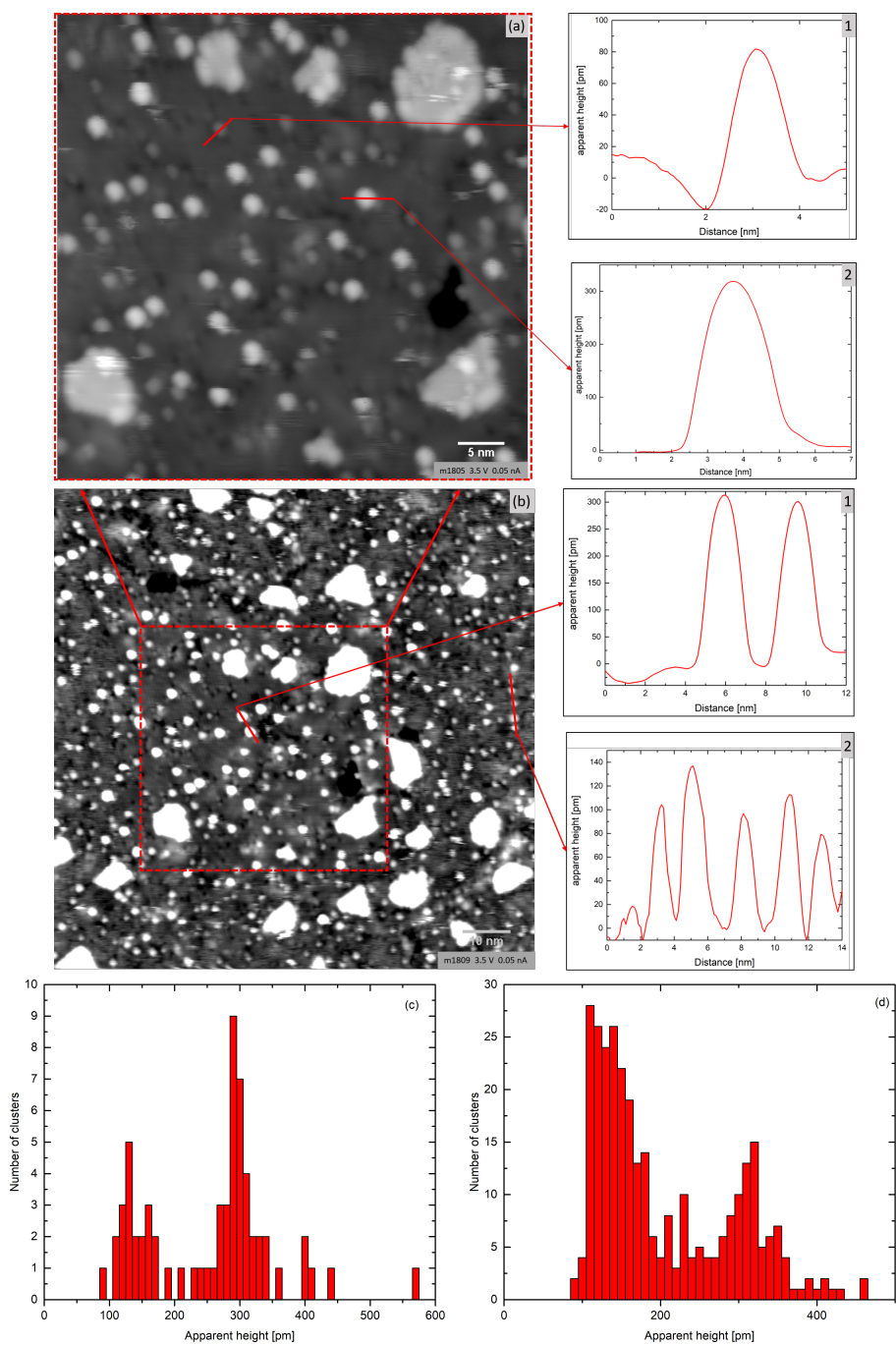
Figure 4.26: STM images of 0.11 ML Rh on tetragonal ZrO_2/Rh(111): (a) Small (Line profile 1) and bigger (Line profile 2) Rh clusters are visible, whose height distribution is shown in (c). (b) The same region is scanned in a larger scale: The area in the middle (red box) was scanned before at 5 V and the fuzzy features vanished. The area which was not scanned at higher voltages reveals fuzzy features, which let the Rh clusters appear lower (Line profile 2) in comparison to clusters of a fuzzy-free area (Line profile 1). (d) cluster height distribution of the whole area of (b).
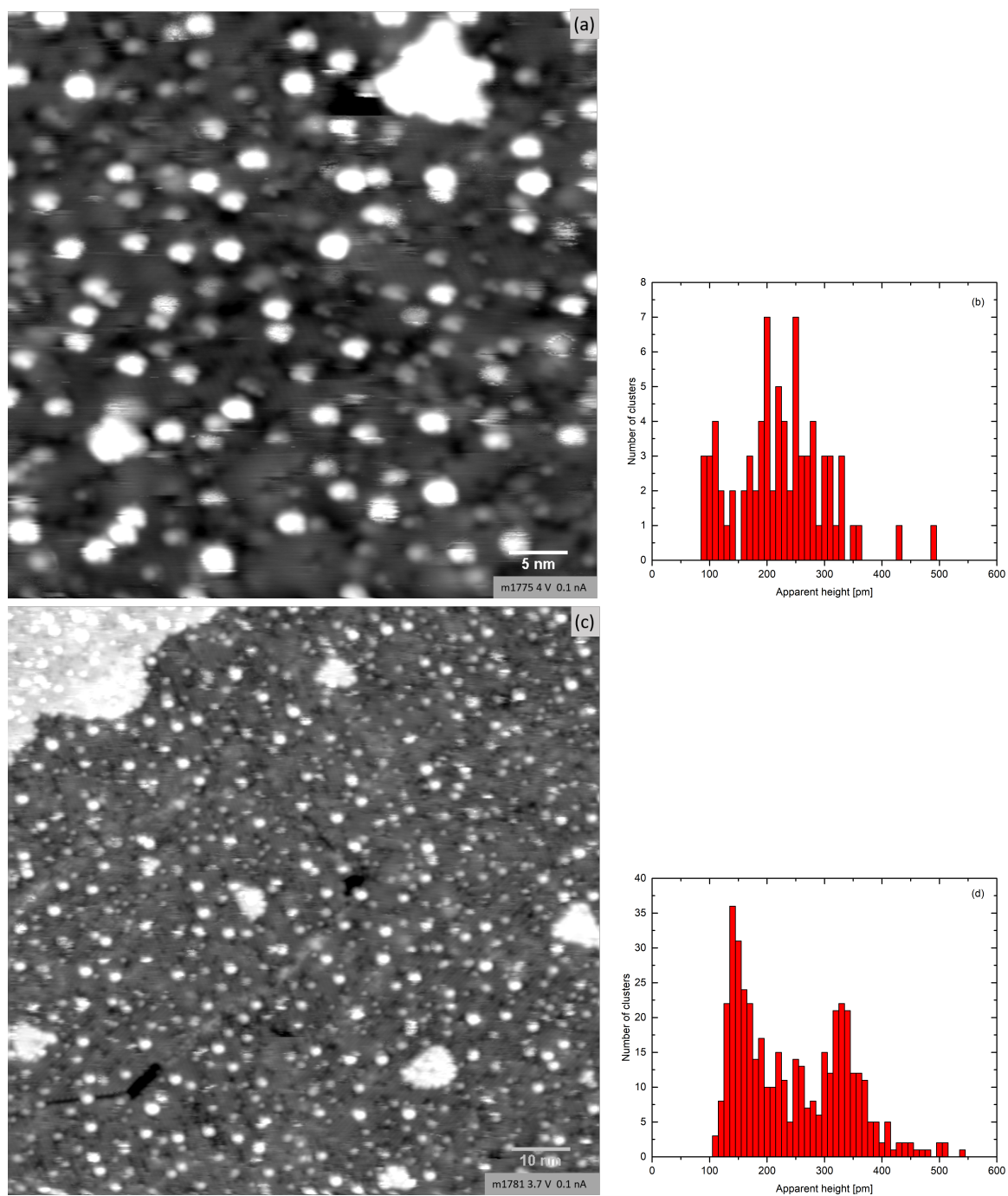
Figure 4.27: STM images of 0.22 ML Rh on tetragonal ZrO_2/Rh(111): (a) The Rh clusters appear as smaller and larger clusters after scanning at 6 V, which removes the fuzziness (b) Cluster height distribution of (a). (c) The cluster do not tend to grow on step edges (d) cluster height distribution (c).
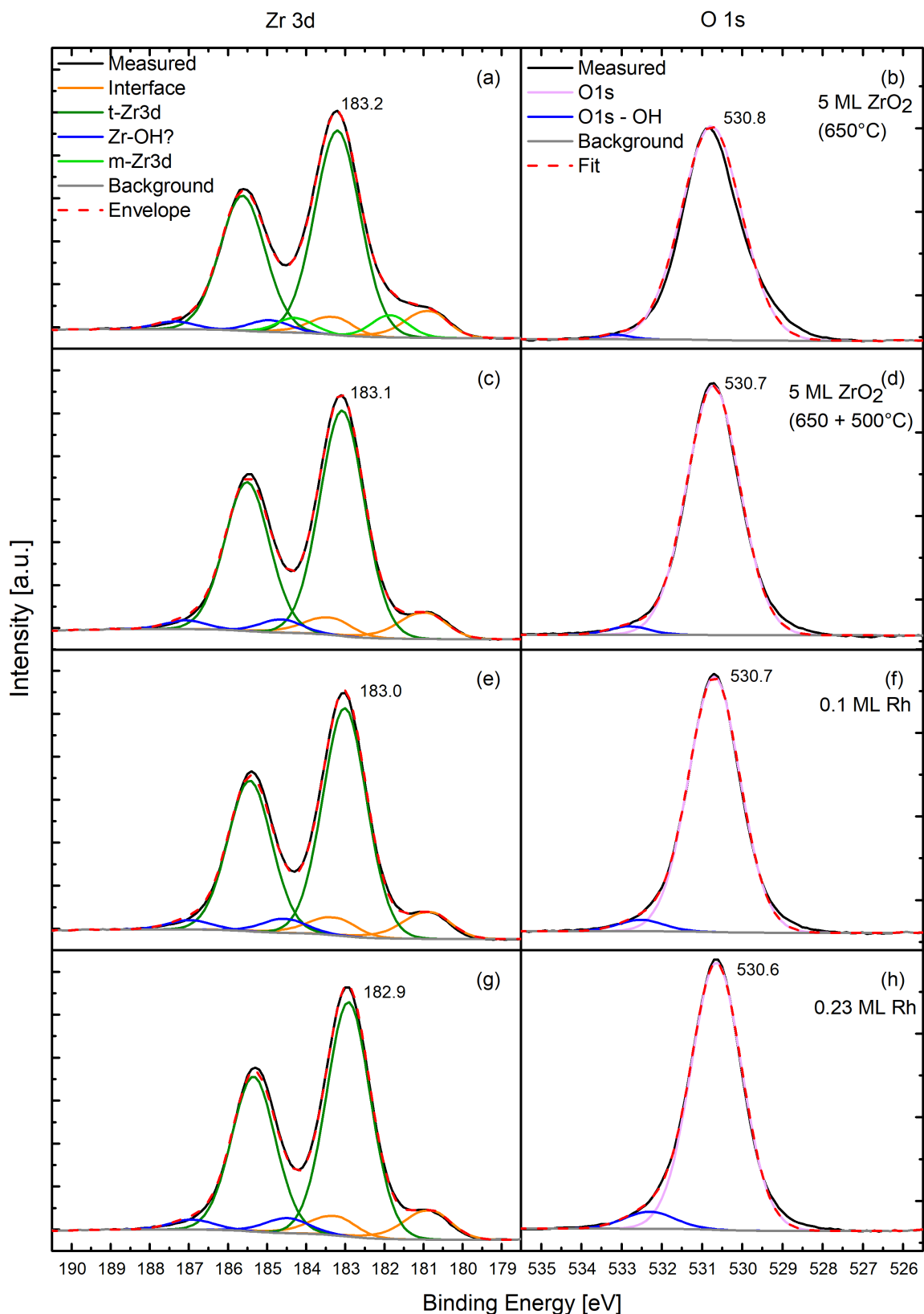
Figure 4.28: XPS fits of Zr 3d peaks (left column) and O 1s peaks (right column) after deposition of $5\,\mathrm{ML}$ ZrO_2 (post-annealed at $650\,°C$) (a),(b), additionally post-annealed the next day ($500\,°C$ (c),(d), 0.1 ML Rh (e),(f) and 0.2 ML Rh (g),(h). The peak positions of tetragonal ZrO_2 Zr $3d_{5/2}$ and O 1s are shown next to the peaks.

4.6.2 Rh on Monoclinic ZrO$_2$

To survey the growth of Rh on monoclinic ZrO$_2$, 0.16 ML and 0.32 ML Rh was deposited on the oxide (0.09 ML and 0.18 ML w.r.t. Rh(111)). Fig. 4.29(a) and (c) show the formation of rounded Rh clusters after depositing 0.16 ML Rh. It can be observed that the oxide surface appears smooth and not damaged so that the monoclinic ZrO$_2$ structure is well resolved. Moreover, it can be determined that the bright features, which form on the clean monoclinic ZrO$_2$ surface, are missing (see section 3.6). The clusters do not grow preferentially at step edges or on domain boundaries. An interaction with the STM tip can be observed, however at the streaky Rh clusters. Fig. 4.29(c) reveals a cluster density of $5.9 \cdot 10^{16} \, \mathrm{m}^{-2}$ and leads to 24 atoms per cluster on average. According to the height distribution in Fig. 4.29(d), the predominant Rh cluster height is 330 nm. By depositing 0.32 ML Rh the cluster density increases to $10.4 \cdot 10^{16} \, \mathrm{m}^{-2}$, whereas the cluster size does not change (Fig. 4.29(e)). Therefore, also the height distribution is not changing much (Fig. 4.29(d) and 4.29(f)).

The STM measurements reveal the presence of fuzzy features, which were already found on clean monoclinic ZrO$_2$ (see section 3.6 and Fig. 3.8). Similar to the clean monoclinic ZrO$_2$ surface, the fuzzy features can be removed by scanning at higher sample bias (above 6 V). Fig. 4.30(a) shows an image in which the fuzzy features had been already removed by scanning at 6 V in a 50×50 nm^2 area (red box), while fuzzy features are still present in the area around. The clusters in the area with the fuzzy features appear smaller and interact more with the tip than the clusters in the area without fuzzy features. While scanning at 6 V over the whole scanning area, the fuzzy features are removed everywhere (Fig. 4.30(c)). However, the clusters still appear differently. The 50×50 nm^2 region, which was free of fuzzy features already, still shows bigger clusters and is therefore still recognizable. In the following scan, however, (sample bias at 4.5 V) the clusters appear almost equal (Fig. 4.30(e)).

XPS reveals a peak shift of Zr 3d of the monoclinic and Zr-OH Zr 3d peaks to higher binding energies (+0.6 eV), which results in a peak position of the monoclinic Zr 3d$_{5/2}$ peak of 182.1 eV independent of the amount of deposited Rh (Fig. 4.31). Moreover, the FWHM increases after depositing Rh from 1.3 eV to 1.6 eV, which indicates a change in the electronic structure possibly caused by band bending. The O 1s peak shows a similar shift as Zr 3d of +0.6 eV to higher binding energies, with respect to clean monoclinic ZrO$_2$ and the O 1s OH peak area is slightly increasing after depositing Rh.
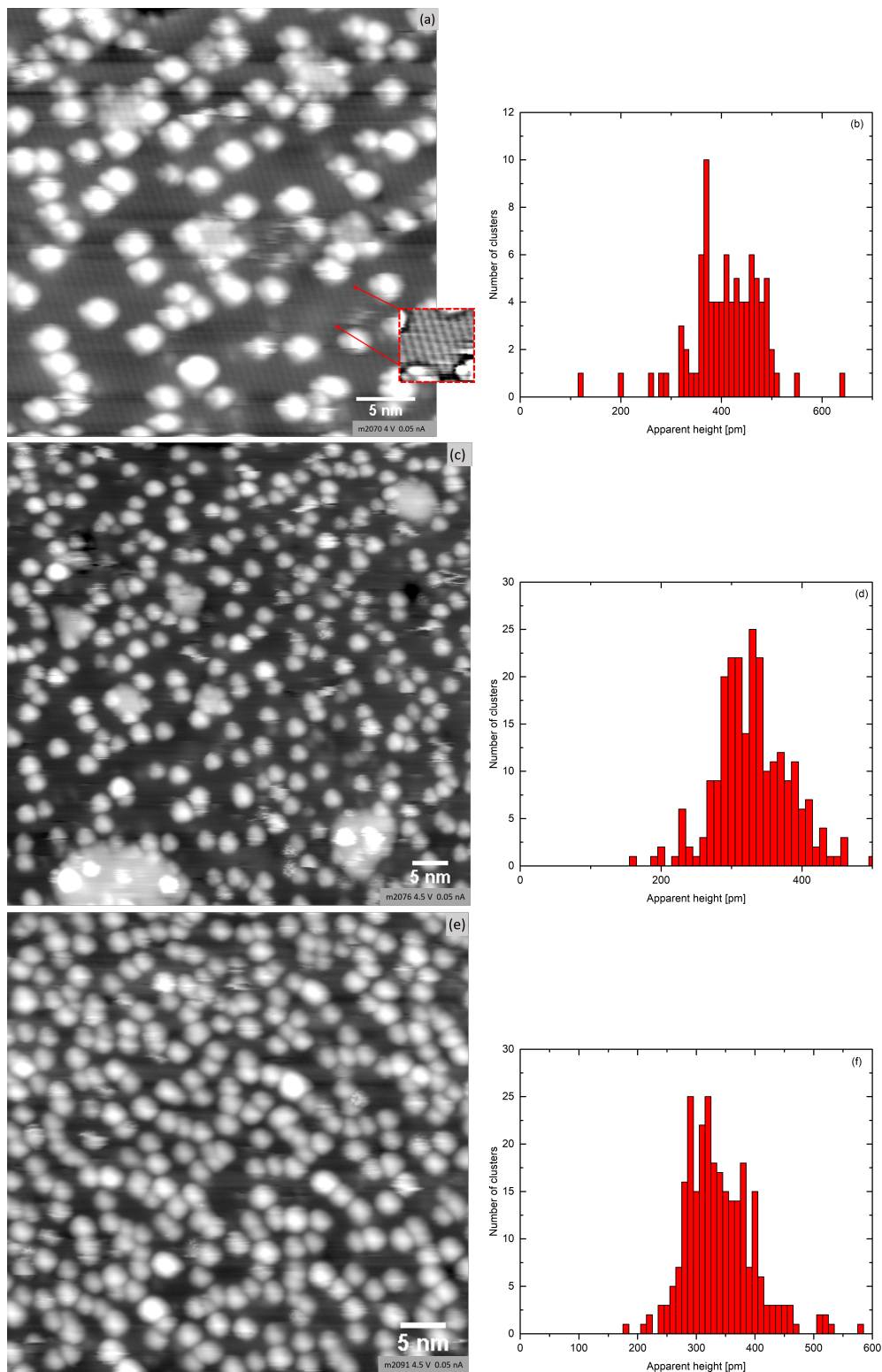
Figure 4.29: STM images of deposited Rh on monoclinic ZrO_2/Rh(111): (a) 0.16 ML Rh. The inset (high-pass-filtered) shows the monoclinic structure. (b) cluster height distribution of (a). (c) Larger-area image of 0.16 ML Rh: The clusters grow mainly on the terrace (d) cluster height distribution of (c). (e) 0.32 ML Rh: The cluster density does not change much compared to less Rh deposition and the cluster size increased. (f) cluster height distribution of (e)
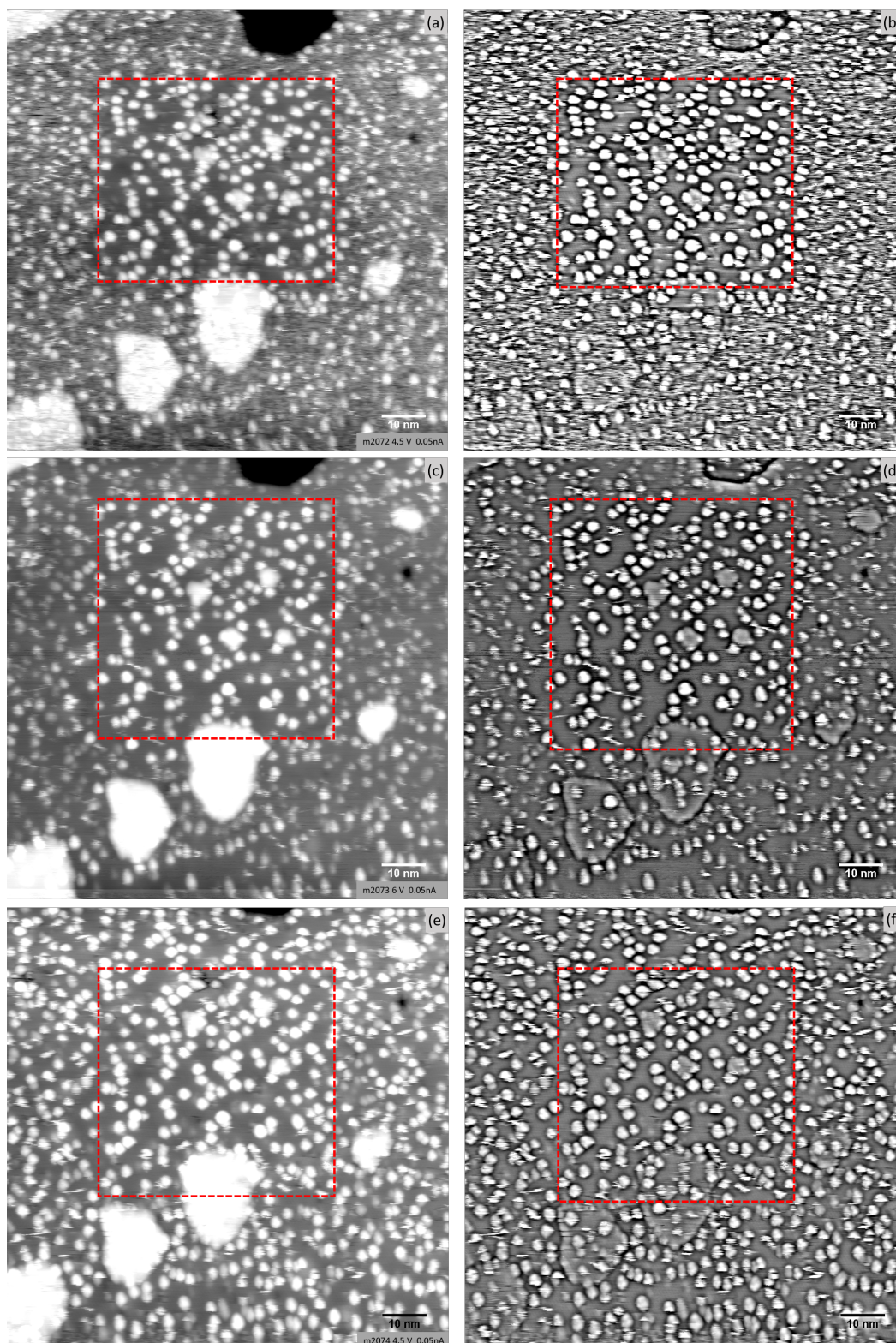
Figure 4.30: STM images of 0.16 ML Rh on monoclinic ZrO_2/Rh(111): By scanning at 6 V a 50×50 nm^2 area was cleaned from fuzzy features (box in (a)). By scanning at 4.5 V the fuzzy features do not vanish, as shown in (a) ((b): same image high pass filtered). Scanning at 6 V over the whole area moves all fuzzy features away (c), but the Rh clusters still appear different ((c): same image high pass filtered). After scanning at 4.5 V the clusters appear similar in the whole area (e) ((f): same image high pass filtered).
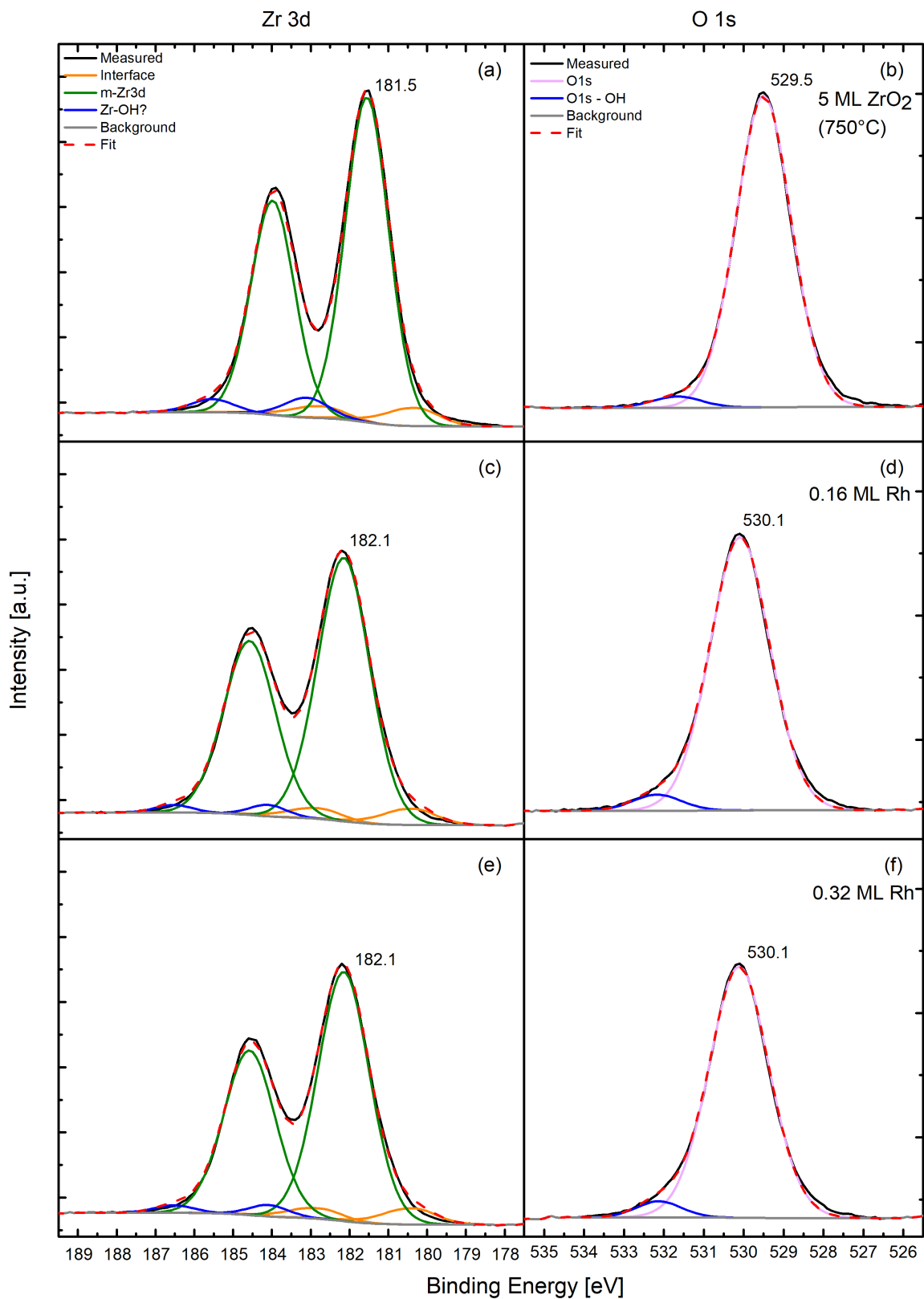
Figure 4.31: XPS fits of Zr 3d peaks (left column) and O 1s peaks (right column) after deposition of 5 ML ZrO_2 (post-annealed at 750 °C) (a),(b), 0.16 ML Rh (c),(d) and 0.32 ML Rh (e),(f). The peak positions of monoclinic ZrO_2 Zr $3d_{5/2}$ and O 1s are shown next to the peaks

4.6.3 Discussion: Rh growth on ZrO$_2$

The growth of Rh clusters on tetragonal and monoclinic ZrO$_2$ appears similar at first glance. The cluster densities are in the same range ($3.1 \cdot 10^{16}\,\mathrm{m^{-2}}$ vs. $5.9 \cdot 10^{16}\,\mathrm{m^{-2}}$ for deposition rates of 0.1 ML and 0.16 ML Rh, respectively) and also the cluster sizes appear similar, which show 32 and 24 atoms per cluster on average, respectively, and are within the error range. The cluster heights differ for the two phases, however. Although clusters with heights around 320–370 pm can be observed on both phases (after removing the fuzzy features by scanning at 6 V), the predominant cluster height on tetragonal ZrO$_2$ is 110 pm, whereas the predominant cluster height on monoclinic ZrO$_2$ is 330 pm. The different sample bias of 3.5 V and 4.5 V, respectively, must be considered, however. On both oxide phases the Rh clusters are bonding strongly to the oxide, since the clusters can hardly be moved by the tip and the clusters do not prefer to grow in height. With increasing coverage, we rather observe nucleation of new clusters. Moreover, the high cluster density indicates strong bonding of Rh to the oxide. Nevertheless, the Rh clusters interact with the tip on both oxide phases.

Both tetragonal and monoclinic ZrO$_2$, showed the fuzzy features, which could be removed by scanning at higher sample bias. After depositing Rh, the tetragonal ZrO$_2$ surface appeared defective, whereas the monoclinic ZrO$_2$ surface shows a smooth surface.

XPS, however, reveals a different behavior of the two oxide phases after depositing Rh. The Zr 3d$_{5/2}$ peak on tetragonal ZrO$_2$ shifts by -0.2 eV (w.r.t. clean tetragonal ZrO$_2$) to lower binding energies, whereas the Zr 3d$_{5/2}$ peak shifts by +0.6 eV to higher binding energies on monoclinic ZrO$_2$, which causes a peak position of Zr 3d$_{5/2}$ at 182.1 eV and its FWHM increases. The peak ratios of the three peak doublets of tetragonal ZrO$_2$, however, do not change much. The O 1s peak shifts on both phases as much as the to Zr 3d and the OH peak area increases on both phases after depositing Rh. Since the ZrO$_2$ films are prepared on Rh(111), a shift of Rh 3d caused by Rh nucleation on the oxide can not be determined and the experiment needs to be repeated on an different substrate to get clear results.

4.7 Summary of the Experimental Results

Table 4.2 summarizes the most important results of depositing metals on tetragonal and monoclinic ZrO$_2$. The cluster densities, the average number of atoms per cluster and the predominant cluster height of a given coverage is listed. The cluster heights are apparent cluster heights, since the apparent oxide thickness can not be calculated. An overview of all results and preparations can be found in appendix A. Moreover Table 4.3 lists the results of metal deposition on ultra-thin ZrO$_2$ [6].

Table 4.2: Properties of metal clusters grown on tetragonal (tet) and monoclinic (mon) ZrO$_2$/Rh(111) (*no repelling voltage applied to evaporator;°Data is inaccurate)

Metal	Fe*			Ag*		
Surface	tet	mon°	mon	tet	tet°	mon
Coverage [ML]	0.05	0.05	0.25	0.1	0.23	0.2
Cluster density [10^{16} m^{-2}]	6.4	5.3	6.4	2.7	3.2	0.49
Average atoms/cluster	7	8	35	34	64	364
Predom. cluster height [pm]	230	170	440	490	920	1440

Metal	Au			Rh	
Surface	tet°	tet	mon	tet	mon
Coverage [ML]	0.1	0.2	0.1	0.1	0.16
Cluster density [10^{16} m^{-2}]	3.3	4.3	1.3	3.1	5.9
Average atoms/cluster	27	39	70	32	24
Predom. cluster height [pm]	340	770	1000	110	330

Table 4.3: Properties of metal clusters grown on ultra-thin ZrO$_2$/Pt$_3$Zr,ZrO$_2$/Pt$_3$Zr$^{\text{unrec}}$ and ZrO$_2$/Pd$_3$Zr [6]

Surface	ZrO$_2$/Pt$_3$Zr			ZrO$_2$/Pt$_3$Zr$^{\text{unrec}}$	ZrO$_2$/Pd$_3$Zr	
Metal	Fe	Ag	Au	Au	Ag	Au
Cluster coverage [ML]	0.18	0.26	0.10	0.10	0.15	0.06
Cluster density [10^{16} m^{-2}]	24	0.53	2.3	13	5.3	21
Average atoms/cluster	7	464	41	7	26	3
predominant apparent height [pm]	220	1400	430	100	700	100

4.8 Discussion

Metal nucleation on tetragonal and monoclinic ZrO_2 reveals puzzling results for each surveyed metal. According to XPS, all metals induce a different behavior of ZrO_2. However, a trend can be determined by STM (see table 4.2 and appendix A). Fe and Rh form small clusters and show an uniformly distributed nucleation on both oxide phases, which leads to a high cluster density and indicates a strong metal-oxide bonding. Ag and Au, on the other hand, reveal heterogeneous nucleation and the formation of big 3D clusters, which can be easily moved or picked up by the STM tip at low voltages. Both is indicative for weak metal-oxide bonding. This fits to the results of Pan *et al.*, who examined the growth of Au on $ZrO_2(111)/Pt(111)$ by LEED, XPS and SRPES and found 3D cluster growth [30]. Moreover, they claimed a weak bonding of Au to the oxide. Han *et al.* studied the growth of Ag on $ZrO_2(111)/Pt(111)$ on the same system and found the growth of 3D particles which are weakly interacting with $ZrO_2(111)$ [31]. Both matches with the STM results presented in this work. A trend to higher metal-oxide bonding could be determined in the sequence: Ag≈Au<Fe≈Rh, which correlates with the results of metal nucleation on ultra-thin ZrO_2 films presented in [6]. Furthermore, the results of the STM measurements on monoclinic ZrO_2 films match with the DFT calculations for single adatoms on monoclinic ZrO_2 [6]. In contrast to the investigations on ultra-thin ZrO_2 films in [6], Au also follows the trend. Choi *et al.* claimed that Au binds not only to oxygen, but also to Zr by becoming a negative ion [6]. To diffuse from Zr to a neighboring O, Au has to transfer two electrons to the substrate to become positively charged. Since the electron transfer from the substrate to Au is hindered by the ultra-thin layer of insulating ZrO_2 in between, the diffusion of Au is reduced in comparison to Ag. This results in 2D islands at higher coverages and a lower cluster density than expected by DFT. Studies of Au deposition on supported MgO films revealed that Au has the ability to become negatively charged and to form 2D clusters on ≈3 ML thin oxide films. The clusters show enhanced bonding due to electrostatic interaction between the metallic substrate beneath the oxide and the metal clusters. On thicker oxide films (8 ML), however, Au tends to form 3D clusters and to bind to oxygen [32, 33]. Indeed, this fits our results on 5–6 ML ZrO_2 films, Au forms 3D clusters and due to the film thickness, a strong interaction between the Rh(111) substrate and Au clusters on top of the oxide film can be excluded. Thus, for the ZrO_2 films studied here, it can be followed that Au binds to oxygen and shows similar diffusion properties as Ag. It has to be noted, however, that during deposition of Fe and Ag on the ZrO_2 films, no repelling voltage was applied to the electrode of the evaporator, which may influenced the growth mode. Since Fe is forming small clusters and shows

a high cluster density, it is claimed that the oxide already offers enough nucleation sites, so that charged Fe atoms do not influence the results strongly by creating new nucleation sites through fast Fe ions. For Ag on the other hand, it is likely that fast Ag ions have created nucleation sites, which is distorting the cluster density and the cluster growth. Hence, the cluster density of Ag should decrease by applying a repelling voltage and would lead to larger clusters with weaker metal-oxide bonding.

All investigated metals reveal differences in their growth modes on tetragonal and monoclinic ZrO$_2$, respectively. Ag and Au form 3D clusters whose cluster density is higher on tetragonal ZrO$_2$. This is an astonishing result, since the studies on ultra-thin ZrO$_2$ revealed an increased cluster density for surfaces that were more strongly buckled [6]. Therefore, Choi *et al.* expected a higher cluster density for monoclinic ZrO$_2$ films due to the stronger distortion compared to tetragonal ZrO$_2$. Both Ag and Au nucleate on steps and terraces on both oxide phases. For Ag on tetragonal ZrO$_2$, a preferential nucleation at steps could be determined. For Ag on monoclinic ZrO$_2$ and Au on both oxide phases, more data is necessary to get a clear answer on preferential nucleation sites. Fe and Rh form similar clusters on tetragonal and monoclinic ZrO$_2$, although monoclinic ZrO$_2$ shows a slightly higher cluster density. The metals nucleate mainly on terraces and form both 2D and 3D clusters. Moreover, after depositing Fe and Rh on monoclinic ZrO$_2$, the oxide appears smooth and homogeneous. The bright features, which could be defects or adsorbates and are observed on the clean monoclinic ZrO$_2$ surface, vanished. Therefore, it is assumed that these bright features are good nucleation sites for Fe and Rh.

On tetragonal ZrO$_2$, fuzzy features were observed after depositing Fe and Rh. These are the same features that were observed on clean monoclinic ZrO$_2$, but not on clean tetragonal ZrO$_2$. It is suggested that the effect stems from mobile OH groups, which form through H$_2$ dissociating on metal but not on the bare oxide. The monoclinic ZrO$_2$ films have holes down to the Rh(111) substrate, which enables the dissociation, whereas dissociation on tetragonal ZrO$_2$ is only possible after the formation of metal clusters. Moreover, the apparent cluster heights of Fe and Rh may be influenced by the fuzzy features, due to induced band bending. This leads to a different apparent bias voltage and therefore to a lower apparent cluster height. Ag and Au nucleation on tetragonal ZrO$_2$ does not show such a formation of fuzzy features, though it requires further investigations to be able to exclude the formation of fuzzy features on this surfaces.

The XPS results reveal that the Zr 3d and O 1s peaks show similar shifts in the same direction after depositing metals on monoclinic and tetragonal ZrO$_2$ (Appendix A). Therefore, it can be claimed that the oxidation state is not changed by metal nucleation

and the oxide peak shifts are caused by shifted bands of the oxide. Though, XPS reveals a different behavior of tetragonal and monoclinic ZrO_2 films after depositing metals, which is not as easy to interpret. Monoclinic ZrO_2 shows a similar trend as the STM results. The Zr 3d and O 1s peaks are shifting to higher binding energies with respect to clean monoclinic ZrO_2 in the sequence Fe>Rh>Au≈Ag (see Appendix A). This shift and the increasing FWHM of Zr 3d and O 1s after depostion of Fe and Rh are indicating a changing electronic structure and correlate with the STM results: The stronger the metal-oxide interaction, the bigger the shift. A large shift is found for metals that form small clusters and show a high cluster density and therefore create a larger interface area. However, the results of metal nucleation on tetragonal ZrO_2 do not offer such a straight forward answer. The oxide peaks shift either slightly to higher binding energies (Fe), do not shift at all (Ag) or even shift to lower binding energies (Au and Rh) after depositing metals (w.r.t. clean tetragonal ZrO_2).

Several effects could be responsible for such a differing behavior of metal nucleation on tetragonal and monoclinic ZrO_2. It could be observed for all preparations that the difference of the binding energies between tetragonal and monoclinic ZrO_2 is reduced by depositing metals. It can be assumed that this is induced by band bending of the oxide due to metal clusters. The clusters bend the ZrO_2 bands, so that the binding energy changes for tetragonal ZrO_2, and monoclinic ZrO_2. Additionally, a catalytic spill-over reaction could be responsible for some effects. The metal clusters, especially Rh and Fe, would then act as catalysts for the splitting of adsorbed H_2 on the oxide. The higher the amount of OH on the oxide, the stronger the oxide peaks shift in XPS. XPS reveals a stronger peak shift on monoclinic ZrO_2, which would lead to the assumption that H or fuzzy features can diffuse more easily on monoclinic ZrO_2. STM showed a stronger coverage by the adsorbates for oxide surfaces with Fe and Rh clusters, compared to oxide surfaces with Ag and Au clusters. In fact, it is known that H_2 adsorbs less on Ag and Au. Moreover, Ag and Au show a lower cluster density than Fe and Rh, which leads to the assumption that the spill-over effect is stronger on Fe and Rh. Hence, that would explain the stronger shift of the oxide peaks on monoclinic ZrO_2 after depositing Fe and Rh in XPS.

The Zr 3d interface peak of tetragonal ZrO_2 does not behave like the main peak. It vares only by $\pm 0.1\,\text{eV}$ after metal nucleation (B.E. $180.9\,\text{eV}$), which lies within the fitting inaccuracy. Hence, the Rh(111) substrate stabilizes the electronic levels of tetragonal ZrO_2 at the interface. A similar behavior is expected from the Zr 3d interface peak on monoclinic ZrO_2. However, the monoclinic ZrO_2 peak overlaps with the interface peak and an accurate determination of the interface peak energy is therefore not possible.

An analysis of the O 1s peak area reveals one more trend for all preparations. The

OH-related peak area is increasing after the deposition of metals, which supports the suggestion of a spill-over reaction taking place. Especially on tetragonal ZrO_2, a clear increase from 3 % to 6 % is observable. However, since the Zr-OH peak is not increasing as much as the O 1s-OH peak, it is assumed that the Zr-OH peak is induced by an other effect than OH binding on Zr. It could also be that the main Zr 3d peak inhibits a slight asymmetry.

XPS reveals a strange behavior of the metal cluster peaks. On tetragonal ZrO_2, compared with the pure metals, Fe 2p and Ag 3d show a peak shift of 0.6 eV and 0.3 eV to higher binding energies, respectively, whereas Au 4f shifts to lower binding energies -0.2 eV (see Appendix A). Rh 3d could not be investigated, since Rh(111) was used as a substrate. On monoclinic ZrO_2, only Fe 2p shows a clear peak shift to higher binding energies with respect to pure Fe. Au 4f shifts slightly to lower binding energies, whereas Ag 3d does not shift on monoclinic ZrO_2, which is surprising. A peak shift of Au 4f depending on the particle size was presented in [30]. The authors found a peak shift by +0.4 eV with respect to pure Au for small deposited amounts (in the range of 0.05 ML Au w.r.t. Au(111)), which decreases with increasing amount of deposited Au. According to [31], Ag behaves similarly: Ag 3d shifts by +0.5 eV with respect to pure Ag after depositing 0.05 ML Ag (w.r.t. Ag(111)) on ZrO_2(111)/Pt(111) and the shift decreases with an increasing Ag deposition. Such a shift could only be observed on tetragonal ZrO_2 in this work, but not on monoclinic ZrO_2. It has to be considered, however, that no repelling voltage was applied when depositing Ag, which may have influenced the results. The cluster density could decrease by depositing Ag with a repelling voltage, since fewer ions reach the sample surface and create nucleation sites.

5 Conclusion

The examination of the growth of 5–6 ML thick ZrO_2 films by STM, LEED and XPS revealed the formation of a (2×1) row structure (w.r.t. cubic ZrO_2) and that the Zr $3d_{5/2}$ is located at a binding energy of 183.2 eV (after post-annealing in O_2 atmosphere at 650 °C). Both is confirming tetragonal ZrO_2. At annealing temperatures of 750 °C ZrO_2 transforms into monoclinic phase. This can be seen in STM and LEED by the formation of a (2×2) structure (w.r.t. cubic ZrO_2) and in XPS due to a shift of the oxide peaks to lower binding energies. For this structure, the Zr $3d_{5/2}$ peak is located to 181.5 eV.

Nucleation of metals on 5–6 ML thick ZrO_2 films in both phases was studied. The examination of the growth mode, cluster density, and cluster sizes by STM lead to following trend: The metals show different strengths of metal-oxide bonding: Ag≈Au<Fe≈Rh. The XPS measurements revealed that the oxide peaks shift to higher binding energies according to the strength of metal-oxide bonding on monoclinic ZrO_2. On tetragonal ZrO_2, however, the oxide peaks either do not shift at all or are slightly shifting to lower or higher binding energies. As a general trend, it was found, that the XPS peaks of tetragonal and monoclinic ZrO_2 are closer after depositing metals on the oxide. The OH-related O 1s peak is increasing after depositing metal on both phases, which is likely to be caused by a spill-over reaction.

The oxide peak shifts may be partly explained by band bending of the oxide induced by metal nucleation. A spill-over reaction of, e.g. H^+ from the metal clusters to the oxide may also play a role, although it does not fully explain all peak shifts. It is very likely that a combination of the already presented effects and at minimum one other effect explains the presented system. Therefore, further investigations of these systems are required to unravel the exact mechanism of band bending induced by metal nucleation on ZrO_2.

Bibliography

[1] S.-J. Hao, C. Wang, T.-L. Liu, Z.-M. Mao, Z.-Q. Mao, and J.-L. Wang, "Fabrication of nanoscale yttria stabilized zirconia for solid oxide fuel cell", *International Journal of Hydrogen Energy*, 2017.

[2] E Ivers-Tiffée, K. Härdtl, W Menesklou, and J Riegel, "Principles of solid state oxygen sensors for lean combustion gas control", *Electrochimica Acta*, vol. 47, no. 5, pp. 807–814, 2001.

[3] R. H. French, S. Glass, F. Ohuchi, Y.-N. Xu, and W. Ching, "Experimental and theoretical determination of the electronic structure and optical properties of three phases of ZrO_2", *Physical Review B*, vol. 49, no. 8, p. 5133, 1994.

[4] M. Antlanger, W. Mayr-Schmölzer, J. Pavelec, F. Mittendorfer, J. Redinger, P. Varga, U. Diebold, and M. Schmid, "Pt_3Zr(0001): A substrate for growing well-ordered ultrathin zirconia films by oxidation", *Physical Review*, vol. B 86, p. 035 451, 2012.

[5] J. Choi, W Mayr-Schmölzer, F Mittendorfer, J Redinger, U Diebold, and M Schmid, "The growth of ultra-thin zirconia films on Pd_3Zr(0001)", *Journal of Physics: Condensed Matter*, vol. 26, no. 22, p. 225 003, 2014.

[6] J. I. J. Choi, W. Mayr-Schmölzer, I. Valenti, P. Luches, F. Mittendorfer, J. Redinger, U. Diebold, and M. Schmid, "Metal Adatoms and Clusters on Ultrathin Zirconia Films", *The Journal of Physical Chemistry*, vol. 120, pp. 9920–9932, 2016.

[7] P. Lackner, J.-I. J. Choi, U. Diebold, and M. Schmid, "Construction and evaluation of an ultrahigh-vacuum-compatible sputter deposition source", *Review of Scientific Instruments*, vol. in press, 2017.

[8] K. Oura, V. Lifshits, A. Saranin, A. Zotov, and M. Katayama, *Surface Science; An Introduction*. 2003, Springer.

[9] H.-J. Güntherodt and R. W. (Eds.), *Scanning Tunneling Microscopy I*. 1992, Springer.

[10] M. Schmid, *Experimentelle Methoden der Oberflächenphysik*, Skriptum, 2016.

[11] S. Hüfner, *Photoelectron Spectroscopy.* 1995, Springer.

[12] E. H. Kisi and C. Howard, "Crystal structures of zirconia phases and their inter-relation", in *Key Engineering Materials*, Trans Tech Publications, vol. 153, 1998, pp. 1–36.

[13] R. C. Garvie, "The Occurrence of Metastable Tetragonal Zirconia as a Crystallite Size Effect", *Journal of Physical Chemistry*, vol. 64, no. 4, pp. 1238–1243, 1964.

[14] P. Kountouros and G. Petzow, "Defect Chemistry, Phase Stability and Properties of Zirconia Polycrystals", in *Science and Technology of Zirconia V*, S. Badwal, M. Bannister, and R. Hannink, Eds. Technomic Poblishing, USA, 1993, p. 30.

[15] N. Igawa, Y. Ishii, T. Nagasaki, Y. Morii, S. Funahashi, and H. Ohno, "Crystal structure of metastable tetragonal zirconia by neutron powder diffraction study", *Journal of the American Ceramic Society*, vol. 76, no. 10, pp. 2673–2676, 1993.

[16] S. Badwal, "Zirconia-based solid electrolytes: microstructure, stability and ionic conductivity", *Solid State Ionics*, vol. 52, no. 1–3, pp. 23–32, 1992.

[17] M. Bocanegra-Bernal and S. D. De La Torre, "Phase transitions in zirconium dioxide and related materials for high performance engineering ceramics", *Journal of Materials Science*, vol. 37, no. 23, pp. 4947–4971, 2002.

[18] P Platt, P Frankel, M Gass, R Howells, and M Preuss, "Finite element analysis of the tetragonal to monoclinic phase transformation during oxidation of zirconium alloys", *Journal of Nuclear Materials*, vol. 454, no. 1, pp. 290–297, 2014.

[19] K. Meinel, K.-M. Schindler, and H. Neddermeyer, "Growth, structure and annealing behaviour of epitaxial ZrO_2 films on Pt(111)", *Surface Science*, vol. 532-535, pp. 420–424, 2003.

[20] K. Meinel, A. Eichler, K.-M. Schindler, and H. Neddermeyer, "STM, LEED, and DFT characterization of epitaxial ZrO_2 films on pt(111)", *Surface Science*, vol. 562, pp. 204–218, 2004.

[21] K. Meinel, A. Eichler, K.-M. Schindler, H. Neddermeyer, and W. Widdra, "Surface and interface structures of epitaxial ZrO_2 films on Pt(111): Experiment and density-functional theory calculations", *Physical Review B*, vol. 74, p. 235 444, 2006.

[22] H. Li, J.-I. J. Choi, W. Mayr-Schmölzer, C. Weilach, C. Rameshan, F. Mittendorfer, J. Redinger, M. Schmid, and G. Rupprechter, "Growth of an Ultrathin Zirconia Film on Pt$_3$Zr Examined by High-Resolution X-ray Photoelectron Spectroscopy, Temperature-Programmed Desorption, Scanning Tunneling Microscopy, and Density Functional Theory", *Journal of Physical Chemistry*, vol. 119, pp. 2462–2470, 2015.

[23] J. I. J. Choi, *Studies of Zirconia Surfaces on the Atomic Scale*, PhD thesis at Vienna University of Technology, 2016.

[24] P. E. S. John F. Moulder William F. Stickle and K. D. Bomben, *Handbook of X-ray Photoelectron Spectroscopy*. 1992, Perkin-Elmer Corporation.

[25] W. Smekal, W. S. Werner, and C. J. Powell, "Simulation of electron spectra for surface analysis (SESSA): a novel software tool for quantitative Auger-electron spectroscopy and X-ray photoelectron spectroscopy", *Surface and Interface Analysis*, vol. 37, no. 11, pp. 1059–1067, 2005.

[26] C. Huang, Z. Tang, and Z. Zhang, "Differences between Zirconium Hydroxide (Zr(OH)$_4$·nH$_2$O) and Hydrous Zirconia (ZrO$_2$·nH$_2$O)", *Journal of the American Ceramic Society*, vol. 84, pp. 1637–1638, 2001.

[27] T. Chraska, A. H. King, and C. C. Berndt, "On the size-dependent phase transformation in nanoparticulate zirconia", *Materials Science and Engineering*, vol. A286, pp. 169–178, 2000.

[28] D. Majumdar and D. Chatterjee, "X-ray photoelectron spectroscopic studies on yttria, zirconia, and yttria-stabilized zirconia", *Journal of Applied Physics*, vol. 70, 1991.

[29] E. Napetschnig, M. Schmid, and P. Varga, "Pd, Co and Co–Pd clusters on the ordered alumina film on NiAl(110): Contact angle, surface structure and composition", *Surface Science*, vol. 601, no. 15, pp. 3233–3245, 2007.

[30] Y. Pan, Y. Gao, G. Wang, D. Kong, L. Zhang, J. Hou, S. Hu, H. Pan, and J. Zhu, "Growth, Structure, and Stability of Au on Ordered ZrO$_2$(111) Thin Films", *The Journal of Physical Chemistry C*, vol. 115, no. 21, pp. 10 744–10 751, 2011.

[31] Y. Han, Q. Xu, W. Wang, and J. Zhu, "Atomic-Scale Insight into the Metal–Support Interaction: A Case for Ag Nanoparticles on Ordered ZrO$_2$(111) Thin Films", *The Journal of Physical Chemistry C*, vol. 119, no. 8, pp. 4235–4241, 2015.

[32] D. Ricci, A. Bongiorno, G. Pacchioni, and U. Landman, "Bonding Trends and Dimensionality Crossover of Gold Nanoclusters on Metal-Supported MgO Thin Films", *Physical Review Letters*, vol. 97, p. 036 106, 3 2006.

[33] M. Sterrer, T. Risse, M. Heyde, H.-P. Rust, and H.-J. Freund, "Crossover from three-dimensional to two-dimensional geometries of Au nanostructures on thin MgO(001) films: A confirmation of theoretical predictions", *Physical Review Letters*, vol. 98, no. 20, p. 206 103, 2007.

A STM and XPS results

Table A.1: STM analysis of metal nucleation on tetragonal and monoclinic ZrO_2

Fe

		Tetragonal ZrO_2		Monoclinic ZrO_2			
Image n		1238	1240	1285	1330	1453	1448
Image size	m^2	8.63E-15	8.07E-15	9.28E-15	9.00E-16	1.00E-14	2.20E-15
scan voltage	V	3.5	3	3	3.5	4	3.5
scan current	nA	0.1	0.1	0.1	0.05	0.1	0.1
Coverage	ML	0.05	0.05	1.25	0.05	0.25	0.25
atoms per area m2 (ZrO2)	m^-2	8.91E+18	8.91E+18	8.91E+18	8.91E+18	8.91E+18	8.91E+18
ML Fe with respect to Fe(110)	ML	0.026	0.026	0.647	0.026	0.129	0.129
Cluster density	m^-2	6.26E+16	6.42E+16	1.49E+17	5.33E+16	6.78E+16	6.45E+16
average atoms per cluster		7	7	75	8	33	35
Predominant cluster height	pm	150	230	400 (310, 590)	170, (240)	430 (310)	440

Ag

		Tetragonal ZrO_2			Monoclinic ZrO_2
Image n		1497	1518	1577	1644
Image size	m^2	9.49E-15	3.45E-14	8.88E-15	1.00E-14
scan voltage	V	3	3.5	3	4
scan current	nA	0.1	0.05	0.05	0.1
Coverage	ML	0.05	0.1	0.23	0.2
atoms per area m2 (ZrO2)	m^-2	8.91E+18	8.91E+18	8.91E+18	8.91E+18
ML Fe with respect to Fe(110)	ML	0.023	0.046	0.105	0.092
Cluster density	m^-2	1.21E+16	2.66E+16	3.19E+16	4.90E+16
average atoms per cluster		37	34	64	364
Predominant cluster height	pm	640 (380)	490 (720)	1180 (240, 720)	1440 (1040)

Au

		Tetragonal ZrO_2				Monoclinic ZrO_2
Image n		1682	1684	1697	1700	1719
Image size	m^2	2.28E-15	2.50E-15	1.95E-15	1.00E-14	6.87E-15
scan voltage	V	3.5	3	2.9	2.9	3.7
scan current	nA	0.05	0.05	0.1	0.05	0.1
Coverage	ML	0.1	0.1	0.2	0.2	0.1
atoms per area m2 (ZrO2)	m^-2	8.91E+18	8.91E+18	8.91E+18	8.91E+18	8.91E+18
ML Fe with respect to Fe(110)	ML	0.064	0.064	0.128	0.128	0.064
Cluster density	m^-2	2.81E+16	3.28E+16	4.27E+16	4.60E+16	1.28E+16
average atoms per cluster		32	27	42	39	70
Predominant cluster height	pm	300, 600, 760	340	470 (850)	770 (430, 940)	1000

Rh

		Tetragonal ZrO_2		Monoclinic ZrO_2		Monoclinic ZrO_2			
Image n		1805	1809	1775	1781	2070	2076	2086	2091
Image size	m^2	2.50E-15	1.00E-14	2.50E-15	1.00E-14	1.33E-15	4.19E-15	2.50E-15	2.59E-15
scan voltage	V	3.5	3.5	4	3.7	4	4.5	4.5	4.5
scan current	nA	0.05	0.05	0.05	0.1	0.05	0.05	0.05	0.05
Coverage	ML	0.11	0.11	0.22	0.22	0.16	0.16	0.32	0.32
atoms per area m2 (ZrO2)	m^-2	8.91E+18	8.91E+18	8.91E+18	8.91E+18	8.91E+18	8.91E+18	8.91E+18	8.91E+18
ML Fe with respect to Fe(110)	ML	0.082	0.082	0.163	0.163	0.089	0.089	0.178	0.178
Cluster density	m^-2	2.56E+16	3.11E+16	3.12E+16	4.35E+16	6.63E+16	5.87E+16	1.04E+17	1.05E+17
average atoms per cluster		38	32	63	45	22	24	27	27
Predominant cluster height	pm	290	110, (320)	200-250	140, (330)	370	330	370	320

Table A.2: XPS analysis of metal nucleation on tetragonal and monoclinic ZrO$_2$

	5ML ZrO2					Fe on Tet ZrO2		Fe on Mon ZrO2		Ag on Tet ZrO2			
Preparation	RT	500°C	550°C	650°C	750°C	0.05ML Fe	1.25ML Fe	0.05ML Fe	0.25ML Fe	clean (500°C)	0.05ML Ag	0.1ML Ag	0.23ML Ag
B.E.	[eV]	[eV]	[eV]	[eV]	[eV]	[eV]	[eV]	[eV]	[eV]	[eV]	[eV]	[eV]	[eV]
Tetragonal	183.38	182.78	182.83	183.2		183.45	183.17			183.16	183.28	183.26	183.14
Monoclinic	181.87				181.55			182.61	182.56				
Interface	180.54	181.28	181.21	180.92	180.25	180.92	180.96	181.34	181.19	180.98	180.98	180.97	180.96
OH	185.21	184.46	184.39	184.85	183.15	185.02	184.84	184.39	184.53	184.68	184.97	184.96	184.67
Metal Zr	179.45										178.78		
Area	[%]	[%]	[%]	[%]	[%]	[%]	[%]	[%]	[%]	[%]	[%]	[%]	[%]
Tetragonal	79	84	85	84	0	86	81	0	0	83	83	85	85
Monoclinic	4			0	88	0	0	88	89	0	0	0	0
Interface	10	11	10	11	6	10	12	10	9	11	11	11	10
OH	5	5	5	6	5	4	6	2	2	6	5	5	5
Metal Zr	3										1		
FWHM	[eV]	[eV]	[eV]	[eV]	[eV]	[eV]	[eV]	[eV]	[eV]	[eV]	[eV]	[eV]	[eV]
Tetragonal	1.52	1.35	1.34	1.35		1.42	1.39			1.32	1.36	1.37	1.34
Monoclinic	1.24				1.30			1.65	1.73				
Interface	1.56	1.33	1.23	1.34	1.40	1.39	1.39	1.58	1.41	1.31	1.49	1.40	1.24
OH	1.39	1.33	1.36	1.44	1.28	1.30	1.50	1.05	1.03	1.43	1.35	1.36	1.33
Metal Zr	1.21										0.93		
BE	[eV]	[eV]	[eV]	[eV]	[eV]	[eV]	[eV]	[eV]	[eV]	[eV]	[eV]	[eV]	[eV]
O1s	531.23	530.48	530.56	530.86	529.50	531.13	530.90	530.39	530.48	530.82	530.98	530.95	530.85
OH	533.07	532.39	532.14	532.87	531.56	533.06	532.68	532.46	532.73	532.80	532.80	532.80	532.59
Area	[%]	[%]	[%]	[%]	[%]	[%]	[%]	[%]	[%]	[%]	[%]	[%]	[%]
O1s	95	97	95	97	97	96	94	95	95	97	95	95	94
OH	5	3	5	3	3	4	6	5	5	3	5	5	6
Ratio O/Zr	1.31	1.42	1.48	1.45	1.42	1.46	1.47	1.58	1.55	1.43	1.47	1.45	1.47

Table A.3: XPS analysis of metal nucleation on tetragonal and monoclinic ZrO_2

Preparation	Ag on Mon ZrO2		Au on Tet ZrO2			Au on Mon ZrO2		Rh on Tet ZrO2			Rh on Mon ZrO2	
	0.1ML Ag	0.2ML Ag	Clean (+500°C)	0.1 ML Au	0.2 ML Au	0.1 ML Au	0.2 ML Au	clean (+500°C)	0.1ML	0.2ML	0.16ML	0.32ML
B.E.	[eV]	[eV]	[eV]	[eV]	[eV]	[eV]	[eV]	[eV]	[eV]	[eV]	[eV]	[eV]
Tetragonal			183.09	182.97	182.92			183.08	183.01	182.92		
Monclinic	181.92	181.98				181.87	181.89				182.15	182.15
Interface	180.40	180.61	180.92	180.90	180.89	180.37	180.53	180.93	180.82	180.81	180.35	180.35
OH	183.55	183.60	184.80	184.62	184.59	183.51	183.68	184.65	184.56	184.49	184.07	184.09
Metal Zr												
Area	[%]	[%]	[%]	[%]	[%]	[%]	[%]	[%]	[%]	[%]	[%]	[%]
Tetragonal	0	0	85	84	83	0	0	84	84	83	0	0
Monoclinic	92	90	0	0	0	91	90	0	0	0	91	90
Interface	5	6	10	11	11	5	6	11	11	12	6	6
OH	4	4	5	6	6	4	4	5	5	5	3	3
Metal Zr												
FWHM	[eV]	[eV]	[eV]	[eV]	[eV]	[eV]	[eV]	[eV]	[eV]	[eV]	[eV]	[eV]
Tetragonal			1.36	1.31	1.31			1.35	1.32	1.32		
Monclinic	1.43	1.43				1.41	1.39				1.58	1.56
Interface	1.34	1.44	1.25	1.20	1.20	1.47	1.41	1.24	1.25	1.22	1.40	1.40
OH	1.15	1.15	1.25	1.38	1.34	1.17	1.23	1.24	1.33	1.33	1.12	1.21
Metal Zr												
BE	[eV]	[eV]	[eV]	[eV]	[eV]	[eV]	[eV]	[eV]	[eV]	[eV]	[eV]	[eV]
O1s	529.86	529.90	530.74	530.69	530.65	529.81	529.83	530.72	530.69	530.64	530.09	530.12
OH	531.71	531.81	532.80	532.37	532.34	531.72	531.74	532.81	532.52	532.30	532.17	532.12
Area	[%]	[%]	[%]	[%]	[%]	[%]	[%]	[%]	[%]	[%]	[%]	[%]
O1s	95	94	97	95	94	95	95	98	96	94	95	95
OH	5	6	3	5	6	5	5	2	4	6	5	5
Ratio O/Zr	1.44	1.46	1.41	1.44	1.44	1.45	1.47	1.42	1.43	1.46	1.47	1.42